NANYANG TECHNOLOGICAL UNIVERSITY

EFFICIENT AND ACCURATE MODELING OF FINITE-SIZE PRINTED CIRCUIT STRUCTURE

LIU ZHIHONG

SCHOOL OF ELECTRICAL AND ELECTRONIC ENGINEERING

2010

Efficient and Accurate Modeling of Finite-Size Printed Circuit Structure

LIU ZHIHONG

School of Electrical and Electronic Engineering

A thesis submitted to the Nanyang Technological University
in fulfillment of the requirement for the degree of
Doctor of Philosophy

2010

ABSTRACT

Printed circuit board (PCB) is one of the crucial parts of electronic packaging. It is mounted with a large number of high-speed electronic devices and serves as a platform for numerous interconnections amongst these devices. With the trend of increasing operating frequency, PCB layouts of high-speed digital circuits become important for the circuit designers. Without proper PCB layout consideration at the design stage, electromagnetic interference (EMI) and signal integrity (SI) issues will surface and affect the functionality of the digital circuit.

To allow an evaluation of PCB layout to meet EMI and SI requirements at the design stage, accurate and efficient simulating tool for printed circuit interconnects is necessary. For high-speed operating environment in the GHz range, lumped circuit modeling of the interconnecting traces on PCB is no longer accurate. Full-wave electromagnetic modeling of PCB provides excellent simulation results accurately. Nearly all full-wave electromagnetic simulation tools rely on solving Maxwell's equations using numerical method. It is also well known that modeling large printed circuit structure based on numerical method can be computational prohibitive due to the long computation time to construct the large matrix resulting from numerical method.

One of the popular numerical methods for electromagnetic modeling of PCB is the Method of Moments (MoM), which provides the numerical solution of the Maxwell's equations using the integral formulation. To improve the computational efficiency of

MoM based numerical method, efficient and accurate integration of the Green's function is essential.

In this thesis, an in-depth study and analysis on the accurate and efficient integration of Greens function is carried out. By expanding the Green's function into the Taylor's series, closed form expression of the integration of the Taylor's series is developed, which reduces the solution time of MoM method significantly. The analytical expression for the integration of the Green's function also makes the solution highly accurate.

ACKNOWLEDGMENTS

I wish to express my sincere gratitude and appreciation to my supervisor, Dr. See Kye Yak, Associate Professor of Circuits and Systems Division, Director of Electromagnetic Effects Research Laboratory (EMERL), School of Electrical and Electronic Engineering, Nanyang Technological University (NTU), for his guidance and encouragement throughout the course of my research work. I like to thank my co-supervisor, Dr. Li Er Ping, Senior Manager of Electronics and Software Applications, Institute of High Performance Computing, Agency for Science, Technology and Research (A*STAR), for his generosity to facilitate the necessary computational resources.

I must thank Dr. Chua Eng Kee, former research student of Dr. See, for his valuable inputs and comments related to my research work. I also like to thank Mr. Hu Bo, Mr. Manish Oswal and other research staff for their technical support and assistance during my study in NTU.

Thanks also go to my family for their understanding, unfailing love and patience. Without them, completion of this thesis would not have been possible. Finally, financial support from NTU is gratefully acknowledged.

Table of Contents

List of Figures

List of Tables

CHAPTER ONE

1 INTRODUCTION

1.1 Importance of EMI and SI Analysis

With the widespread use of electronic circuits in almost every aspect in life, such as entertainment, computation and wireless telecommunication, electromagnetic interference (EMI) has become a problem that cannot be ignored. EMI refers to a phenomenon where an electrical or electronic device/system generates electromagnetic field in the radio frequency (RF) spectrum that degrades the satisfactory operation of another electronic device/system in its vicinity [1]–[4]. As today's clock speeds of integrated circuits approach the GHz range and edge rates reduce to the picoseconds range, the radiated emission from the a digital board can be significant, if no proper consideration is paid on the board layout. High emission from portable digital devices can cause EMI to useful communication systems. For example, a notebook computer can interfere with the navigation system in an airplane, which can endanger passenger safety. Therefore, attention on PCB design must be paid in order to reduce the emission from these digital devices. Internationally, many countries have imposed stringent EMI regulations on imported electronics products to reduce the EMI risk to other electronics systems as well as to protect the communications spectrum [5]–[7]. For example, the Federal Communications Commission (FCC) of USA has imposed EMI regulation as early as 1979 and the European Community has enforced the electromagnetic compatibility (EMC) directive in 1997.

Besides radiated emission issue, high-speed digital design to ensure signal integrity (SI) is another major design issue for circuit designers [8]. Conventionally, PCB interconnects have little influence on the high-speed digital design. However, with ever-increasing clock speed, transmission line effects of interconnects begin to have a significant impact on high-speed digital design [9]. Without good impedance matching design, signal reflections at the receiving gates occur and cause signal ringing, which could lead to false triggering of logic state. The fast edge rates of digital signals also result in inter-trace crosstalk, which is usually caused by undesired capacitive, inductive, or conductive coupling from one circuit or channel to another. In addition, grounding design consideration is a must in high-speed system design to minimize the ground bounce. All these problems seriously affect signal propagation and hamper the quality of the digital signal. Due to the physical size constraint of the PCB, crosstalk is a common phenomenon which occurs in PCB design and the techniques to simulate and to mitigate it have been well studied [10]–[13]. Transmission line effects refer to the reflections arising due to impedance mismatch of a between the gate and the PCB trace [14]. Ground bounce means ground voltage fluctuation during logic gate switching [15]–[17]. Resolving SI problems on high-speed board can be of great assistance in achieving a quiet board to meet EMI requirement. Most SI problems can be avoided through suitable layout and termination techniques [18]–[21].

To control radiated emission from a high-speed board, it is essential to understand the mechanism of the digital circuit radiation. The radiation mechanism composes of two modes, the differential-mode (DM) [22]–[23] and the common-mode (CM) [24]–[30]. DM radiation can be effectively controlled by proper PCB layout, which includes circuit loop area control and good power supply decoupling. The main causes of

radiation in most systems are PCBs with the interconnecting cables, as these cables are the primary contributors of unintentional CM emissions. In most cases, CM radiation causes a product to fail the final EMI, as smaller CM current of a cable can produce higher emission than a circuit loop with larger DM current [24]. The causes of these CM currents are usually due to the poorly designed signal current return current paths on the PCB [20]. When clock speeds are less than 10MHz or so, the return current path of the digital circuit is not particularly important. However, with on-board data bus speed in the several hundred MHz range, the return path of high-speed signal must be properly considered in the design stage. Imperfect return paths result in high ground bounce, which will convert into significant CM current in the cable.

Although there are many modern high-speed PCB analysis tools available for SI analysis, EMI effect remains one that is nearly impossible to be simulated in a complete and accurate way. In order to model the radiation mechanism properly, DM and CM emissions have to be computed for every net on board and the resulting electromagnetic fields in all directions need to be combined to get the resultant radiated electromagnetic field. Considering the large amount of nets, it will be very time consuming and require many tradeoffs to reach a solution, and such tradeoffs then sacrifice accuracy of results. Therefore, developing an electromagnetic solver with both accuracy and efficiency will make great advancement in the modeling and simulation of PCB to predict its characteristics, power distribution behaviours and EMI radiation.

1.2 Motivation

Since radiated emissions at the PCB level are usually dominated by radiated fields from interfacing cables and printed circuit interconnects, a suitable electromagnetic modeling and simulation method that is capable of analyzing the characteristics of radiation becomes useful so that effective EMI corrective measures could be implemented during the design stage.

Conventionally, most commercial EM simulation tools are targeted at the microwave and RF design communities. These tools usually extract the scattering characteristics of interconnects but detailed information for the printed circuit structures for power bus or ground bounce analysis is usually not readily available. Hence, from the EMI perspective, these tools provide little information for the physical insight required for EMI analysis.

Practically, all full-wave electromagnetic field solvers use either finite element method (FEM) [31]–[33], finite-difference time-domain (FDTD) method [34]–[36], transmission line matrix (TLM) method [37]–[38], finite-volume time-domain (FVTD) method [39]–[40], or method of moments (MoM) [41]–[42], in order to solve the Maxwell's equations in time or frequency domain. For problems with bounded and sufficiently small volume, differential methods such as FEM, FDTD and TLM are usually adopted. These differential methods are suitable in modeling bounded problems such as shielded enclosures or waveguides as the boundary can be assigned on the physically finite region. For open boundary problems, integral method, such as MoM is preferred, as the radiation condition is implicit within the integral equation formulation.

In reality, all PCBs are finite-size with non-ideal power and ground planes. Unfortunately, most moment method based simulation tools employ infinite stratified media approach and assume infinite PCB ground/power planes for ease of numerical modeling. Hence, the motivation here is to develop a full-wave modeling method that is suitable for more in-depth analysis of EMI problems at the PCB level.

In this thesis, the author employs the full-wave MOM technique that allows modelling of realistic finite-size PCBs based on an exact volume/surface integral equation formulation approach. By enforcing the boundary conditions for the Maxwell's equations on the conductor and substrate of a PCB, a set of electric field integral equations (EFIEs) is formulated. As the formulation allow true finite-size PCB to be modeled, EMI problems associated with non-ideal ground plane and traces near the PCB edges can be modeled with ease. Hence, CM current in an attached cable and ground bounce phenomena of a PCB can be predicted numerically using the proposed approach.

In any MoM formulation, depending on the selection of the basis functions and the test functions, the impedance matrix can be ill-conditioned [42]–[48]. As such, the overall accuracy depends very much on the accurate evaluation of the integrals, especially diagonal elements of the matrix. Besides accuracy, computational efficiency is a major concern. The solution time for MoM consists of the matrix-fill time and the matrix-solve time. The matrix-fill time is the time taken to calculate all the elements of the impedance matrix whereas, the matrix-solve time is the time taken to solve the matrix. Depending on the matrix size, the matrix-fill time can contribute a significant portion of the total solution time. Many approaches have been reported to reduce the matrix-fill

time. One common approach is to employ interpolation method [49]–[52]. It evaluates impedance matrices at a few selected frequencies and interpolates impedance matrices for the rest of frequencies. The improvement on the overall matrix-fill time depends on the number of simulation frequencies, which can be several decades. However, the matrix-fill time for a single frequency still takes up substantial amount of time. Another approach is the application of the artificial neural networks (ANN) based model [53], [54]. Its computational efficiency is superior but suffers in solution's accuracy. Subsequently, a hybrid approach that combines neural networks and method of moments (NN-MoM) [55] is proposed to optimize both matrix-fill time and solution accuracy. It employs two trained radial basis function-neural networks (RBF-NN) to calculate majority of elements in the coupling matrix, the rest of elements are calculated using the conventional method. This approach provides better accuracy but does not reduce matrix-fill time significantly. Some researchers use analytical simplification method [56]–[58] to reduce the impedance equation format from double integral to single integral. This approach effectively reduces the matrix-fill time but it is still not as efficient as the analytical approach for the evaluation of the impedance matrix elements [59]–[61]. Some other fast algorithms are also reported in [62]–[65]. Since the analytical approach eliminates the need of numerical integration and reduces the matrix-fill time significantly, it will be the main focus of this thesis.

1.3 Objective and Contributions of the Thesis

The objective of this thesis is to investigate and develop an efficient and accurate MoM algorithm that is suitable for modeling of finite-size PCB for EMI and SI analyses. The thesis has derived an accurate analytical formulation to solve the integrals involving

free-space Green's function for any combination of basis and test functions. During the matrix filling procedure, the closed form integral formulation derived in the thesis reduces the simulation time significantly without the trade-off in accuracy. Without prohibitive computational effort, relatively complex and large-scale structures can be simulated with good solution accuracy.

The major contributions of this thesis are thought to be:

- Based on the distance between the source and observation points, a criterion is established to reduce the full integral equation in MoM to a much-simplified expression, which speeds up the computational efficiency to fill up the MoM matrix.

- Derivation of the analytical expression for the integration of the free-space Green's function. It allows highly efficient and accurate evaluation of the integrals involved in MoM matrix. Accuracy and efficiency has been demonstrated in comparison with numerical integration approach.

1.4 Organization of the Thesis

The thesis is organised into the following chapters. In the first chapter, the importance of EMI/SI considerations for high-speed PCB design is addressed. The motivation, objective and contributions of the thesis have also been discussed.

Chapter 2 is dedicated to the integral formulation of a printed circuit structure using the field equivalence theorem. By enforcing the necessary boundary conditions, a set of

electric field integral equations are established. Based on the MoM technique, an impedance matrix is formed and the unknown current distributions of the printed circuit structure can be obtained.

Chapter 3 introduces a highly efficient and accurate approach to calculating the elements in the MoM matrix. The approach is based on an analytical expression for the integration of the free-space Green's function involving any combination of basis and test functions. Full analytical formulations are derived by direct integration of Taylor's series expansion of the free-space Green's function. A criterion is established to reduce the full expression to a simplified expression further. This method speeds up the computation efficiency to fill up the MoM matrix without loss of solution accuracy.

Chapter 4 validates the accuracy and efficiency of the developed MoM code and demonstrates its ability for SI and EMI analyses.

Chapter 5 concludes the thesis and recommends possible future work.

CHAPTER TWO

2 MODELING OF FINITE-SIZE PCB STRUCTURE

Numerical modeling techniques such as FDTD, FEM, PEEC (Partial Element Equivalent Circuit) and MoM have been used widely as supporting tools to assist engineers to model and analyze EMI/EMC design problems. Each of these modeling techniques has its own strengths in solving specific types of problems. Differential methods such as FDTD and FEM are popular for electromagnetic field problems with well-defined enclosed boundaries. However, they require additional field extension procedure for modeling open boundary problems, such as radiated fields from high-speed PCBs [66]–[68]. Integral methods such as MoM and PEEC are ideal for open boundary problems as their formulations require no further treatment for radiation problems [69]–[71].

Traditionally, the MoM formulations are based on the Green's functions that involve infinite stratified media. With these formulations, only the conductor surface currents are the unknown variables to be determined using the exact version of Green's function for an infinite layered media [72]–[76]. Although such formulations reduce the number of unknowns to be solved for, it has the inherent limitation to deal with realistic 3D finite-size printed circuit structures, where the pertinent common-mode phenomenon due to asymmetry of printed circuit structure cannot be predicted. The proposed MoM formulation to be described in this chapter has the flexibility to model true 3D finite-

size substrate without simplifying assumptions so that the common-mode radiation behaviours of a 3D printed circuit can be predicted [65][77][78]. The following sections in this chapter explain the derivation of the numerical formulation of the Maxwell's equations that is capable of modeling any arbitrary 3D printed circuit structure with defined geometry and dimension.

The volume equivalence theorem will be first discussed as it forms the basis in forming the electric field integral equations (EFIEs). With the enforcement of the conductor/dielectric boundary conditions, a set of EFIEs that is suitable for the radiation and scattering analysis of finite-size printed circuit structure will be formulated. The handling of surface charge density in the EFIEs at the conductor/dielectric boundary due to the polarisation effect of the dielectric substrate will be described in details. Then, the unknown magnetic vector potential **A** and electric scalar potential ϕ are deduced using d'Alembert formula. Through the use of MoM, the EFIEs are converted into a discrete system of equations and the MoM impedance matrix is established. Finally, the unknown complex current coefficients in the equation will be determined.

2.1 Formulation of the Electric Field Integral Equations

Based on the field equivalence theorem [79], one of the fundamental concepts in electromagnetics, any objects subjected to an excitation field can be replaced by their electric and magnetic equivalent currents situated in the regions occupied by the objects.

These equivalent current sources produce the scattered fields. The resultant Maxwell's equations can be expressed in equations (2.1) and (2.2) .

$$\nabla \times \mathbf{E} = -\mathbf{K}_{eq} - j\omega\mu_o \mathbf{H} \tag{2.1}$$

$$\nabla \times \mathbf{H} = \mathbf{J}_{eq} + \mathbf{J} + j\omega\varepsilon_o \mathbf{E} \tag{2.2}$$

where **J** is the time harmonic electric source current density. The equivalent magnetic and electric current densities $\mathbf{K}_{eq}$ and $\mathbf{J}_{eq}$ can be obtained as follows.

$$\mathbf{K}_{eq} = j\omega\mu_o(\mu_r - 1)\mathbf{H} \tag{2.3}$$

$$\mathbf{J}_{eq} = j\omega\varepsilon_o(\varepsilon_r - 1)\mathbf{E} \tag{2.4}$$

By superposition in a linear medium, the resultant field in the entire space **E** is the vector sum of the excitation field $\mathbf{E}^i$ and the scattered fields $\mathbf{E}^s$ as given in equation (2.5).

$$\mathbf{E} = \mathbf{E}^i + \mathbf{E}^s \tag{2.5}$$

This theorem allows the EFIEs to be formulated in only a single medium, usually free space. Considering a finite-size PCB structure situated in a homogeneous infinite free space as shown in Fig. 2.1, it is composed of a perfect conductor surface occupying S_c and a homogeneous, lossless dielectric volume occupying V_d. The PCB is excited by an incident time harmonic electric field $\mathbf{E}^i$ with angular frequency ω . In the presence of the PCB, scattered electric field $\mathbf{E}^s$ is produced. The resultant electric field **E** is the vector sum of $\mathbf{E}^i$ and $\mathbf{E}^s$.

Applying the field equivalence theorem, the field scattered by the PCB can be determined by replacing the PCB with its equivalent current densities radiating in free space. The conductor surface S_c and the dielectric substrate V_d can be replaced by

equivalent surface current density $\mathbf{J}_c$, and equivalent volume polarisation current density $\mathbf{J}_d$, respectively, both radiating in free space, as shown in Fig. 2.2.

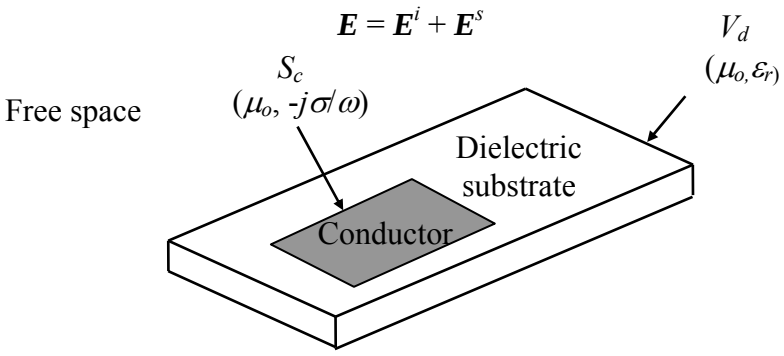

Fig. 2.1 Electric filed in the presence of finite-size printed circuit structure

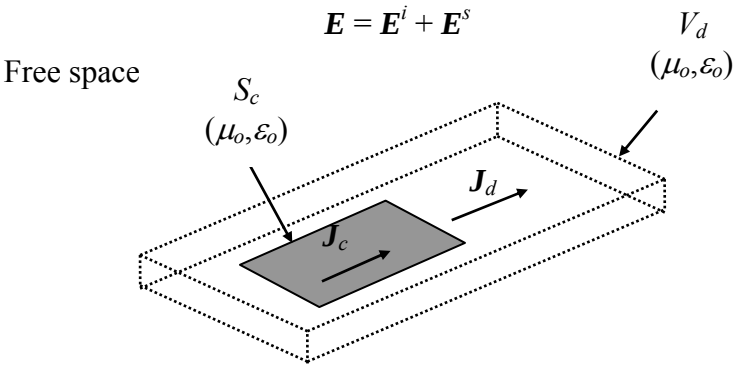

Fig. 2.2 Equivalence problem of Fig.2.1

Typical PCB substrate has the thickness of 1.6 mm (or 60 mil) or so and the conductor thickness is in the range of 0.025 ~0.05 mm (or 1~2 mil). Hence, the conductor is considered to be very much thinner than the substrate. To reduce the computational effort, it is convenient to assume that the conductors are of zero thickness.

The necessary conductor/substrate boundary conditions can be imposed to solve the unknown electric field $\mathbf{E}^s$. Fig. 2.3 illustrates the boundary between a perfect conductor and a dielectric body [79]–[80].

On the conductor surface, tangential electric field is equal to zero.

$$[\mathbf{E}^i(\mathbf{r}) + \mathbf{E}^s(\mathbf{r})]_{tan} = 0, \quad \mathbf{r} \in S_c \tag{2.6}$$

Substituting equation (2.5) into equation (2.4), the volume polarization current density in the dielectric substrate can be obtained as

$$\mathbf{J}_d(\mathbf{r}) = j\omega\varepsilon_o\,(\varepsilon_r\text{-}1)[\mathbf{E}^i(\mathbf{r}) + \mathbf{E}^s(\mathbf{r})]\,, \quad \mathbf{r} \in V_d \tag{2.7}$$

At the conductor/dielectric boundary, the normal component of the resultant electric displacement field is equal to the free surface charge density $\rho_f(\mathbf{r})$.

$$[\mathbf{D}^i(\mathbf{r}) + \mathbf{D}^s(\mathbf{r})]_{norm} = \rho_f(\mathbf{r}), \quad \mathbf{r} \in S_c \cap V_d \tag{2.8}$$

where

$\mathbf{E}^i(\mathbf{r})$ is the known incident electric field at $\mathbf{r}$

$\mathbf{E}^s(\mathbf{r})$ is the unknown scattered electric field at $\mathbf{r}$ and equal to $\mathbf{E}_c^s(\mathbf{r}) + \mathbf{E}_d^s(\mathbf{r})$

$\mathbf{E}_c^s(\mathbf{r})$ is the electric field scattered by the conductor of the PCB at $\mathbf{r}$

$\mathbf{E}_d^s(\mathbf{r})$ is the electric field scattered by the dielectric substrate of the PCB at $\mathbf{r}$

$\mathbf{D}^i(\mathbf{r})$ is the known impressed electric flux density at $\mathbf{r}$

$\mathbf{D}^s(\mathbf{r})$ is the unknown scattered electric flux density at $\mathbf{r}$

$\mathbf{r}$ is the position vector at the observation point

ε_r is the relative permittivity of the dielectric substrate

$\rho_f(\mathbf{r})$ is the conductor/dielectric boundary's free surface charge density at $\mathbf{r}$.

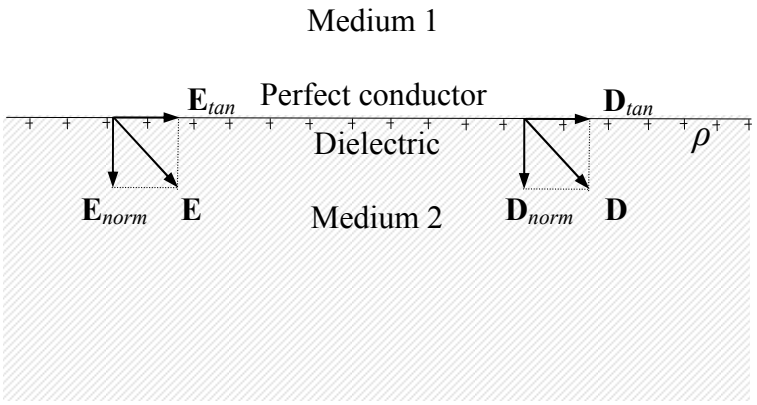

Fig. 2.3 Boundary illustration of conductor/dielectric

From Gauss's law in Maxwell's equations formulation in terms of total charge, the total surface charge density ρ is given by

$$\rho=\varepsilon_0[\mathbf{E}^i(\mathbf{r})+\mathbf{E}^s(\mathbf{r})]_{norm}, \quad \mathbf{r} \in S_c \cap V_d \tag{2.9}$$

Because the total charge density is the summation of free and bound surface charge density, bound surface charge density due to the polarisation effect can be calculated by

$$\rho_b=\varepsilon_0(\varepsilon_r-1)\,[\mathbf{E}^i(\mathbf{r})+\mathbf{E}^s(\mathbf{r})]_{norm}, \quad \mathbf{r} \in S_c \cap V_d \tag{2.10}$$

Combining equation (2.7) and (2.10), the bound surface charge density ρ_b can be related with the equivalence volume polarisation current $\mathbf{J}_d$ within the dielectric substrate and expressed as

$$\rho_b = \frac{[\mathbf{J}_d(\mathbf{r})]_{norm}}{j\omega}, \quad \mathbf{r} \in S_c \cap V_d \tag{2.11}$$

Rearranging equation (2.6) and (2.7), leads to

$$\mathbf{E}^i(\mathbf{r})_{tan} = -[\mathbf{E}_c^s(\mathbf{r})+\mathbf{E}_d^s(\mathbf{r})]_{tan}, \quad \mathbf{r} \in S_c \tag{2.12}$$

$$\mathbf{E}^i(\mathbf{r}) = \frac{\mathbf{J}_d(\mathbf{r})}{j\omega\varepsilon_o(\varepsilon_r-1)} - [\mathbf{E}_c^s(\mathbf{r})+\mathbf{E}_d^s(\mathbf{r})], \quad \mathbf{r} \in V_d \tag{2.13}$$

Substituting equation (2.11) into (2.10) with some rearrangement gives

$$\mathbf{E}^i(\mathbf{r})_{norm} = \frac{\mathbf{J}_d(\mathbf{r})_{norm}}{j\omega\varepsilon_o(\varepsilon_r - 1)} - \left[\mathbf{E}_c^s(\mathbf{r}) + \mathbf{E}_d^s(\mathbf{r})\right]_{norm}, \qquad \mathbf{r} \in S_c \cap V_d \tag{2.14}$$

where

$\mathbf{E}^i(\mathbf{r})_{tan}$ is the known incident tangential electric field on the 2D conducting surface

$\mathbf{E}^i(\mathbf{r})$ is the known incident electric field within the 3D substrate

$\mathbf{E}^i(\mathbf{r})_{norm}$ is the known incident normal electric field at the conductor/substrate boundary

$\mathbf{J}_d(\mathbf{r})$ is the 3D polarisation current density within the substrate

$\mathbf{J}_d(\mathbf{r})_{norm}$ is the 3D normal polarisation current density at the conductor/substrate boundary

E_{tan} is the scalar tangential electric field at the conductor/substrate boundary

E_{norm} is the scalar normal electric field at the conductor/substrate boundary

S_c is the 2D area occupied by the conductor

V_d is the 3D volume occupied by the substrate

$S_c \cap V_d$ is the conductor/substrate boundary

ω is the angular frequency

ε_o is the free space permittivity (8.854×10^{-12} F/m)

ε_r is the relative permittivity of the dielectric substrate

The electric fields $\mathbf{E}_c^s(\mathbf{r})$ and $\mathbf{E}_d^s(\mathbf{r})$ scattered by the conductor and the substrate can be expressed in terms of their respective magnetic vector potentials and electric scalar potentials given as follows

$$\mathbf{E}_c^s(\mathbf{r}) = -(\nabla\phi_c(\mathbf{r}) + j\omega\mathbf{A}_c(\mathbf{r})) \tag{2.15}$$

$$\mathbf{E}_d^s(\mathbf{r}) = -(\nabla\phi_d(\mathbf{r}) + j\omega\mathbf{A}_d(\mathbf{r})) \tag{2.16}$$

The magnetic vector potentials and electric scalar potentials can be obtained using d'Alembert formula

$$\phi_c(\mathbf{r}) = \frac{1}{4\pi\varepsilon_o}\iint_{S_c}\frac{\rho_c(\mathbf{r}')e^{-jk_0|\mathbf{r}-\mathbf{r}'|}}{|\mathbf{r}-\mathbf{r}'|}ds' \tag{2.17}$$

$$\mathbf{A}_c(\mathbf{r}) = \frac{\mu_o}{4\pi}\iint_{S_c}\frac{\mathbf{J}_c(\mathbf{r}')e^{-jk_0|\mathbf{r}-\mathbf{r}'|}}{|\mathbf{r}-\mathbf{r}'|}ds' \tag{2.18}$$

$$\begin{aligned}\phi_d(\mathbf{r}) = &\frac{1}{4\pi\varepsilon_o}\iiint_{V_d}\frac{\rho_d(\mathbf{r}')e^{-jk_0|\mathbf{r}-\mathbf{r}'|}}{|\mathbf{r}-\mathbf{r}'|}dv' \\ &+\frac{1}{4\pi\varepsilon_o}\iint_{S_c\cap V_d}\frac{\rho_b(\mathbf{r}')e^{-jk_0|\mathbf{r}-\mathbf{r}'|}}{|\mathbf{r}-\mathbf{r}'|}ds'\end{aligned} \tag{2.19}$$

$$\mathbf{A}_d(\mathbf{r}) = \frac{\mu_o}{4\pi}\iiint_{V_d}\frac{\mathbf{J}_d(\mathbf{r}')e^{-jk_0|\mathbf{r}-\mathbf{r}'|}}{|\mathbf{r}-\mathbf{r}'|}dv' \tag{2.20}$$

where

$\rho_c(\mathbf{r}')$ is the 2D surface charge density associated with $\mathbf{J}_c(\mathbf{r}')$

$\mathbf{J}_c(\mathbf{r}')$ is the 2D conduction current density on the 2D conductor surface

$\rho_d(\mathbf{r}')$ is the 3D volume charge density associated with $\mathbf{J}_d(\mathbf{r}')$

$\rho_b(\mathbf{r}')$ is the bound surface charge density

$\mathbf{J}_d(\mathbf{r}')$ is the 3D polarisation current density within the substrate

μ_o is the free space permeability ($4\pi\times10^{-7}$ H/m)

k_0 is the free space wave number and given as

$$k_o = \omega\sqrt{\mu_o\varepsilon_o} \tag{2.21}$$

The free space Green's function $G(\mathbf{r};\mathbf{r}')$ [81]–[83] is given by

$$G(\mathbf{r};\mathbf{r}') = \frac{e^{-jk_o|\mathbf{r}-\mathbf{r}'|}}{4\pi|\mathbf{r}-\mathbf{r}'|} \tag{2.22}$$

Using the continuity equation, the surface charge density at the conducting surface $\rho_c(\mathbf{r}')$ can be expressed in terms of $\mathbf{J}_c(\mathbf{r}')$ which is shown as

$$\rho_c(\mathbf{r}') = -\frac{\nabla' \cdot \mathbf{J}_c(\mathbf{r}')}{j\omega} \tag{2.23}$$

Similarly, the volume charge density within the substrate $\rho_d(\mathbf{r}')$ can be obtained using divergence of $\mathbf{J}_d(\mathbf{r}')$

$$\rho_d(\mathbf{r}') = -\frac{\nabla' \cdot \mathbf{J}_d(\mathbf{r}')}{j\omega} \tag{2.24}$$

Combining equations (2.11),(2.15)–(2.24), the scattered electric field $\mathbf{E}_c^s(\mathbf{r})$ and $\mathbf{E}_d^s(\mathbf{r})$ due to the conductor and substrate can be expressed in terms of $\mathbf{J}_d(\mathbf{r}')$ and $\mathbf{J}_d(\mathbf{r}')_{norm}$, respectively.

$$\mathbf{E}_c^s(\mathbf{r}) = \frac{\nabla}{j\omega\varepsilon_o}\iint_{S_c} \nabla' \cdot \mathbf{J}_c(\mathbf{r}')G(\mathbf{r};\mathbf{r}')ds' - j\omega\mu_o \iint_{S_c} \mathbf{J}_c(\mathbf{r}')G(\mathbf{r};\mathbf{r}')ds' \tag{2.25}$$

$$\begin{aligned}\mathbf{E}_d^s(\mathbf{r}) = {} & \frac{\nabla}{j\omega\varepsilon_o}\iiint_{V_d} \nabla' \cdot \mathbf{J}_d(\mathbf{r}')G(\mathbf{r};\mathbf{r}')dv' + \frac{\nabla}{j\omega\varepsilon_o}\iint_{S_c\cap V_d} \mathbf{J}_d(\mathbf{r}')_{norm}G(\mathbf{r};\mathbf{r}')ds' \\ & - j\omega\mu_o \iiint_{V_d} \mathbf{J}_d(\mathbf{r}')G(\mathbf{r};\mathbf{r}')dv'\end{aligned} \tag{2.26}$$

where

$\mathbf{r}'$ is the position vector at the source point

$\mathbf{J}_c(\mathbf{r}')$ is the 2D conduction current density on the 2D conductor surface

$\mathbf{J}_d(\mathbf{r}')$ is the 3D polarisation current density within the substrate

μ_r is the relative permeability of substrate

∇ is gradient operator

$\nabla' \cdot$ is divergence operator on the source function

To simplify the mathematical expressions, now we define a linear operators $L[\ ]$ which is related to the unknown current densities and the formulations are shown as follows

$$L\left[\mathbf{J}_c(\mathbf{r}')\right] = \frac{\nabla}{j\omega\varepsilon_o}\iint_{S_c}\nabla'\cdot\mathbf{J}_c(\mathbf{r}')G(\mathbf{r};\mathbf{r}')ds' - j\omega\mu_o\iint_{S_c}\mathbf{J}_c(\mathbf{r}')G(\mathbf{r};\mathbf{r}')ds' \tag{2.27}$$

$$L\left[\mathbf{J}_d(\mathbf{r}')\right] = \frac{\nabla}{j\omega\varepsilon_o}\iiint_{V_d}\nabla'\cdot\mathbf{J}_d(\mathbf{r}')G(\mathbf{r};\mathbf{r}')dv' - j\omega\mu_o\iiint_{V_d}\mathbf{J}_d(\mathbf{r}')G(\mathbf{r};\mathbf{r}')dv' \tag{2.28}$$

$$L\left[\mathbf{J}_d(\mathbf{r}')_{norm}\right] = \frac{\nabla}{j\omega\varepsilon_o}\iint_{S_c\cap V_d}\mathbf{J}_d(\mathbf{r}')_{norm}G(\mathbf{r};\mathbf{r}')ds' \tag{2.29}$$

Upon substituting equations (2.27)–(2.29) into equations (2.25) and (2.26), scattered electric field expressions can be simplified as

$$\mathbf{E}_c^s(\mathbf{r}) = L\left[\mathbf{J}_c(\mathbf{r}')\right] \tag{2.30}$$

$$\mathbf{E}_d^s(\mathbf{r}) = L\left[\mathbf{J}_d(\mathbf{r}')\right] + L\left[\mathbf{J}_d(\mathbf{r}')_{norm}\right] \tag{2.31}$$

By substituting (2.30) and (2.31) into equations (2.12)–(2.14), EFIEs can be expressed as follows [84]–[86]

$$\mathbf{E}^i(\mathbf{r})_{tan} = -L\left[\mathbf{J}_c(\mathbf{r}')\right] - L\left[\mathbf{J}_d(\mathbf{r}')\right] - L\left[\mathbf{J}_d(\mathbf{r}')_{norm}\right], \qquad \mathbf{r}\in S_c \tag{2.32}$$

$$\mathbf{E}^i(\mathbf{r}) = \frac{\mathbf{J}_d(\mathbf{r})}{j\omega\varepsilon_o(\varepsilon_r-1)} - L\left[\mathbf{J}_c(\mathbf{r}')\right] - L\left[\mathbf{J}_d(\mathbf{r}')\right] - L\left[\mathbf{J}_d(\mathbf{r}')_{norm}\right], \qquad \mathbf{r}\in V_d \tag{2.33}$$

$$\mathbf{E}^i(\mathbf{r})_{norm} = \frac{\mathbf{J}_d(\mathbf{r})_{norm}}{j\omega\varepsilon_o(\varepsilon_r-1)} - L\left[\mathbf{J}_c(\mathbf{r}')\right] - L\left[\mathbf{J}_d(\mathbf{r}')\right] - L\left[\mathbf{J}_d(\mathbf{r}')_{norm}\right], \qquad \mathbf{r}\in S_c\cap V_d \tag{2.34}$$

2.2 Numerical Solution of the EFIEs

To solve the EFIEs numerically, fist of all, the PCB needs to be subdivided into smaller sub-sections. Typical PCBs are of planar structures. Hence, it is convenient to subdivide a PCB along the *u*, *v* and *w* Cartesian coordinate axes into rectangular cells. As depicted in Fig. 2.4, the conductors can be subdivided into rectangular patches with dimensions: $du \times dv$, $du \times dw$, $dv \times dw$. And dielectric substrate can be discretized into rectangular cells with the sizes $du \times dv \times dw$. The size of each of these sub-sections *du*, *dv* and *dw* should not be larger than $\lambda/10$, where λ is the wavelength of the highest frequency of interest.

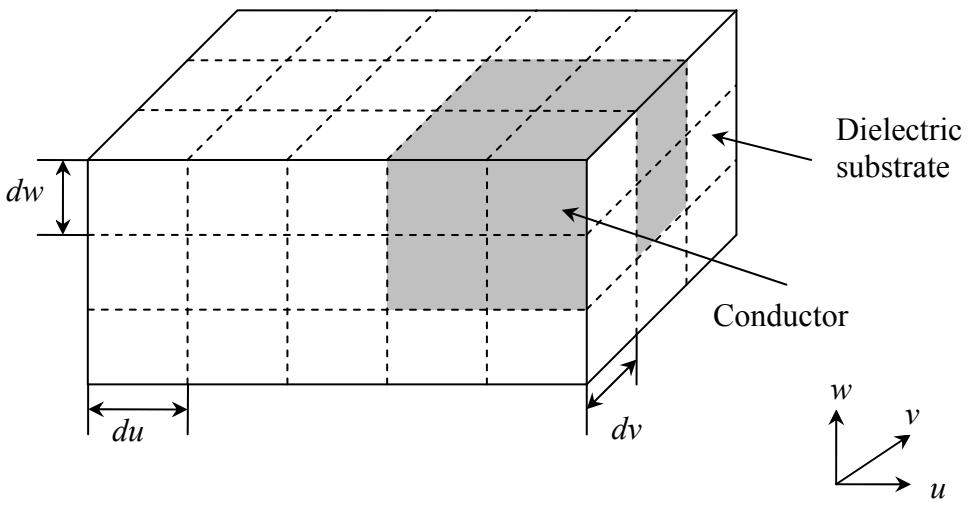

Fig. 2.4 Sub-divisions of a PCB

Once the structure is subdivided, the next step is to choose suitable basis functions to represent the current distributions on the conductor and within the substrate. Three possible basis functions and test functions combinations are illustrated in the Table 2.1

[87]. In case A, overlapping rooftop basis functions are selected to expand along the two components of the surface current and EFIEs are tested by using the same rooftop function, which is also known as Galerkin method [88]–[89]. In this situation, the differential operation in the current continuity equation results in a charge doublet for the given rooftop current basis function. In case B, rooftop basis function and line matching is used to solve the surface current distribution numerically. Case C is the simplest method where 2D pulse function is expanded to represent the surface current and associated charges are now line charges. Point matching on the centre of the segment is performed in the testing procedure.

Table 2.1 Some possible basic and test function choices defined over rectangular patch[87]

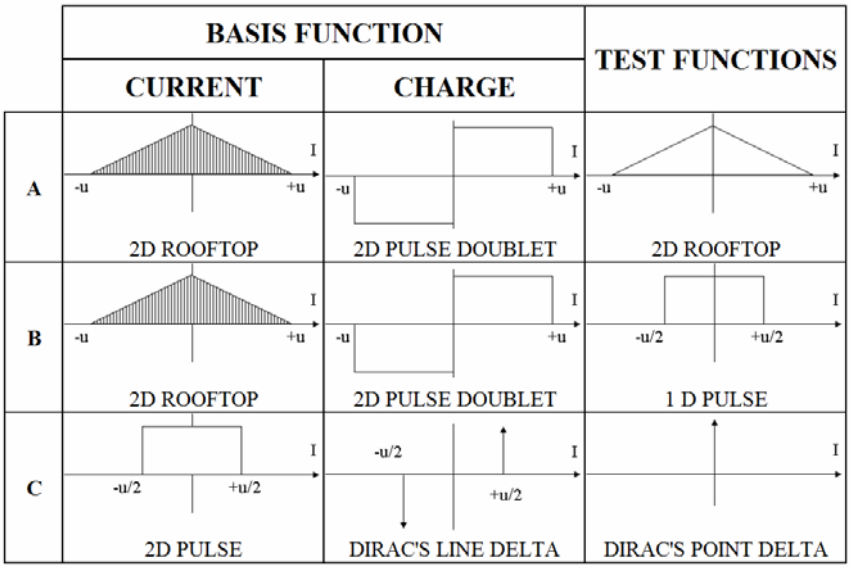

By choosing the basis functions of $\mathbf{J}_c(\mathbf{r}')$, $\mathbf{J}_d(\mathbf{r}')$ and $\mathbf{J}_d(\mathbf{r}')_{norm}$ to be $\boldsymbol{\beta}_c(\mathrm{r}')$, $\boldsymbol{\beta}_d(\mathrm{r}')$ and $\boldsymbol{\beta}_b(\mathrm{r}')$, respectively, the u-component of the known incident electric field on the conducting surface, within the dielectric substrate and at the conductor/dielectric boundary can be expressed in terms of the unknown complex current coefficients I_α, I_β and I_γ as

$$\mathbf{E}_u^i(\mathbf{r})_{tan} = -\sum_{\alpha=1}^{N_\alpha} \frac{I_\alpha}{\Delta v} L\left[\boldsymbol{\beta}_c{}^u\left(\mathbf{r}_\alpha{}'\right)\right]_{tan} - \sum_{\beta=1}^{N_\beta} \frac{I_\beta}{\Delta v \Delta w} L\left[\boldsymbol{\beta}_d{}^u\left(\mathbf{r}_\beta{}'\right)\right]_{tan} - \sum_{\gamma=1}^{N_\gamma} \frac{I_\gamma}{\Delta v \Delta w} L\left[\boldsymbol{\beta}_b{}^u\left(\mathbf{r}_\gamma{}'\right)\right]_{tan}$$

$$\mathbf{r}_\alpha{}', \mathbf{r} \in S_c \qquad \mathbf{r}_\beta{}' \in V_d \qquad \mathbf{r}_\gamma{}' \in S_c \cap V_d \tag{2.35}$$

$$\mathbf{E}_u^i(\mathbf{r}) = \frac{I_\beta \boldsymbol{\beta}_d{}^u(\mathbf{r})}{j\omega\varepsilon_o(\varepsilon_r - 1)} - \sum_{\alpha=1}^{N_\alpha} \frac{I_\alpha}{\Delta v} L\left[\boldsymbol{\beta}_c{}^u\left(\mathbf{r}_\alpha{}'\right)\right] - \sum_{\beta=1}^{N_\beta} \frac{I_\beta}{\Delta v \Delta w} L\left[\boldsymbol{\beta}_d{}^u\left(\mathbf{r}_\beta{}'\right)\right] - \sum_{\gamma=1}^{N_\gamma} \frac{I_\gamma}{\Delta v \Delta w} L\left[\boldsymbol{\beta}_b{}^u\left(\mathbf{r}_\gamma{}'\right)\right]$$

$$\mathbf{r}_\alpha{}' \in S_c \qquad \mathbf{r}_\beta{}', \mathbf{r} \in V_d \qquad \mathbf{r}_\gamma{}' \in S_c \cap V_d \tag{2.36}$$

$$\mathbf{E}_u^i(\mathbf{r})_{norm} = \frac{I_\gamma \boldsymbol{\beta}_b{}^u(\mathbf{r})}{j\omega\varepsilon_o(\varepsilon_r - 1)} - \sum_{\alpha=1}^{N_\alpha} \frac{I_\alpha}{\Delta v} L\left[\boldsymbol{\beta}_c{}^u\left(\mathbf{r}_\alpha{}'\right)\right]_{norm} - \sum_{\beta=1}^{N_\beta} \frac{I_\beta}{\Delta v \Delta w} L\left[\boldsymbol{\beta}_d{}^u\left(\mathbf{r}_\beta{}'\right)\right]_{norm} - \sum_{\gamma=1}^{N_\gamma} \frac{I_\gamma}{\Delta v \Delta w} L\left[\boldsymbol{\beta}_b{}^u\left(\mathbf{r}_\gamma{}'\right)\right]_{norm}$$

$$\mathbf{r}_\alpha{}' \in S_c \qquad \mathbf{r}_\beta{}' \in V_d \qquad \mathbf{r}_\gamma{}', \mathbf{r} \in S_c \cap V_d \tag{2.37}$$

where N_α N_β and N_γ are the total number of *u*-directed basis functions on the conducting surface, in the dielectric substrate and at the conductor/dielectric boundary respectively.

Through equations (2.27)–(2.29) and leaving out all the coefficients and constants, only two types of integral $\mathbf{g}_1(\mathbf{r};\mathbf{r}')$ and $\mathbf{g}_2(\mathbf{r};\mathbf{r}')$ are required to evaluate the right part of EFIEs given as

$$\mathbf{g}_1\left(\mathbf{r};\mathbf{r}'\right) = \int_{\beta_j} \boldsymbol{\beta}_j\left(\mathbf{r}'\right) G\left(\mathbf{r};\mathbf{r}'\right) d\beta_j \tag{2.38}$$

$$\mathbf{g}_2\left(\mathbf{r};\mathbf{r}'\right) = \nabla \int_{\beta_j} \nabla' \cdot \boldsymbol{\beta}_j\left(\mathbf{r}'\right) G\left(\mathbf{r};\mathbf{r}'\right) d\beta_j \tag{2.39}$$

where j = c, d or b and β_j is the region of integration of the basis function $\boldsymbol{\beta}_j(\mathbf{r}')$ which is called source region. By choosing $\theta_i(\mathbf{r})$ to be the test function and applying the MoM procedure [90]–[92], equations (2.38) and (2.39) become equations (2.40) and (2.41) respectively

$$Z_1\left(\mathbf{r};\mathbf{r}'\right) = \int_{\theta_i} \theta_i(\mathbf{r}) \int_{\beta_j} \boldsymbol{\beta}_j\left(\mathbf{r}'\right) G\left(\mathbf{r};\mathbf{r}'\right) d\beta_j d\theta_i \tag{2.40}$$

$$Z_2(\mathbf{r};\mathbf{r}') = \int_{\theta_i} \theta_i(\mathbf{r}) \nabla \int_{\beta_j} \nabla' \cdot \boldsymbol{\beta}_j(\mathbf{r}') G(\mathbf{r};\mathbf{r}') d\beta_j d\theta_i \tag{2.41}$$

where i = c, d or b and θ_i is the integration domain of the test function $\theta_i(\mathbf{r})$ which is called test region.

Finally, a full set of linear equations are formed which can be expressed in the matrix format as given in equation (2.42), where [V] represents the testing of known incident electric fields on the material and [I] denote the unknown complex coefficients of the selected basis functions [92]. The next chapter will describe the evaluation of the impedance matrix [Z] in an accurate and efficient way.

$$[V]=[Z][I] \tag{2.42}$$

2.3 Load impedance modeling

For most practical PCBs, the printed circuits are normally terminated with the known impedances. To handle such modeling problem, for example, a fixed load, $Z_{load} = R + jX$ is connected across points a and b of the conducting segment, as shown in Fig. 2.5. A delta gap is assumed to exist between the two segments so that the load is not short circuited.

In order to derive the tangential electric field expression on the segment, the load can be replaced by an equivalent surface impedance Z_s, as shown in Fig. 2.6. Therefore, the tangential electric field on the surface occupied by the patch is given by the multiplication of Z_s and current density J which can be written as

$$E_{tan} = Z_s J \tag{2.43}$$

Equation (2.43) can be modified and expressed in terms of the load voltage V and the load current I as follows

$$\frac{V}{\Delta w} = Z_s\left(\frac{I}{\Delta u}\right) \tag{2.44}$$

Rearranging equation (2.44) yields

$$V = \frac{Z_s \Delta w}{\Delta u} I \tag{2.45}$$

From equation (2.45), the relationship between the surface impedance Z_s and the load impedance Z_{load} can be obtained by the following expression.

$$Z_s = \frac{Z_{load} \Delta u}{\Delta w} \tag{2.46}$$

Testing the tangential electric field on the surface occupied by Z_s means to take the inner product between equation (2.46) and the test function, for example, 1D pulse test function. This will generate relevant generalized load impedance Z_L.

$$Z_L = \int_{\Delta w} Z_s dw = \int_{\Delta w} \frac{Z_{load} \Delta u}{\Delta w} dw = Z_{load} \Delta u \tag{2.47}$$

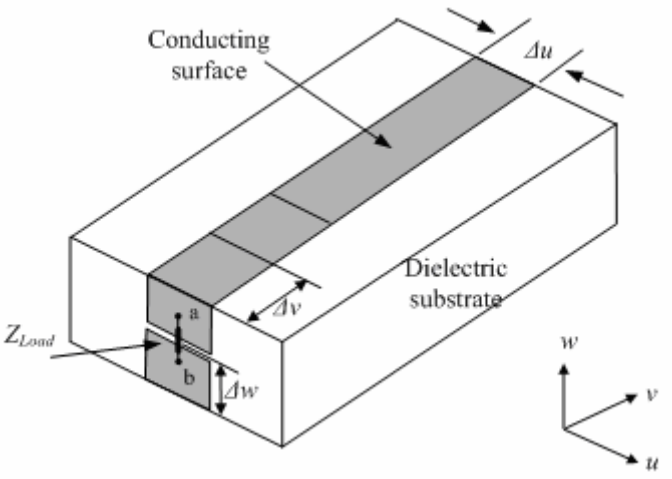

Fig. 2.5 Conducting strip terminated with a fixed load

From equation (2.47), it is observed that, Z_L can be determined by multiply Z_{load} and the width of the conducting segment that is connected to the load. If the j^{th} segment of the conducting surface is connected to the load, Z_L should be added to the diagonal element Z_{jj} of the generalized impedance sub-matrix $[Z_{cc}]$.

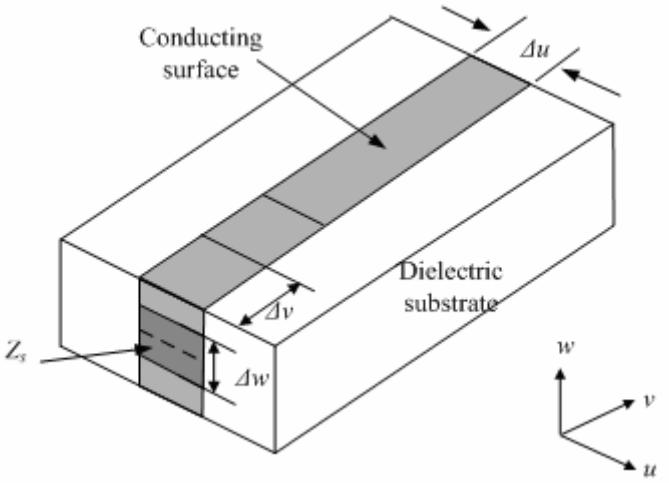

Fig. 2.6 Equivalent surface impedance

2.4 S-parameter characterization

Any circuit or system can be treated as a two-port network with well-defined pairs of input and output nodes. Network characterization is commonly used during PCB design. Elementary circuit theory provides us with many methods to describe the electronic networks but these methods, however, best describe DC and low-frequency behaviours of the circuits. At RF and microwave frequencies, when the wavelengths of the signals of interest shrink to become comparable to the physical dimensions of the circuit of interest, scattering parameters become extremely useful design aid. Therefore, a brief introduction of the S-parameter is given here.

If the input reflection coefficient S_{11} and the forward transmission coefficient S_{21} are the unknowns to be calculated, the circuit must be configured as a two port network as shown in Fig. 2.7. Each port is terminated with the port characteristic/reference

impedance, in most cases 50Ω, and AC voltage source at port 1 is set to 2V. Then based on the microwave theory, S-parameters can be defined with respect to incident travelling wave (a_1, a_2) and reflected wave (b_1, b_2) [93]–[94], which can be expressed as

$$a_1 = \frac{V_1 + Z_0 I_1}{2\sqrt{Z_0}} \qquad b_1 = \frac{V_1 - Z_0 I_1}{2\sqrt{Z_0}} \tag{2.48}$$

$$a_2 = \frac{V_2 + Z_0 I_2}{2\sqrt{Z_0}} \qquad b_2 = \frac{V_2 - Z_0 I_2}{2\sqrt{Z_0}} \tag{2.49}$$

S_{11} is equal to the ratio of reflected travelling wave b_1 and incident wave a_1 with a_2=0.

$$S_{11} = \left.\frac{b_1}{a_1}\right|_{a2=0} \tag{2.50}$$

Substituting (2.48) into (2.50) can obtain

$$S_{11} = \frac{V_1 - Z_0 I_1}{V_1 + Z_0 I_1} \tag{2.51}$$

Through the input network, we can get

$$V_1 = \frac{2Z_{in}}{Z_{in} + Z_0} \tag{2.52}$$

Considering $Z_{in}=V_1/I_1$, S_{11} can be determined using the following equation.

$$S_{11} = V_1 - 1 = 1 - 50 I_1 \tag{2.53}$$

Transmission coefficient S_{21} is equal to the ratio of reflected wave b_2 and incident wave a_1.

$$S_{21} = \left.\frac{b_2}{a_1}\right|_{a2=0} \tag{2.54}$$

Combining (2.49) and (2.50) then substituting into (2.54), we can obtain

$$S_{21} = \frac{V_2 - Z_0 I_2}{V_1 + Z_0 I_1} \tag{2.55}$$

Because S_{21} is defined under the condition that a_2=0, I_2 can be computed by $-V_2/Z_0$. Equation (2.55) is simplified as

$$S_{21} = \frac{2V_2}{V_1 + Z_0 I_1} \tag{2.56}$$

In the input network, the input current is related to the input voltage by

$$V_1 = Z_{in} I_1 \tag{2.57}$$

Substituting (2.57) into (2.56) obtains the final expression of the forward transmission coefficient S_{21}

$$S_{21} = V_2 = -50I_2 \tag{2.58}$$

Similarly, S_{22} and S_{12} can be extracted through terminating the output network with the AC 2V driving voltage source and characteristic impedance in series. Thus all S-parameters can be computed by the input and output currents.

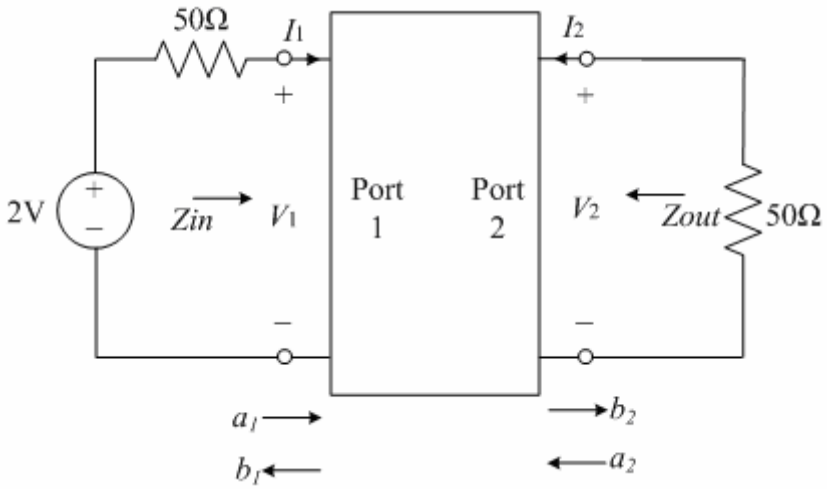

Fig. 2.7 Two-port network connected to compute S_{11} and S_{21}

2.5 Conclusions

Starting from the field equivalence theorem and integral equation approach, three coupled EFIEs were derived in order to model the finite-size PCB correctly. In the formulation, the electric scalar potential due to the bound surface charge at the conductor/dielectric boundary was also considered and included.

By employing the numerical discretization procedure, the PCB structures were subdivided into smaller patches and MoM method was employed to extract the impedance matrix and solve the unknown current distributions on the conductor and within the substrate. Also, the numerical implementation to model the circuit load and scattering parameters were discussed.

When solving the large-scale problems or complex PCB structures, a major concern is the impedance matrix filling time, as integration is the most time consuming step during the matrix element calculation. Its accuracy and efficiency will influence the computational efficiency and precision of the MoM codes. Hence, in the next chapter, the generalized analytical algorithm to accelerate the impedance matrix evaluation time will be discussed in depth.

CHAPTER THREE

3 EFFICIENT EVALUATION OF THE MOM IMPEDANCE MATRIX

MoM is well known for its dense impedance matrix and the singular nature of the Green's function. The total solution time of MoM consists of the matrix-fill time and the matrix-solution time, where the matrix-fill time is the time taken to evaluate and to fill all the elements in the impedance matrix and the matrix-solution time is the time taken to solve for the unknown current column matrix. Depending on the size of the impedance matrix, the matrix-fill time can contribute a significant part of the total solution time. As such, much research work on reducing the matrix-fill time has been carried out in recent years, for example, the interpolation method [49]–[52], the neural network method [53]–[55] and the analytical simplification method [56]–[58]. Although these methods evaluate the impedance matrix effectively, they sacrifice accuracy for efficiency. In order to preserve accuracy and still remains efficient, the analytical evaluation approach [59]–[60] is preferred. By using the analytical evaluation approach, time-consuming numerical integrations can be eliminated and the matrix-fill time can be greatly reduced. With the analytical approach, highly accurate evaluation of the impedance matrix where the singular point lies in the region of integration is also achievable.

In the previous chapter, the formulations of EFIEs have been discussed. By applying the MoM procedure to the EFIEs, the elements of the impedance matrix consists of two

main types of integrals, as indicated in equations (2.40) and (2.41). Depending on the selection of the basis and test functions, the order of integration may range from first-order to sixth-order and the impedance matrix can be ill-conditioned [45]–[47], which often requires very accurate evaluation of the elements of the impedance matrix. To achieve good overall solution accuracy, highly accurate evaluation of the diagonal elements of the impedance matrix is often required. Due to the singular nature of the Green's function, achieving accurate numerical integration of the Green's function (which contains singular point in the region of integration) will often sacrifice efficiency, i.e., higher order of numerical integration scheme is necessary.

In this chapter, a new efficient and accurate generalised analytical approach is adopted to speed up the evaluation of the impedance matrix elements. The analytical approach employed in this chapter has the flexibility of choosing any combination of basis and test functions, as long as their formulation can be expressed in polynomials form. In addition, it is capable of handling any order of integrations. Although the double and triple integrations using analytical expressions have been reported [59]–[60], analytical expression for higher order integration has not been investigated. Thus, the major contribution of this thesis is to develop the full analytical expressions to evaluate higher-order integrals accurately, up to sixth or even higher order, if necessary.

3.1 Taylor's Series Expansion of Free-Space Green's Function

The major challenge to calculate the elements of an impedance matrix is to evaluate accurately the integration of free-space Green's function $G(\mathbf{r};\mathbf{r}')$, which is given by

$$G(\mathbf{r};\mathbf{r}') = \frac{e^{-jk_oR}}{4\pi R} \tag{3.1}$$

where the free-space wave number is $k_o = \omega\sqrt{\mu_o\varepsilon_o}$, (u_i, v_i, w_i) is the observation point, (u_j, v_j, w_j) is the source point and $R = \sqrt{(u_i - u_j)^2 + (v_i - v_j)^2 + (w_i - w_j)^2}$.

To evaluate the integral of $G(\mathbf{r};\mathbf{r}')$ efficiently with good accuracy, analytical expression of the integral of $G(\mathbf{r};\mathbf{r}')$ is often required, especially when the singular point lies within the region of integration. Mathematically, direct integration of $G(\mathbf{r};\mathbf{r}')$ is not readily available; hence, approximated analytical approach is developed to evaluate the analytical expressions. By expanding $G(\mathbf{r};\mathbf{r}')$ in Taylor's series, the accuracy of the integration can be controlled within a specific precision.

$$\frac{e^{-jk_oR}}{4\pi R} \approx \frac{1}{4\pi}\sum_{p=0}^{n}\frac{(-j)^p k_o^p R^{p-1}}{p!} \tag{3.2}$$

From equation (3.2), one can observe that the only function to be integrated is R^p and since the analytical expression of the integral of R^p is obtainable, the analytical expression of the integral of $G(\mathbf{r};\mathbf{r}')$ can be evaluated. However, the use of equation (3.2) is limited to small k_oR because large k_oR will result in slow convergence or the result may not converge at all. Hence, $G(\mathbf{r};\mathbf{r}')$ should be expanded in Taylor's series around R_o, where R_o is the distance between centre of the source region and the test region.

$$\frac{e^{-jk_oR}}{4\pi R} \approx \frac{e^{-jk_oR_o}}{4\pi R} \sum_{p=0}^{n} \frac{(-j)^p k_o^p (R-R_o)^p}{p!} \tag{3.3}$$

In this case, equation (3.3) can still converge with very large k_oR as long as $k_o(R- R_o)$ is sufficiently small. Generally, $|R- R_o|$ is only a fraction of the wavelength and $k_o(R- R_o)$ will be sufficiently small. Hence, equation (3.3) can be a very good approximation of the $G(\mathbf{r};\mathbf{r}')$ with only a few terms. To determine error bound by the integral of equation (3.3) with different combinations of the source and test functions, the expressions for maximum $|R- R_o|$ are derived. Assuming Δu_i, Δu_j, Δv_i, Δv_j, Δw_i, and Δw_j are all equal to $m\lambda$ (where m is a scaling factor and λ is the wavelength of the EM wave), Fig. 3.1, Fig. 3.2, Fig. 3.3, Fig. 3.4 and Fig. 3.5 show that the maximum $|R-R_o|$ is 0, $m\lambda/2$, $m\lambda/\sqrt{2}$, $\sqrt{3}m\lambda/2$ and $m\lambda$, for the various possible source and test regions, respectively. In Fig. 3.1 to Fig. 3.5, (u_{io},v_{io},w_{io}) is the centre of test region, (u_{jo},v_{jo},w_{jo}) is the centre of source region and 0D, 1D, 2D and 3D represent point, line interval, surface patch and volumic cell respectively. R is the distance between the source and test grid points. It can be observed that the maximum distance between R and R_o occurs when both (u_{io},v_{io},w_{io}) and (u_{jo},v_{jo},w_{jo}) lie on the same point. For instance, as shown in Fig. 3.1, the test point (u_i,v_i,w_i)=(u_{io},v_{io},w_{io}) and the source point (u_j,v_j,w_j) =(u_{jo},v_{jo},w_{jo}), hence, $R = R_o$, maximum $|R-R_o|$ equals zero. Typically, the maximum grid size uses in MoM is a tenth of wavelength, which is 0.1λ, therefore, maximum $|R-R_o|$ for different dimensions of source and test region are calculated and tabulated in Table 3.1.

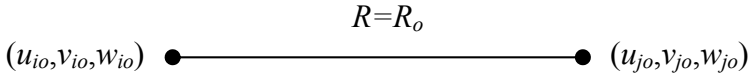

Fig. 3.1 Source point (0D) and test point (0D)

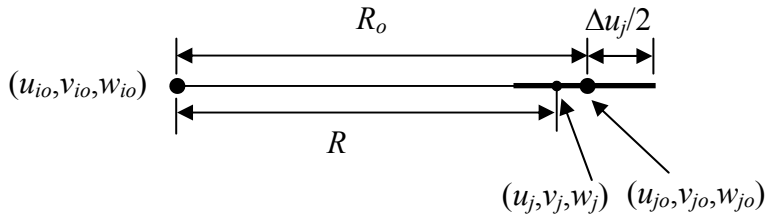

Fig. 3.2 Source interval (1D) and test point (0D)

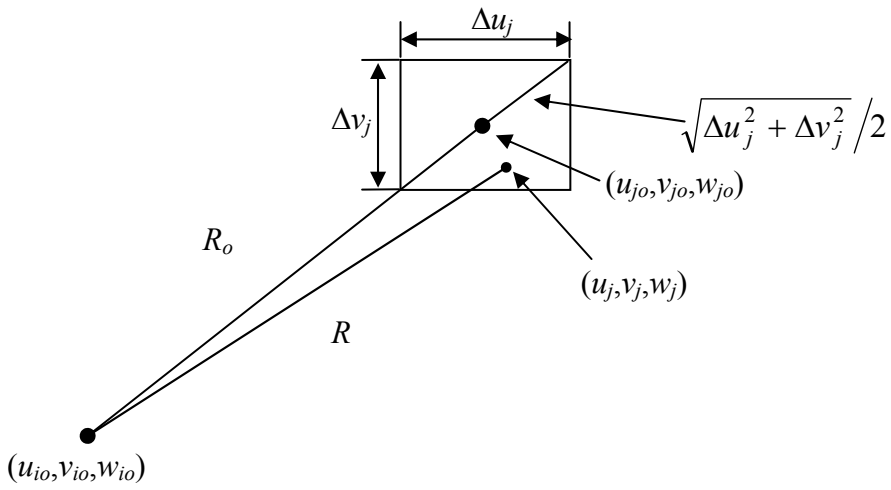

Fig. 3.3 Source patch (2D) and test point (0D)

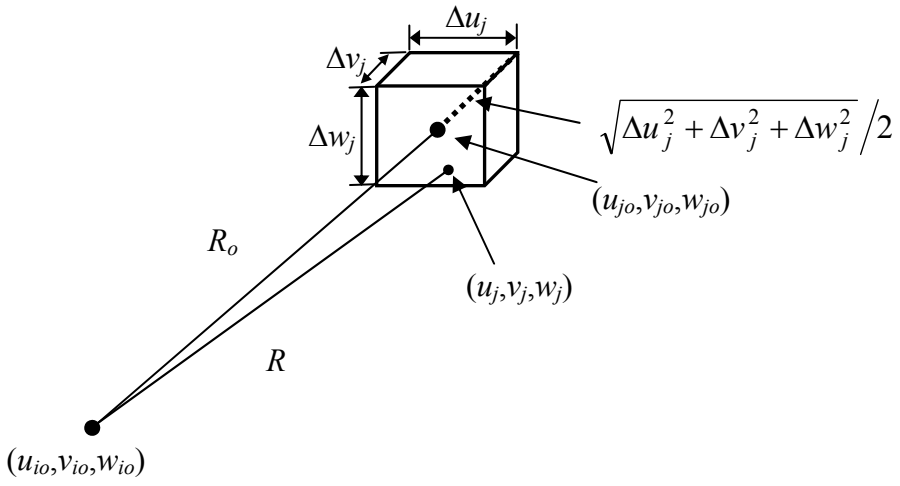

Fig. 3.4 Source cell (3D) and test point (0D)

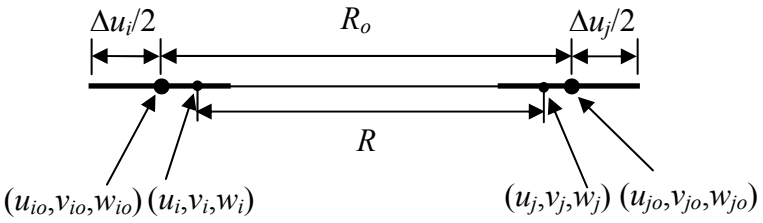

Fig. 3.5 Source interval (1D) and test interval (1D)

Table 3.1 Error bound of max|R-R_o|

Basis function/Test function	max|R-R_o|
point/point (0D/0D)	0
line/point (1D/0D)	0.05λ
surface/point (2D/0D)	$0.05\sqrt{2}\lambda$
volume/point (3D/0D)	$0.05\sqrt{3}\lambda$
line/line (1D/1D)	0.1λ
surface/line (2D/1D)	$0.05\sqrt{5}\lambda$
volume/line (3D/1D)	$0.05\sqrt{6}\lambda$
surface/surface (2D/2D)	$0.1\sqrt{2}\lambda$
volume/surface (3D/2D)	0.15λ
volume/volume (3D/3D)	$0.1\sqrt{3}\lambda$

The error bound of equation (3.3) depends on the number of terms to be included in calculation; the nth order error bound of equation (3.3) is given by

$$\textbf{error} \le \left|\frac{e^{-jk_oR_o}}{4\pi R}\right|\left|\frac{k_o^{n+1}(R-R_o)^{n+1}}{(n+1)!}\right| + O\left(R^{n+2}\right) \tag{3.4}$$

By assuming the maximum grid size for the structure in the modeling to be 0.1λ, Table 3.2 shows (in terms of percentages) the error bound of equation (3.3) for one-dimension basis function/one-dimension test function (1D/1D), two-dimension basis function/two-dimension test function (2D/2D) and three-dimension basis function/three-dimension test function (3D/3D) with various order, n. Other combinations of basis function and test function, such as 1D/2D, 1D/3D, etc, have different values of error bound than the three combinations listed in Table 3.2 and their error bound will lie between 0 (error bound of 0D/0D) to the error bound of 3D/3D.

Table 3.2 Error bound of equation (3.3)

Order n	1D/1D	2D/2D	3D/3D
0	62.8%	88.9%	109%
1	19.7%	39.5%	59.2%
2	4.13%	11.7%	21.5%
3	0.649%	2.60%	5.84%
4	0.0816%	0.462%	1.27%
5	0.00855%	0.0684%	0.231%
6	0.000767%	0.00868%	0.0359%

From Table 3.1 and Table 3.2, the worst error bound of equation (3.3) will be the 3D/3D case, and its error bound up to 5th order is 0.231%; it is sufficiently accurate for most engineering problems. However if better precision is required, equation (3.3) will be truncated till higher order terms. To rewrite equation (3.3) in terms of R^p rather than $(R\text{-}R_o)^p$, binomial expansion will be applied to $(R\text{-}R_o)^p$ of equation (3.3), which leads to equation (3.5).

$$\frac{e^{-jk_oR}}{4\pi R} \approx \frac{e^{-jk_oR_o}}{4\pi R} \sum_{p=0}^{n} \beta_p^{(n)}{}_p R^p \tag{3.5}$$

where

$$\beta_p^{(n)} = \sum_{m=p}^{n} (-1)^{2m-p} \frac{(j)^m k_o^m}{p!(m-p)!} R_o^{m-p} \tag{3.6}$$

With equation (3.5), the analytical expressions for the integrations of $G(\mathbf{r};\mathbf{r}')$ will be discussed in the next section in details.

3.2 Analytical Expressions for Integrals

From equation (3.5), it can observed that the only kind of integral involved is the integral of R^p and the lowest order integral of R^p is -1. Due to the fact that the solution of the integral of higher power order of R depends on the integral of R^{-1}, the solutions of $\int R^{-1} du$, where (u,v,w) is defined as the generalised Cartesian coordinate and $R = \sqrt{u^2 + v^2 + w^2}$, will be discussed in details. The variables u, v and w are defined as $u = u_i - u_j$, $v = v_i - v_j$ and $w = w_i - w_j$, respectively. Since R^{-1} contains a singular point when R =0, it imposes difficulty to evaluate $\int R^{-1} du$ accurately using numerical integration scheme, therefore, analytical approach is preferred. From the literature, there are four known analytical solutions for $\int R^{-1} du$ [95]–[98]

$$\int \frac{1}{R} du = \ln(R + u) \tag{3.7}$$

$$\int \frac{1}{R} du = -\ln(R - u) \tag{3.8}$$

$$\int \frac{1}{R} du = \sinh^{-1} \frac{u}{\sqrt{v^2 + w^2}} \tag{3.9}$$

$$\int \frac{1}{R} du = \tanh^{-1} \frac{u}{R} = \frac{1}{2} \ln \left| \frac{R+u}{R-u} \right| \tag{3.10}$$

Out of these four possible solutions, the closed-form expression given in equation (3.7) is the most common indefinite integral given in literature; not only it is the integral found in [95]–[97], it is also the solution given in commercial mathematical software like Maple [99] and Mathematica [100]. It is an appropriate expression for definite single integral, the resultant expressions of equations (3.7)–(3.10) are exactly the same. However, mathematically, it is not a good expression for indefinite integral. As stated in [98], since R is an even function of u, the indefinite integral of R^{-1} should be made odd function of u. Hence, equation (3.10), which is an odd function of u, is the recommended closed-form expression for the indefinite integral of R^{-1}. There is another further comment about equation (3.7); if it is used to evaluate the second integration with dv as the variable of integration, the resulting expression given in equation (3.11) is not symmetrical. Since R is symmetric function of u, v and w, double indefinite integral of R^{-1} should be symmetric function as well. As it can be observed in equation (3.11), two additional redundant terms $-v$ and $w\tan^{-1}(v/w)$ are identified. These additional terms will vanish once the limits of integration are imposed to equation (3.11).

$$\begin{aligned} \int\int \frac{1}{R} du dv &= \int \ln(u+R) dv \\ &= v\ln(u+R) - v + u\ln(v+R) - w\tan^{-1}\left(\frac{uv}{wR}\right) + w\tan^{-1}\left(\frac{v}{w}\right) \end{aligned} \tag{3.11}$$

On the other hand, the second integration of equation (3.10) with *dv* as the variable of integration will provide symmetric function with no redundant term, which is given as:

$$\begin{aligned}\iint \frac{1}{R} du dv &= \int \tanh^{-1}\frac{u}{R} dv \\ &= v\tanh^{-1}\frac{u}{R} + u\tanh^{-1}\frac{v}{R} - w\tan^{-1}\left(\frac{uv}{wR}\right)\end{aligned} \tag{3.12}$$

With equations (3.10) and (3.12), closed-form expressions for higher order integral of R^{-1} are possible.

From Chapter 2, equations (2.40) and (2.41) give the generalised form of the two kinds of integrals that are used to evaluate the elements of the impedance matrix of MoM. By choosing both the basis and test functions to be polynomial-type functions, only one kind of integration is required to solve, which is given as

$$g(u,v,w) = \int_{\Omega_T} \eta^p f(u,v,w) d\Omega_T \tag{3.13}$$

where

$$f(u,v,w) = \int_{\Omega_B} \gamma^m R^n d\Omega_B \tag{3.14}$$

where both γ and $\eta = u$, v or w, Ω_B is the integration domain for basis function and Ω_T is the integration domain for test function. The domain can be line (1D), area (2D) or volume (3D). Depending on whether *m* is odd number or even number, the integral of equation (3.14) have two different forms of integral expressions. If *m* is even number

and $m'=m/2$, $R^m = \left(R^2\right)^{m/2} = \left(u^2+v^2+w^2\right)^{m'}$ which is just a multi-variable polynomial. The integral of multi-variable polynomial is easily obtainable. However, when m is odd number, the integral is not as straight forward. By using integration by part, $\int u^m R^n du$ can be derived and the full expression can be found in Appendix A**,** equation (A.2). As it can be observed from equation (A.2), the full expression of $\int u^m R^n du$ requires the analytical expression of $\int R^n du$. Although the integral of $\int R^n du$ can be found from mathematical tables, the expression given in equation (A.1) is slightly different from the expression given in [96]. Again, due to the similar reason that $\int R^n du$ is an even function, the expression given in equation (A.1) uses arc hyperbolic tangent function instead of using logarithmic function.

Depending on the basis function, equation (3.14) can range from zero (point) to third (volume) order integration. Hence, double and triple integration of $u^m R^n$ should be obtained. As such, with the help of equations (A.3)–(A.7), equations (A.1) and (A.2) will be further integrated into the double and triple integrations, which are listed in equations (A.8)–(A.11). For simplicity, this thesis only provides the integrals until triple integration and leave out the fourth to sixth order integrations, which can be derived by making full use of equations (A.1)–(A.11).

As shown in equations (A.1)–(A.11), the integral expressions consist of logarithmic, arctangent and arc hyperbolic tangent functions. These functions are computationally expensive and should be avoided whenever possible. Hence, R^n should further expand in terms of Taylor's series around R_o [61].

$$a_\alpha(u',v',w') = R^\alpha \approx \sum_{m=0}^{N}\sum_{n=0}^{N-m}\sum_{p=0}^{N-m-n} A_{\alpha,mnp}\, u'^m\, v'^n\, w'^p \tag{3.15}$$

where N is the number of order truncated in the Taylor's series expansion, $R = \sqrt{(u_o+u')^2+(v_o+v')^2+(w_o+w')^2}$ and α is integer.

The coefficient $A_{\alpha,mnp}$ is defined as follow

$$A_{\alpha,mnp} = \frac{a_\alpha^{(m,n,p)}(u_o,v_o,w_o)}{m!\,n!\,p!}$$

where

$$a_\alpha^{(m,n,p)}(u_o,v_o,w_o) \equiv \frac{\partial^m \partial^n \partial^p}{\partial u'^m\, \partial v'^n\, \partial w'^p} a_\alpha(u_o,v_o,w_o)$$

With equation (3.15), R^α terms can now be easily integrated. However, due to singularity nature of equation (3.15), it cannot be used when the distance between observation point and source point is approaching zero. Table 3.3 defines the two regions that decide whether equation (3.15) (i.e. only simple mathematical functions) will be used in the integrals.

Table 3.3 Region definitions

Region I	Region II
R_o<2max(Δu_j,Δv_j,Δw_j)+max(Δu_i,Δv_i,Δw_i) (analytical expressions with logarithmic, arctangent and arc hyperbolic tangent functions are used in the integrals)	R_o≥2max(Δu_j,Δv_j,Δw_j)+max(Δu_i,Δv_i,Δw_i) (only simple mathematical functions are used in the integrals)

3.3 Computational Efficiency of the Evaluation of the Impedance Matrix

In MoM, there are many different implementations of basis and test functions. As long as the basis and test functions are polynomial-type functions, the analytical approach mentioned in the previous sections can be applied. To study the efficiency and accuracy of the evaluation of the impedance matrix, the triangular basis function and the line matching test function is chosen for the study. This combination of basis and test functions will be used in the rest of the thesis for consistency. The triangular basis functions for 2D conduction current density on the 2D conductor surface $\Lambda_\alpha^u\left(\mathbf{r}_\alpha^{'}\right)$, 3D polarisation current density within the substrate $\tau_\beta^u\left(\mathbf{r}_\beta^{'}\right)$ and 3D normal polarisation current density at the conductor/substrate boundary $\tau_\gamma^u\left(\mathbf{r}_\gamma^{'}\right)$ are given as

$$\Lambda_\alpha^u\left(\mathbf{r}_\alpha^{'}\right)=\begin{cases}1-\dfrac{\left|u^{'}-u_\alpha^{'}\right|}{\Delta u}, & -\Delta u\le u^{'}-u_\alpha^{'}\le\Delta u,-\dfrac{\Delta v}{2}\le v^{'}-v_\alpha^{'}\le\dfrac{\Delta v}{2},w^{'}=w_\alpha^{'}\\ 0, & \text{otherwise}\end{cases} \tag{3.16}$$

$$\tau_\beta^u\left(\mathbf{r}_\beta^{'}\right)=\begin{cases}1-\dfrac{\left|u^{'}-u_\beta^{'}\right|}{\Delta u}, & -\Delta u\le u^{'}-u_\beta^{'}\le\Delta u,-\dfrac{\Delta v}{2}\le v^{'}-v_\beta^{'}\le\dfrac{\Delta v}{2},\\ & -\dfrac{\Delta w}{2}\le w^{'}-w_\beta^{'}\le\dfrac{\Delta w}{2}\\ 0, & \text{otherwise}\end{cases} \tag{3.17}$$

$$\tau_\gamma^u\left(\mathbf{r}_\gamma^{'}\right)=\begin{cases}1-\dfrac{u^{'}-u_\gamma^{'}}{\Delta u}, & 0\le u^{'}-u_\gamma^{'}\le\Delta u,-\dfrac{\Delta v}{2}\le v^{'}-v_\gamma^{'}\le\dfrac{\Delta v}{2},\\ & -\dfrac{\Delta w}{2}\le w^{'}-w_\gamma^{'}\le\dfrac{\Delta w}{2}\\ 0, & \text{otherwise}\end{cases} \tag{3.18}$$

With the selected triangular basis functions, it is useful to derive the divergence of the basis functions before substituting the basis functions to equation (2.41), as it contains divergence of the basis function. The divergence of the triangular basis functions are pulse functions. There are two types of pulse functions (2D and 3D) required and they are given as

$$\Pi_{2\mathrm{D}}^{u}\left(\mathbf{r}_{2\mathrm{D}}^{'}\right)=\begin{cases}1, & -\frac{\Delta u}{2}\le u^{'}-u_{2\mathrm{D}}^{'}\le\frac{\Delta u}{2},-\frac{\Delta v}{2}\le v^{'}-v_{2\mathrm{D}}^{'}\le\frac{\Delta v}{2},w^{'}=w_{2\mathrm{D}}^{'}\\ 0, & \text{otherwise}\end{cases} \tag{3.19}$$

$$\Pi_{3\mathrm{D}}^{u}\left(\mathbf{r}_{3\mathrm{D}}^{'}\right)=\begin{cases}1, & -\frac{\Delta u}{2}\le u^{'}-u_{3\mathrm{D}}^{'}\le\frac{\Delta u}{2},-\frac{\Delta v}{2}\le v^{'}-v_{3\mathrm{D}}^{'}\le\frac{\Delta v}{2},\\ & -\frac{\Delta w}{2}\le w^{'}-w_{3\mathrm{D}}^{'}\le\frac{\Delta w}{2}\\ 0, & \text{otherwise}\end{cases} \tag{3.20}$$

With these basis functions, only four different kinds of integration are needed. These are surface integration of 2D pulse (2DΠ) function ($I_{2\mathrm{D}\Pi}$), volume integration of 3D pulse (3DΠ) function ($I_{3\mathrm{D}\Pi}$), triple integration of half 2D triangular (2DΛ) function ($I_{2\mathrm{D}\Lambda}$) and quadruple integration of half 3D triangular (3DΛ) function ($I_{3\mathrm{D}\Lambda}$). Since the falling half triangular functions are similar to the rising half triangular functions, only the rising half triangular functions are discussed in this thesis. Their mathematical expressions are given by

$$I_{2\mathrm{D}\Pi}=\frac{1}{4\pi}\int_{-\frac{\Delta v_j}{2}}^{\frac{\Delta v_j}{2}}\int_{-\frac{\Delta u_j}{2}}^{\frac{\Delta u_j}{2}}\frac{e^{-jk_oR}}{R}du_jdv_j \tag{3.21}$$

$$I_{3\mathrm{D}\Pi}=\frac{1}{4\pi}\int_{-\frac{\Delta w_j}{2}}^{\frac{\Delta w_j}{2}}\int_{-\frac{\Delta v_j}{2}}^{\frac{\Delta v_j}{2}}\int_{-\frac{\Delta u_j}{2}}^{\frac{\Delta u_j}{2}}\frac{e^{-jk_oR}}{R}du_jdv_jdw_j \tag{3.22}$$

$$I_{2D\Lambda} = \frac{1}{4\pi}\int_{-\frac{\Delta u_i}{2}}^{\frac{\Delta u_i}{2}}\int_{-\frac{\Delta v_j}{2}}^{\frac{\Delta v_j}{2}}\int_{-\frac{\Delta u_j}{2}}^{\frac{\Delta u_j}{2}} \frac{e^{-jk_oR}}{R}\left(\frac{1}{2}+\frac{u_j}{\Delta u_j}\right)du_j dv_j du_i \tag{3.23}$$

$$I_{3D\Lambda} = \frac{1}{4\pi}\int_{-\frac{\Delta u_i}{2}}^{\frac{\Delta u_i}{2}}\int_{-\frac{\Delta w_j}{2}}^{\frac{\Delta w_j}{2}}\int_{-\frac{\Delta v_j}{2}}^{\frac{\Delta v_j}{2}}\int_{-\frac{\Delta u_j}{2}}^{\frac{\Delta u_j}{2}} \frac{e^{-jk_oR}}{R}\left(\frac{1}{2}+\frac{u_j}{\Delta u_j}\right)du_j dv_j dw_j du_i \tag{3.24}$$

To verify the efficiency and accuracy of the proposed approach, *N*-point quadrature integration is used as a reference for comparison purposes. The details about the *N*-point quadrature integration can be found in Appendix B. In the study carried in this thesis, all simulations are done with a HP xw6600 workstation with Intel Xeon 3 GHz CPU. The computation time for different orders of Taylor's series expansion in equation (3.5) (from 0 to 5th order) in both region I and II are tabulated in Table 3.4. For comparison purposes, different *N*-point quadrature integrations (*N* = 2, 4, 6, 8, 10, 12, 14, 16, 18, 20, 32, 64, 128, 256, 512 and 1024) are tabulated as well.

Table 3.4 Comparison of computation time of analytical approach with *N*-point quadrature integration

Integration Method	2DΠ	2DΛ	3DΠ	3DΛ
Analytical Region I *n*=0	0.468 μs	1.320 μs	1.344 μs	4.37 μs
Analytical Region I *n*=1	0.484 μs	1.339 μs	1.359 μs	4.38 μs
Analytical Region I *n*=2	0.531 μs	1.671 μs	1.421 μs	5.78 μs
Analytical Region I *n*=3	0.546 μs	1.890 μs	1.437 μs	5.78 μs
Analytical Region I *n*=4	0.609 μs	2.593 μs	1.578 μs	7.03 μs
Analytical Region I *n*=5	0.640 μs	2.652 μs	1.593 μs	7.65 μs
Analytical Region II *n*=0	0.250 μs	0.416 μs	0.328 μs	0.516 μs
Analytical Region II *n*=1	0.265 μs	0.438 μs	0.328 μs	0.546 μs
Analytical Region II *n*=2	0.281 μs	0.531 μs	0.343 μs	0.703 μs
Analytical Region II *n*=3	0.312 μs	0.586 μs	0.359 μs	0.859 μs
Analytical Region II *n*=4	0.328 μs	0.734 μs	0.391 μs	1.086 μs

Analytical Region II n=5	0.343 μs	0.892 μs	0.438 μs	1.156 μs
2-point Quadrature	0.47 μs	0.937 μs	0.875 μs	1.734 μs
4-point Quadrature	1.56 μs	6.87 μs	5.79 μs	25.31 μs
6-point Quadrature	3.43 μs	22.66 μs	19.53 μs	126.5 μs
8-point Quadrature	6.20 μs	53.10 μs	45.30 μs	391 μs
10-point Quadrature	9.30 μs	104.6 μs	89.10 μs	969 μs
12-point Quadrature	12.5 μs	179.7 μs	154.7 μs	2.016 ms
14-point Quadrature	18.7 μs	287.5 μs	246.9 μs	3.75 ms
16-point Quadrature	23.4 μs	422 μs	359 μs	6.40 ms
18-point Quadrature	29.7 μs	609 μs	515 μs	10.15 ms
20-point Quadrature	37.5 μs	828 μs	719 μs	15.62 ms
32-point Quadrature	93.0 μs	3.43 ms	2.81 ms	103.1 ms
64-point Quadrature	390 μs	27.34 ms	23.59 ms	1.64 s
128-point Quadrature	1.40 ms	221.9 ms	187.5 ms	26.375 s
256-point Quadrature	6.25 ms	1.75 s	1.5 s	421.174 s
512-point Quadrature	23.4 ms	14.015 s	12.078 s	6741.48 s
1024-point Quadrature	98.4 ms	112.219 s	96.545 s	107884.235 s

By denoting the analytical method in region I (AMI) with n order as AMI_n, the analytical method in region II (AMII) with n order as $AMII_n$, the N-point quadrature integration (QI) scheme as QI_N, computation time of AMI_n as t_{AMIn}, computation time of $AMII_n$ as t_{AMIIn} and computation time of QI_N as t_{QIN}, the explanation on the observation that follows will be more concise. There are a couple of phenomena that can be observed from Table 3.4 and they are summarized as follows:

- The computation time of AMI does not increase linearly as n increases; it increases at a much slower rate. The ratios of t_{AMI5} is to t_{AMI0} of 2DΠ, 2DΛ, 3DΠ and 3DΛ are only 1.37:1, 2.01:1, 1.19:1 and 1.75:1, respectively. It indicates that

improving the accuracy by increasing n does not suffer much computation time, which is a desirable feature if highly accurate solution is required.

- Similarly, the ratios of t_{AMII5} is to t_{AMII0} is 1.37, 2.14, 1.34 and 2.24 for 2DΠ, 2DΛ, 3DΠ and 3DΛ, respectively. Similarly, improving accuracy does not suffer much in computational efficiency.
- The ratios of t_{QI1024} is to t_{QI2} of 2DΠ, 2DΛ, 3DΠ and 3DΛ are 2.09×10^{5}, 1.2×10^{8}, 1.1×10^{8} and 6.22×10^{10}, respectively. It shows significant increase in computation time if better accuracy is needed. From the tabulated results, it can be observed that to improve the accuracy of 2DΠ, 2DΛ, 3DΠ and 3DΛ by doubling N will result in approximately 4 times, 8 times, 8 times and 16 times increase in the computation time, respectively. QI scheme become highly inefficient if large N is used to achieve the required accuracy.
- The QI_2 scheme is the least number of N that could be used to evaluate the diagonal element of the impedance matrix (which contains the singular point inside the region of integration). Although it is faster than all order of AMI, except AMI_0 of 2DΠ, the accuracy is far worse than AMI_n in most cases. On the other hand, $AMII_5$ is faster than QI_2 for 2DΠ, 2DΛ, 3DΠ and 3DΛ.
- From QI_4 scheme onwards, they are all slower than AMI and AMII, which does not offer any advantage in term of speed. Hence, AMI and AMII are very efficient when compared with the QI_4 to QI_{1024} scheme.

In conclusion, both AMI and AMII have been proven to be efficient in comparison to the traditional higher order QI scheme.

3.4 Accuracy of the Evaluation of the Impedance Matrix

To study the accuracy of AMI, AMII and the QI scheme, QI_{1024} is set as the reference and the absolute relative error is defined as

$$\text{absolute relative error} = \left| \frac{QI_{1024} - I_{res}}{QI_{1024}} \right| \times 100\% \tag{3.25}$$

where I_{res} is either AMI_n, $AMII_n$ or QI_N.

Analyses on the accuracy of $I_{2D\Pi}$, $I_{2D\Lambda}$, $I_{3D\Pi}$ and $I_{3D\Lambda}$ will be discussed in this section. Firstly, the accuracy of $I_{2D\Pi}$ will be discussed in greater details, in order to provide insights on how the AMI, AMII and QI schemes behave. Subsequently, the accuracy of $I_{2D\Lambda}$, $I_{3D\Pi}$ and $I_{3D\Lambda}$ will be discussed. Since a maximum grid size of 0.1λ is typically used in MoM, it will be adopted as the maximum grid size used in the following analyses.

To study the behaviour of the accuracy of $I_{2D\Pi}$, different combinations of (u_o,v_o,w_o), Δu and Δv are used. The first set of combination: $(u_o,v_o,w_o)=(0,0,0)$ and varying Δu and Δv, is used to study the accuracy of the different methods (AMI, AMII and QI) when the singular point resides in the region of integration (the diagonal elements of the impedance matrix), since high accuracy is required to evaluate the diagonal elements of the impedance matrix. Different $\Delta u/\Delta v$ ratios (1, 0.1 and 0.01) and different square cells ($\Delta u=\Delta v=0.1\lambda$, 0.01λ and 0.001λ) will be applied for the analyses. All other sets are similar to the first set except their positions (u_o,v_o,w_o) are different. The second set of combination: $(u_o,v_o,w_o)=(\Delta u,0,0)$, is chosen to study the behaviour when the source cell

is the neighbouring cell of the field cell and Δu is the shorter side of the cell. The third set of combination: $(u_o,v_o,w_o)=(0,\Delta v,0)$, is chosen to study the behaviour when the source cell is the neighbouring cell of the field cell, but with Δv is the longer side of the cell. The fourth set of combination: $(u_o,v_o,w_o)=(0,0,0.1\lambda)$, is chosen to study the behaviour when the source cell is directly above or below the field cell. The fifth set of combination: $(u_o,v_o,w_o)=(0,2\Delta v,0)$, is chosen to study the behaviour when the source cell is two cells away from the field cell with Δv as the longer side of the cell. The last set of combination: $(u_o,v_o,w_o)=(\Delta u,\Delta v,1\lambda)$, is chosen to study the behaviour when the source cell is far away from the field cell.

The real and imaginary parts of the impedance are compared between the AMI and QI schemes, with five different combinations of Δu and Δv for $(u_o,v_o,w_o)=(0,0,0)$ and they plotted in Fig. 3.6 to Fig. 3.10. AMII is not included in the figures because of its singular nature that will result in infinity, so it should not be used when $(u_o,v_o,w_o)=(0,0,0)$. From Fig. 3.6 to Fig. 3.10, both AMI and QI scheme will converge to the same point for both real part of the impedance (Z_r) and imaginary part of the impedance (Z_i). As it can be observed, the accuracy of Z_r increases steeply when N of QI_N increases, till the point that is close to the exact value. Then, the accuracy will start to increase slowly till it converges to the exact value. As for the AMI_n, the accuracy of Z_r converges quickly as n increases. The accuracy of Z_i remains to be almost constant for QI_N as N increases which means that even QI_2 scheme for Z_i is very accurate. On the other hand, Z_i in AMI converges quickly as n increases and it keeps to almost constant once $n\geq 3$.

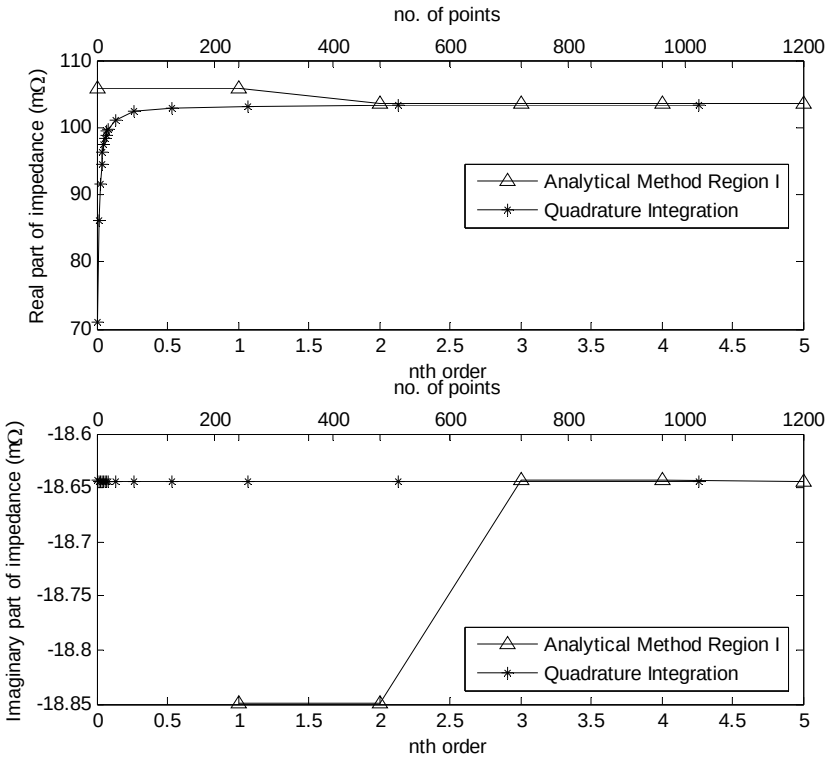

Fig. 3.6 Impedance of $I_{2D\Pi}$ versus n-th order of AMI and no. of QI points with $(u_o,v_o,w_o)=(0,0,0)$ and $\Delta u = \Delta v = 0.1\lambda$

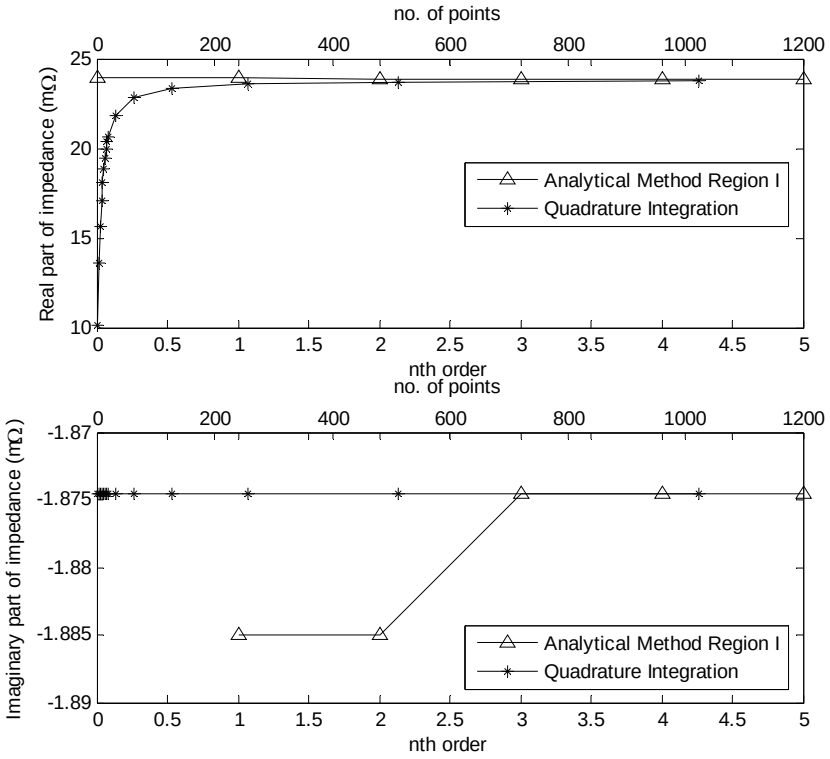

Fig. 3.7 Impedance of $I_{2D\Pi}$ versus n-th order of AMI and no. of QI points with $(u_o,v_o,w_o)=(0,0,0)$, $\Delta u=0.01\lambda$ and $\Delta v=0.1\lambda$

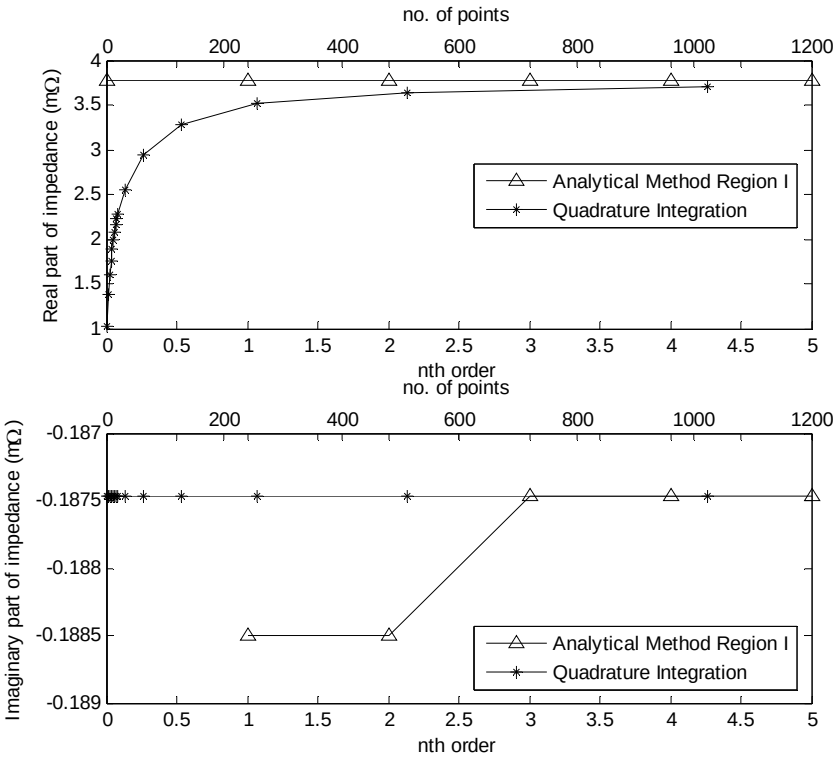

Fig. 3.8 Impedance of $I_{2D\Pi}$ versus n-th order of AMI and no. of QI points with (u_o,v_o,w_o)=(0,0,0), Δu=0.001λ and Δv=0.1λ

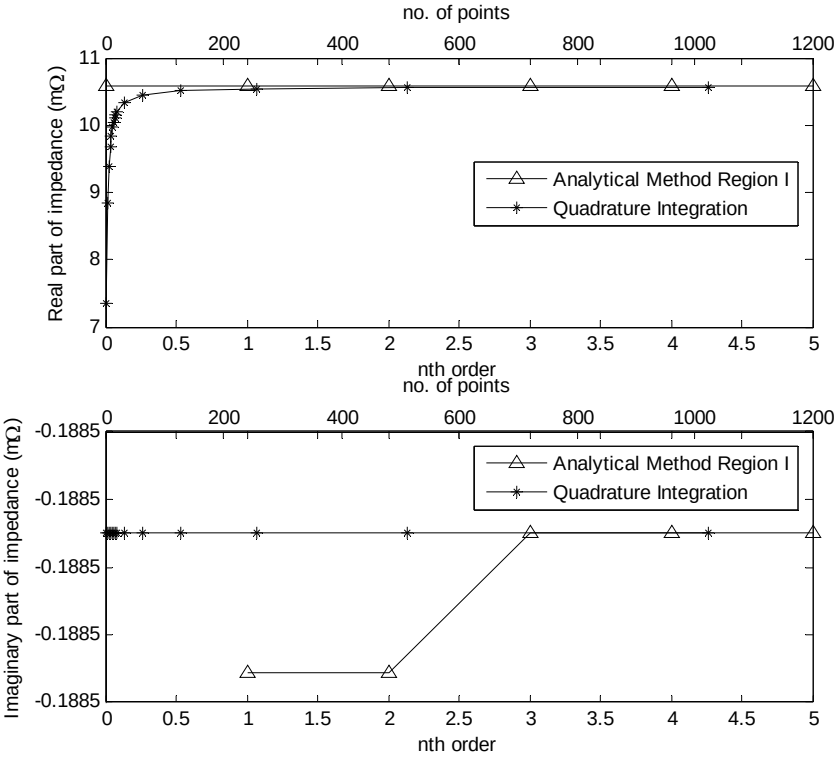

Fig. 3.9 Impedance of $I_{2D\Pi}$ versus n-th order of AMI and no. of QI points with (u_o,v_o,w_o)=(0,0,0), Δu=0.01λ and Δv=0.01λ

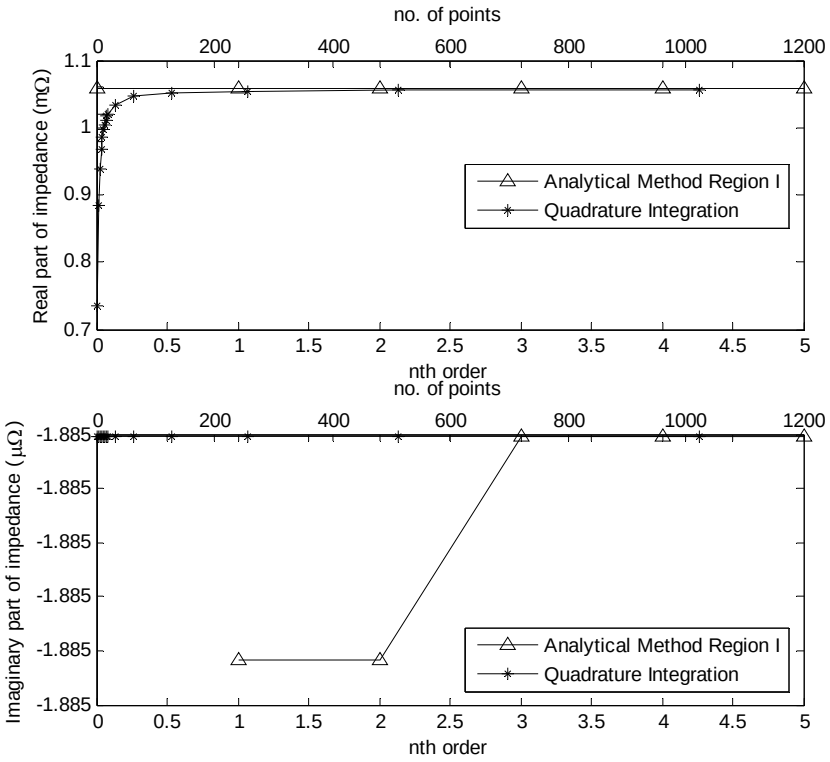

Fig. 3.10 Impedance of $I_{2D\Pi}$ versus n-th order of AMI and no. of QI points with $(u_o,v_o,w_o)=(0,0,0)$, $\Delta u=0.001\lambda$ and $\Delta v=0.001\lambda$

As it is difficult to determine the accuracy from Fig. 3.6 to Fig. 3.10, the absolute relative errors of Fig. 3.6 to Fig. 3.8 will plotted (in logarithmic scale) in Fig. 3.11 and Fig. 3.6, Fig. 3.9 and Fig. 3.10 will be plotted (in logarithmic scale) in Fig. 3.12. From Fig. 3.11, it can be observed that when $\Delta u/\Delta v$ ratios decreases, the absolute relative error also increases (0.07% for $\Delta u/\Delta v=1$, 0.27% for $\Delta u/\Delta v=0.1$ and 1.72% for $\Delta u/\Delta v=0.01$) for both AMI_5 and QI_{512}. Although, absolute relative error of AMI_5 and QI_{512} are almost similar, their relative errors are of different polarities. It can be observed from real parts of the impedance in Fig. 3.6 to Fig. 3.8, that both AMI and QI will converge to the same point, but the value of AMI is always larger than the value of QI. Another interesting observation is from Fig. 3.8, if the curve of QI is extrapolated to higher number of N of QI_N, the value will converge towards AMI_5. This shows that

when $\Delta u/\Delta v$ becomes very small in value, the QI scheme becomes much less accurate than AMI.

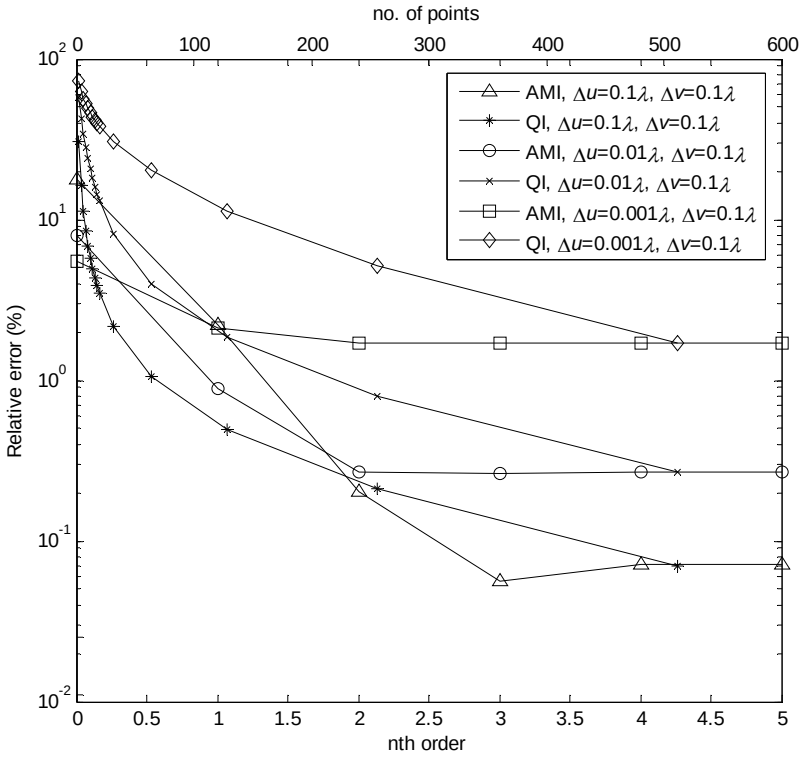

Fig. 3.11 Relative error of impedance of $I_{2D\Pi}$ versus n-th order of AMI and no. of QI points with (u_o,v_o,w_o)=(0,0,0), Δu=0.1λ, 0.01λ and 0.001λ, and Δv=0.1λ

From Fig. 3.12, it can be observed that when the ratio $\Delta u/\Delta v$ becomes unity, the absolute relative errors of QI are approximately similar. On the other hand, for AMI, larger Δu tends to converge faster than smaller Δu. Also, with just a few term of Taylor's series expansion, i.e., n of AMI_n is small (n = 0, 1 and 2 for Δu = 0.001λ, 0.01λ and 0.1λ, respectively), relative error of less than 1% can be achieved. With QI scheme, QI_{128} or higher order QI scheme is required to achieve relative error of less than 1%. Hence, AMI exhibits much better accuracy than QI when singular point resides within the region of integration.

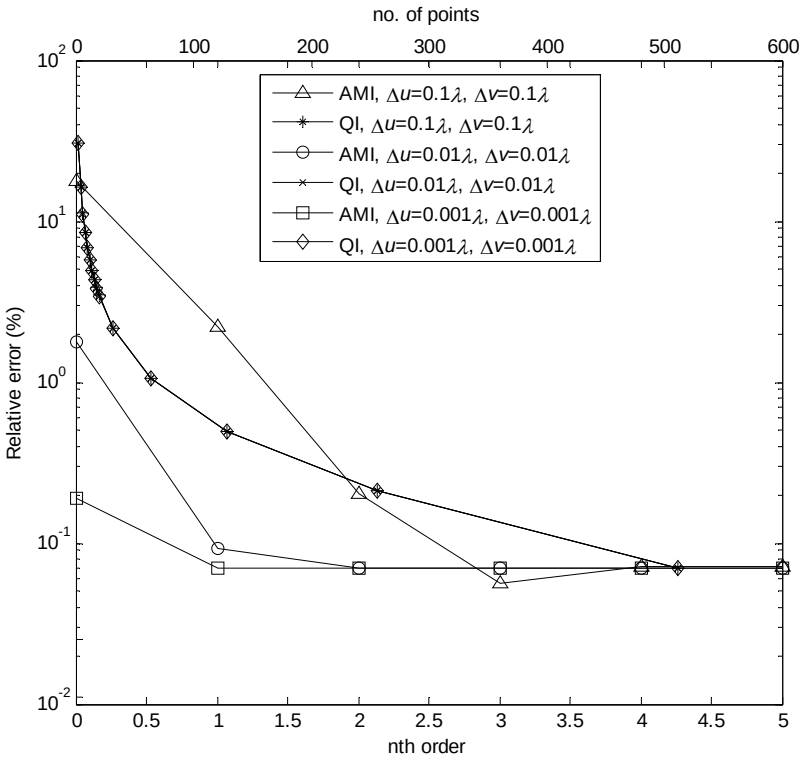

Fig. 3.12 Relative error of impedance of $I_{2D\Pi}$ versus n-th order of AMI and no. of QI points with (u_o,v_o,w_o)=(0,0,0), Δu=Δv, Δu=0.1λ, Δu=0.01λ and Δu=0.001λ

To investigate the accuracy of the integrals when the source cell is the neighbouring cell of the field cell, Fig. 3.13, Fig. 3.16 and Fig. 3.17 show the behaviours of the integrals when (u_o,v_o,w_o) = $(\Delta u,0,0)$ and Δu = Δv; Fig. 3.14 and Fig. 3.15 show the behaviours of the integrals when (u_o,v_o,w_o) = $(\Delta u,0,0)$ and Δu is the shorter side of the cell; Fig. 3.18 and Fig. 3.19 show the behaviours of the integrals when (u_o,v_o,w_o) = $(0,\Delta v,0)$ and Δv is the longer side of the cell. From Fig. 3.13, Fig. 3.16 and Fig. 3.17, it is clearly observed that when Δu = Δv, and R_o = Δu, the relative errors converge to the magnitude order of less than 10^{-2} % for AMII. As for AMI, the relative error reduces when Δu reduces; for QI_N scheme, the relative error converges rapidly as N increases. From Fig. 3.14 and Fig. 3.15, it shows that when R_o is much smaller than max(Δu,Δv), AMII becomes inaccurate and makes it unsuitable in this case; AMI works very well

even when R_o is much smaller than max(Δu,Δv); QI scheme converges much slower when R_o is much smaller than max(Δu,Δv). From Fig. 3.18 and Fig. 3.19, it shows that when $\Delta u << \Delta v$ and $R_o=\Delta v$, the relative errors converge to the magnitude order of less than 1% for AMII; AMI still maintains good accuracy and the relative error of QI_N scheme converges rapidly as N increases.

From the investigative study, it can be concluded that to obtain relative error of better than 1%, R_o>max(Δu,Δv) is required.

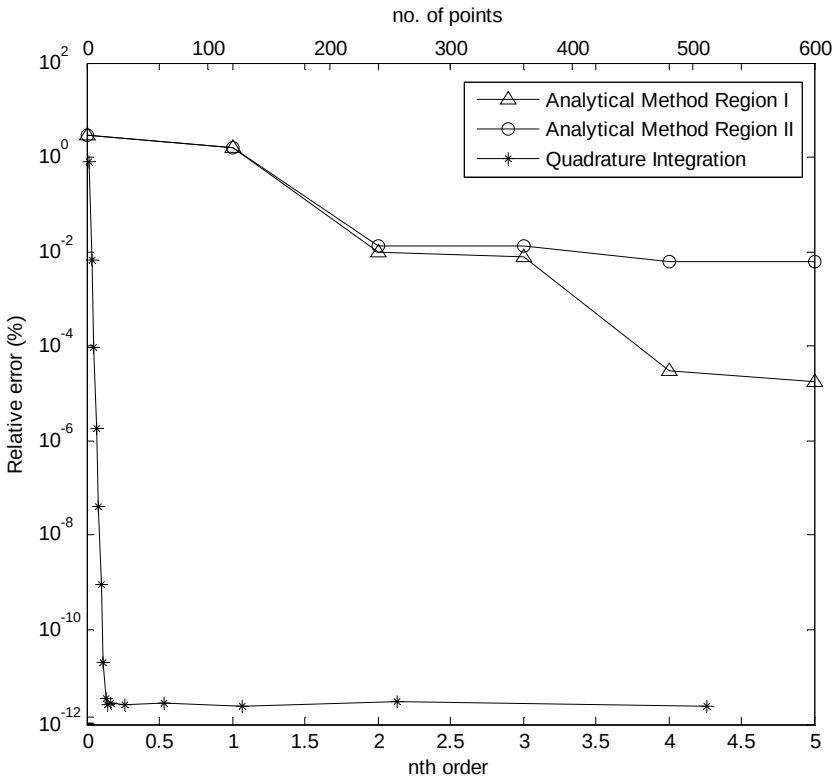

Fig. 3.13 Relative error of impedance of $I_{2D\Pi}$ versus n-th order of AMI and no. of QI points with $(u_o,v_o,w_o)=(0.1\lambda,0,0)$, $\Delta u=0.1\lambda$ and $\Delta v=0.1\lambda$

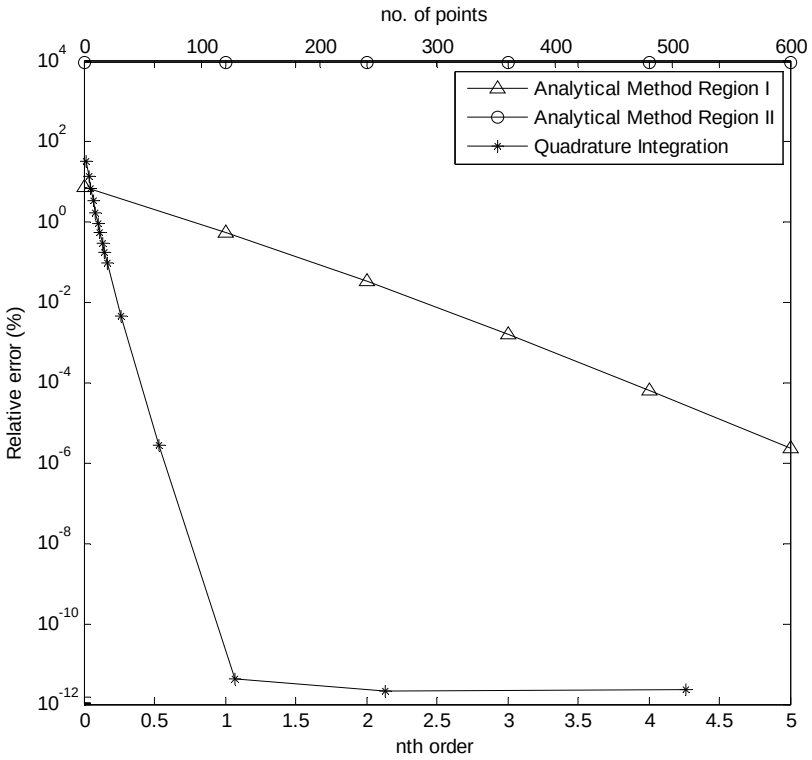

Fig. 3.14 Relative error of impedance of $I_{2D\Pi}$ versus n-th order of AMI and no. of QI points with $(u_o,v_o,w_o)=(0.01\lambda,0,0)$, $\Delta u=0.01\lambda$ and $\Delta v=0.1\lambda$

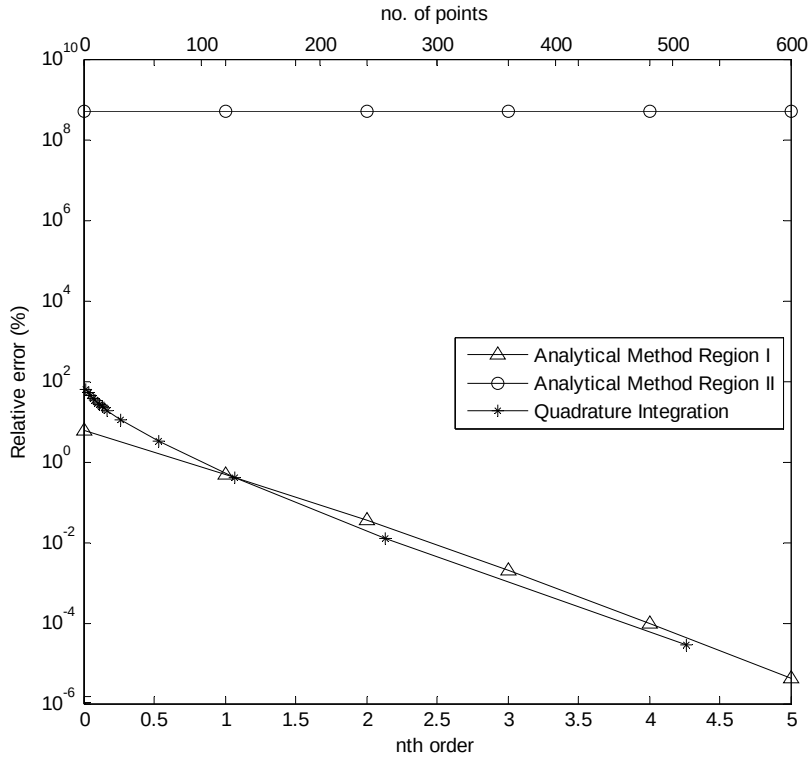

Fig. 3.15 Relative error of impedance of $I_{2D\Pi}$ versus n-th order of AMI and no. of QI points with $(u_o,v_o,w_o)=(0.001\lambda,0,0)$, $\Delta u=0.001\lambda$ and $\Delta v=0.1\lambda$

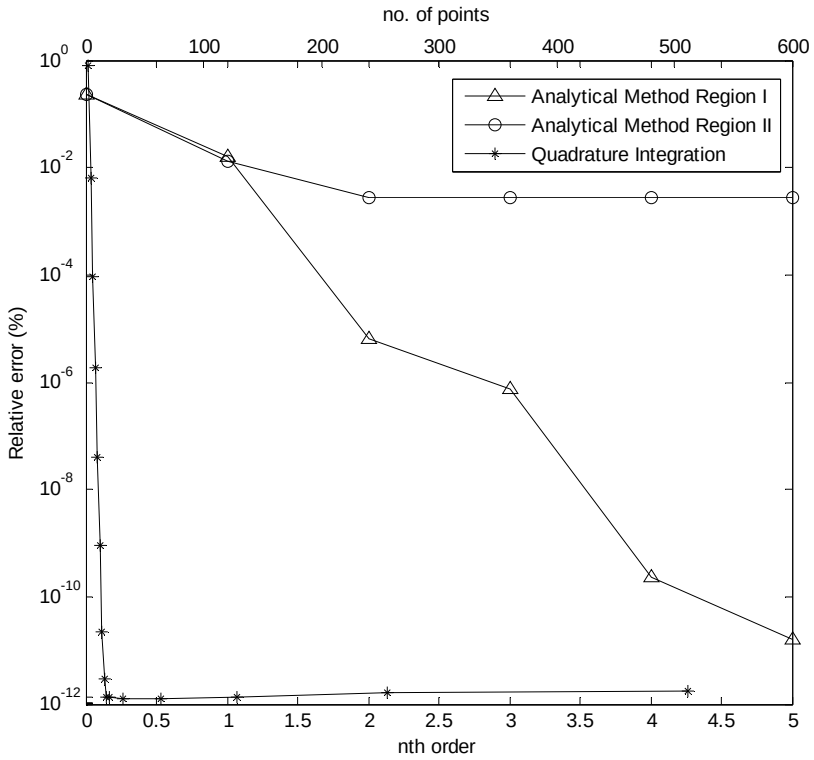

Fig. 3.16 Relative error of impedance of $I_{2D\Pi}$ versus n-th order of AMI and no. of QI points with $(u_o,v_o,w_o)=(0.01\lambda,0,0)$, $\Delta u=0.01\lambda$ and $\Delta v=0.01\lambda$

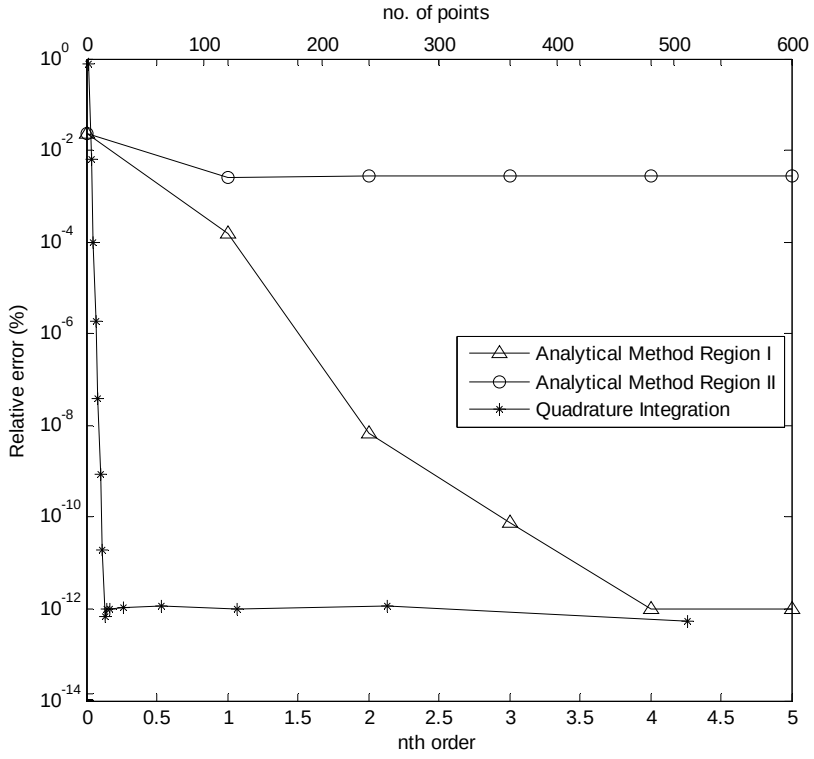

Fig. 3.17 Relative error of impedance of $I_{2D\Pi}$ versus n-th order of AMI and no. of QI points with $(u_o,v_o,w_o)=(0.001\lambda,0,0)$, $\Delta u=0.001\lambda$ and $\Delta v=0.001\lambda$

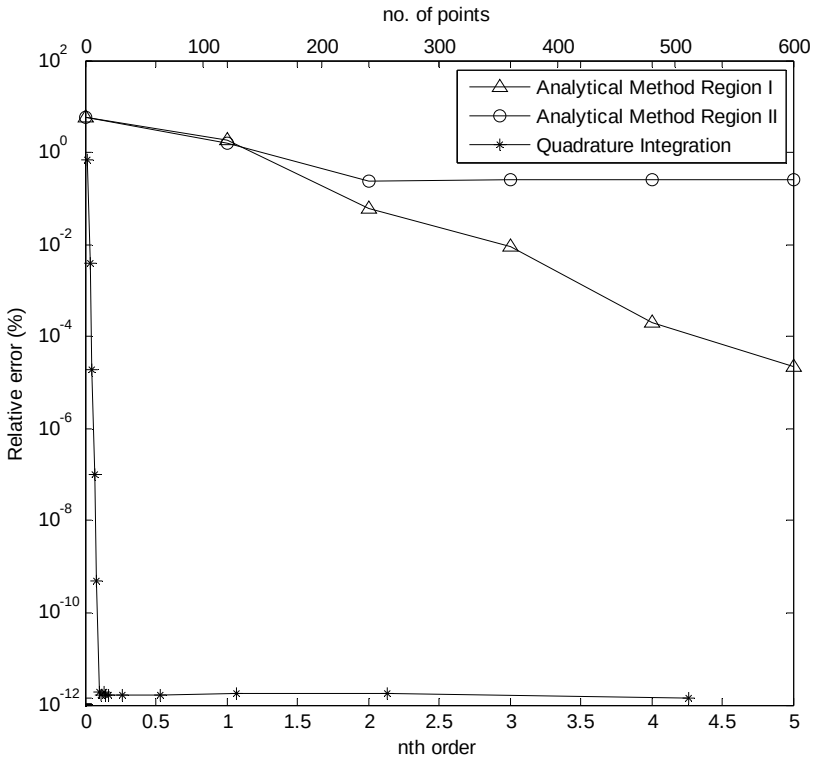

Fig. 3.18 Relative error of impedance of $I_{2D\Pi}$ versus n-th order of AMI and no. of QI points with $(u_o,v_o,w_o)=(0,0.1\lambda,0)$, $\Delta u=0.01\lambda$ and $\Delta v=0.1\lambda$

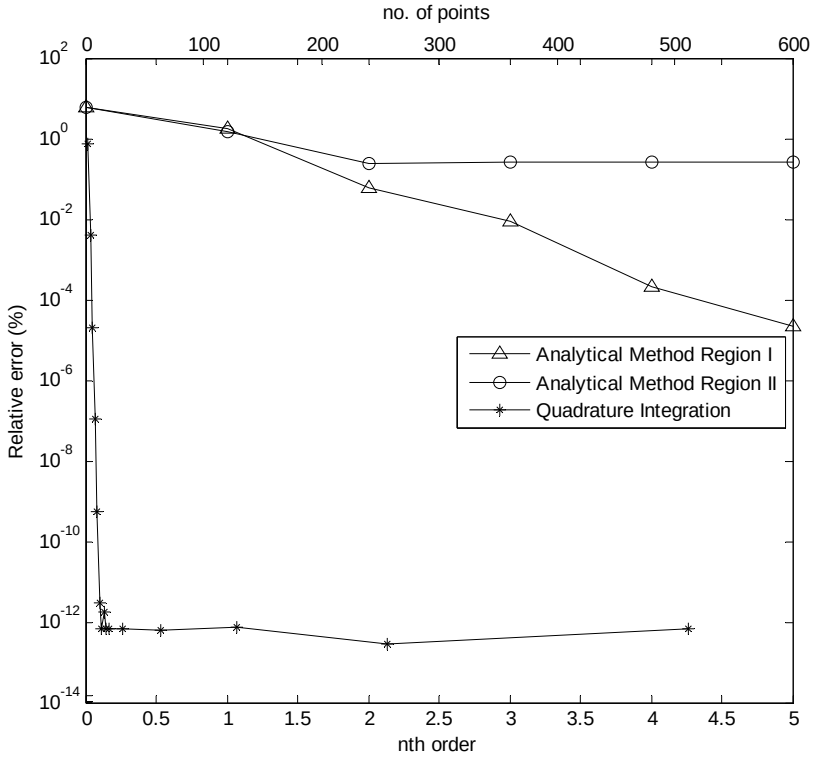

Fig. 3.19 Relative error of impedance of $I_{2D\Pi}$ versus n-th order of AMI and no. of QI points with $(u_o,v_o,w_o)=(0,0.1\lambda,0)$, $\Delta u=0.001\lambda$ and $\Delta v=0.1\lambda$

To investigate the accuracy of the integrals when the source cell is directly on top or below the field cell, Fig. 3.20 to Fig. 3.24 show the behaviours of the integrals when $(u_o,v_o,w_o)=(0,0,0.1\lambda)$. Both AMI and QI schemes work well when $(u_o,v_o,w_o)=(0,0,0.1\lambda)$ with maximum grid size of 0.1λ. However, the relative error of AMII is slightly less than 1% when $R_o=\Delta u=\Delta v$, and accuracy increases when R_o becomes large than $\max(\Delta u,\Delta v)$. Similarly conclusion can be deduced that the condition $R_o>\max(\Delta u,\Delta v)$ is necessary to obtain relative error of better than 1%.

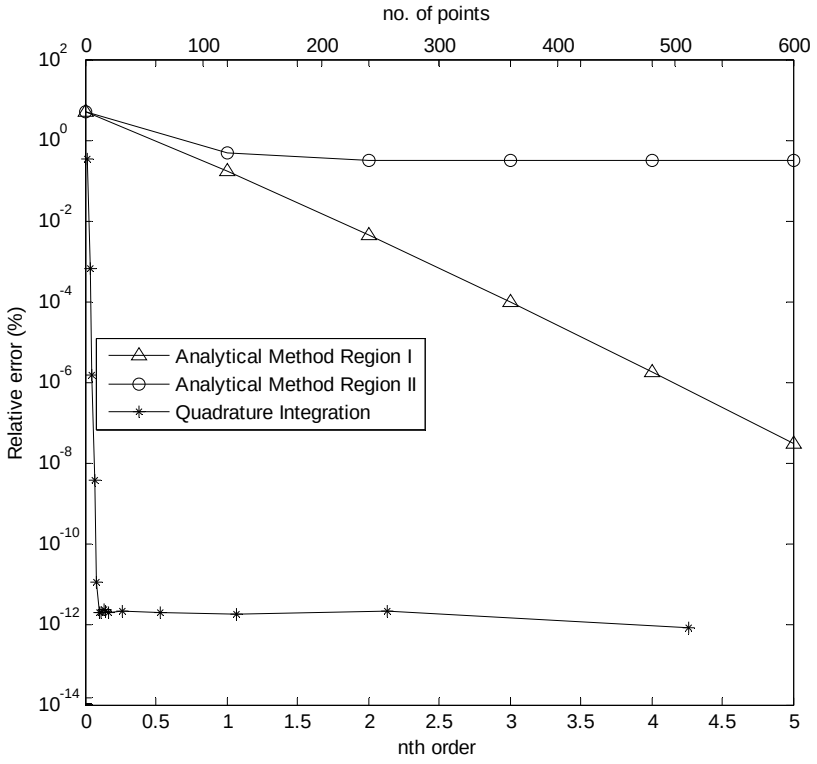

Fig. 3.20 Relative error of impedance of $I_{2D\Pi}$ versus n-th order of AMI and no. of QI points with $(u_o,v_o,w_o)=(0,0,0.1\lambda)$, $\Delta u=0.1\lambda$ and $\Delta v=0.1\lambda$

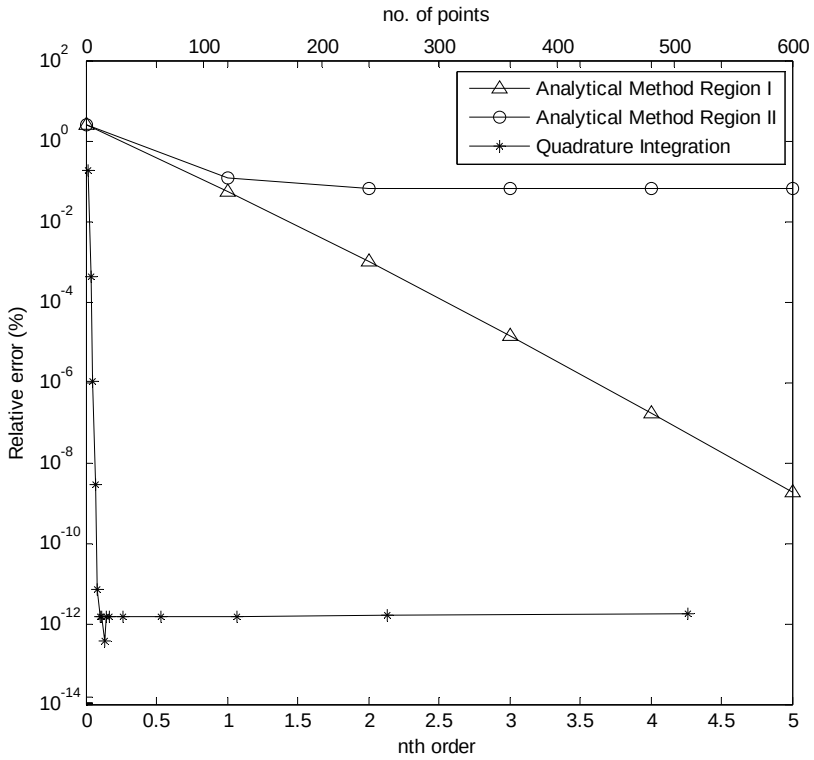

Fig. 3.21 Relative error of impedance of $I_{2D\Pi}$ versus n-th order of AMI and no. of QI points with $(u_o,v_o,w_o)=(0,0,0.1\lambda)$, $\Delta u=0.01\lambda$ and $\Delta v=0.1\lambda$

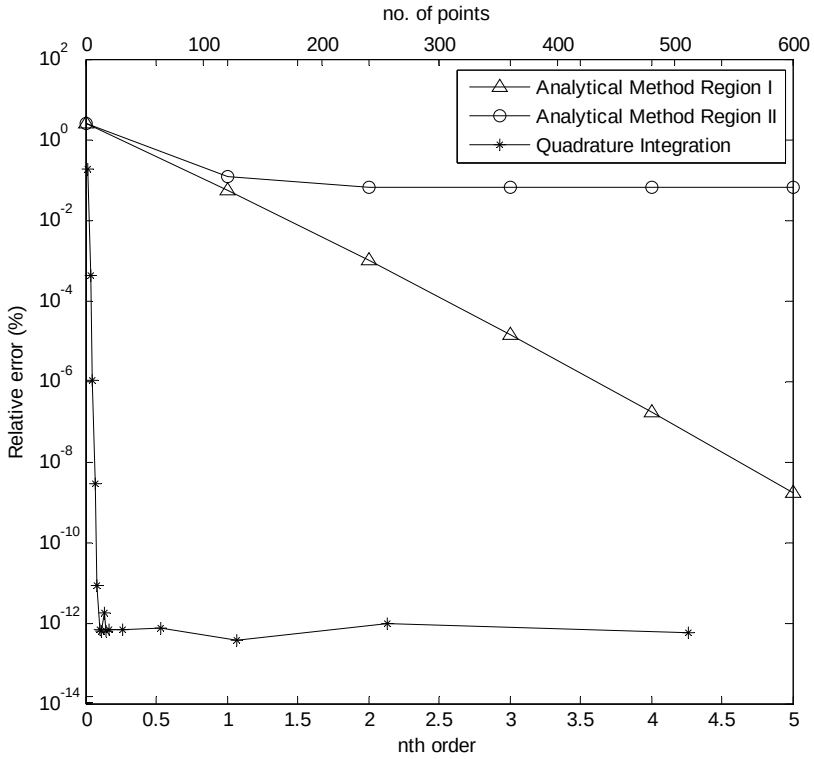

Fig. 3.22 Relative error of impedance of $I_{2D\Pi}$ versus n-th order of AMI and no. of QI points with $(u_o,v_o,w_o)=(0,0,0.1\lambda)$, $\Delta u=0.001\lambda$ and $\Delta v=0.1\lambda$

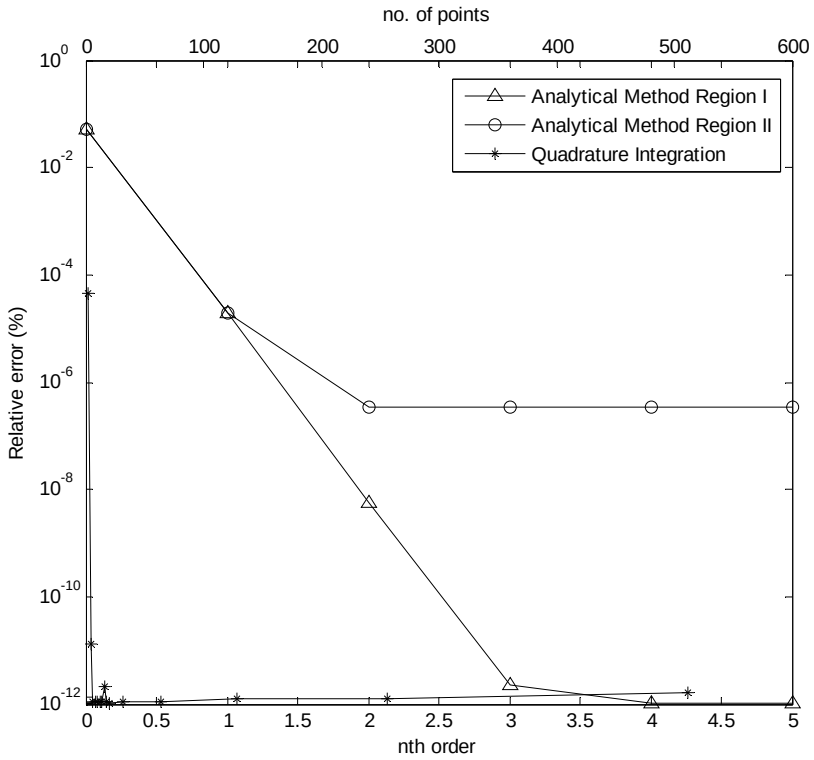

Fig. 3.23 Relative error of impedance of $I_{2D\Pi}$ versus n-th order of AMI and no. of QI points with $(u_o,v_o,w_o)=(0,0,0.1\lambda)$, $\Delta u=0.01\lambda$ and $\Delta v=0.01\lambda$

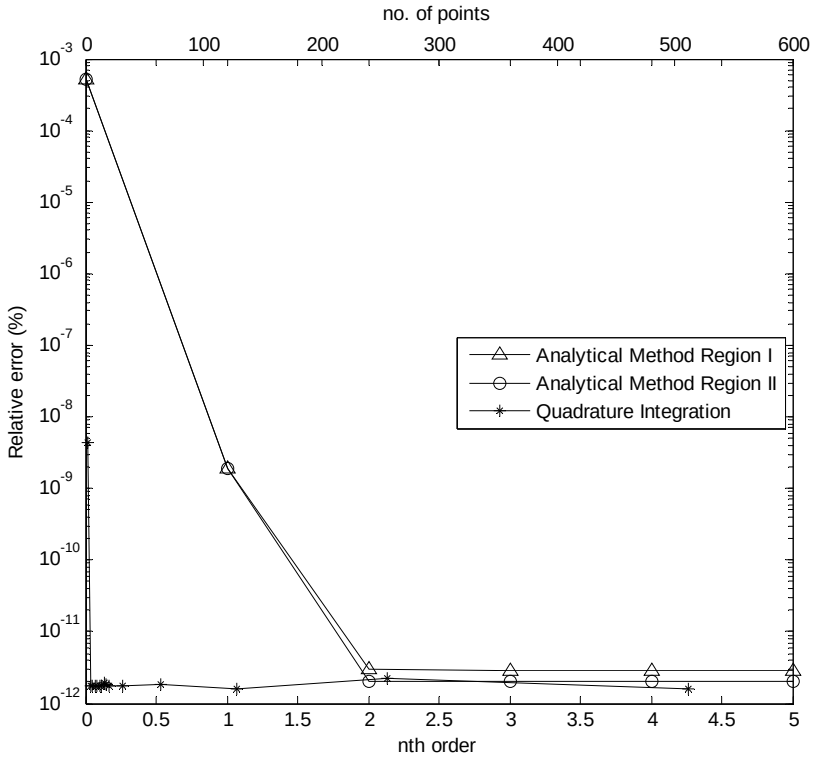

Fig. 3.24 Relative error of impedance of $I_{2D\Pi}$ versus n-th order of AMI and no. of QI points with $(u_o,v_o,w_o)=(0,0,0.1\lambda)$, $\Delta u=0.001\lambda$ and $\Delta v=0.001\lambda$

To investigate the accuracy of the integrals when the source cell is two cells away from the field cell, Fig. 3.25 to Fig. 3.29 show the behaviours of the integrals when $(u_o,v_o,w_o)= (0,2\Delta v,0)$, where Δv is the longer side of the cell. It can be observed that all three schemes, AMI, AMII and QI work quite well. By comparing the relative error of AMII under the conditions $R_o=\max(\Delta u,\Delta v)$ and $R_o=2\times\max(\Delta u,\Delta v)$, the relative error of AMII with $R_o=2\times\max(\Delta u,\Delta v)$ is 100 times less than AMII with $R_o=\max(\Delta u,\Delta v)$. The relative error of AMII with $R_o=2\times\max(\Delta u,\Delta v)$ is less than 0.01%, which is acceptable for most applications.

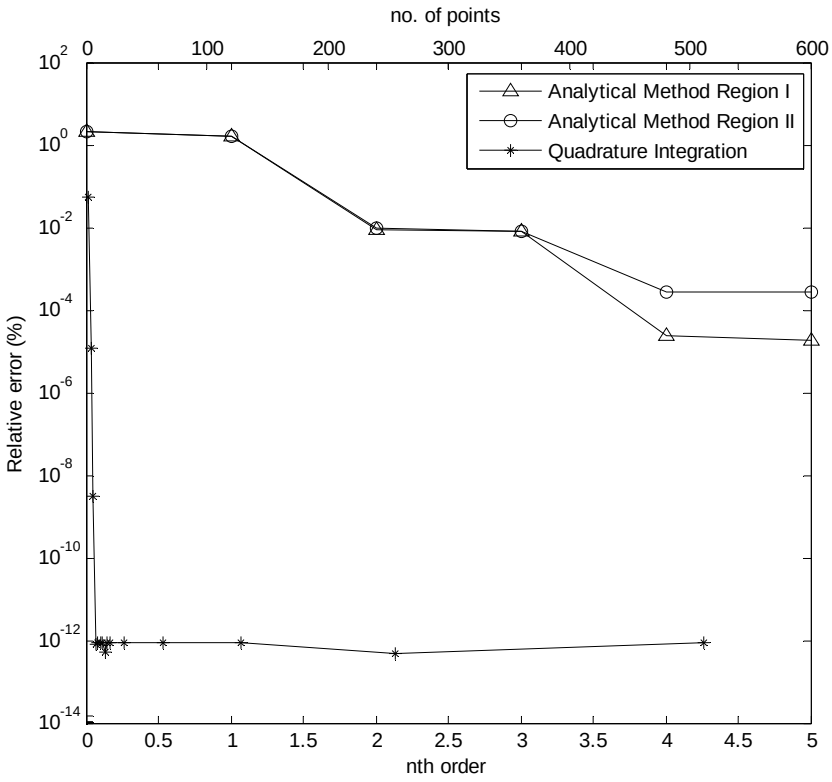

Fig. 3.25 Relative error of impedance of $I_{2D\Pi}$ versus n-th order of AMI and no. of QI points with $(u_o,v_o,w_o)=(0,0.2\lambda,0)$, $\Delta u=0.1\lambda$ and $\Delta v=0.1\lambda$

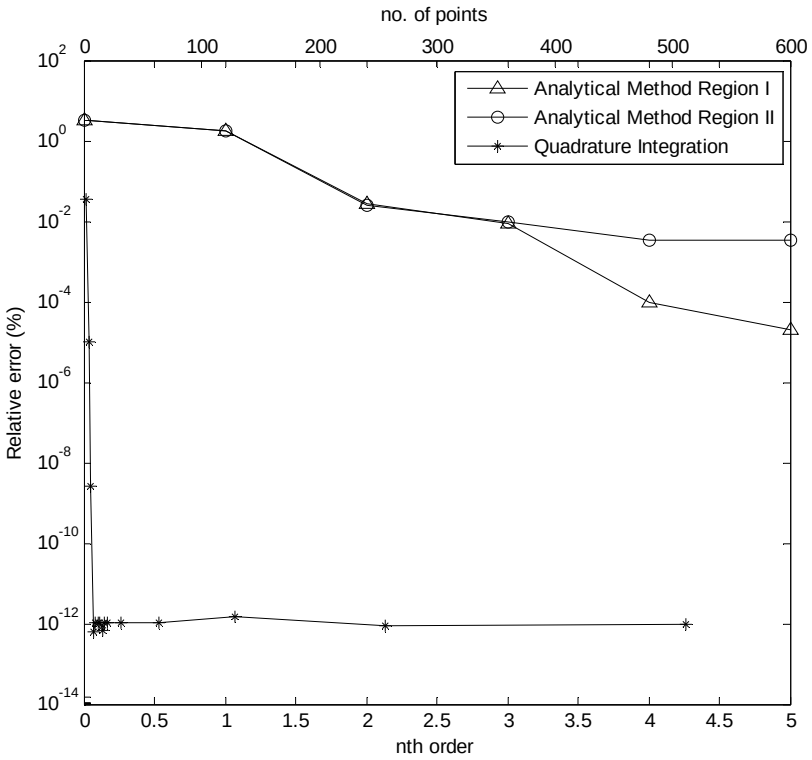

Fig. 3.26 Relative error of impedance of $I_{2D\Pi}$ versus n-th order of AMI and no. of QI points with $(u_o,v_o,w_o)=(0,0.2\lambda,0)$, $\Delta u=0.01\lambda$ and $\Delta v=0.1\lambda$

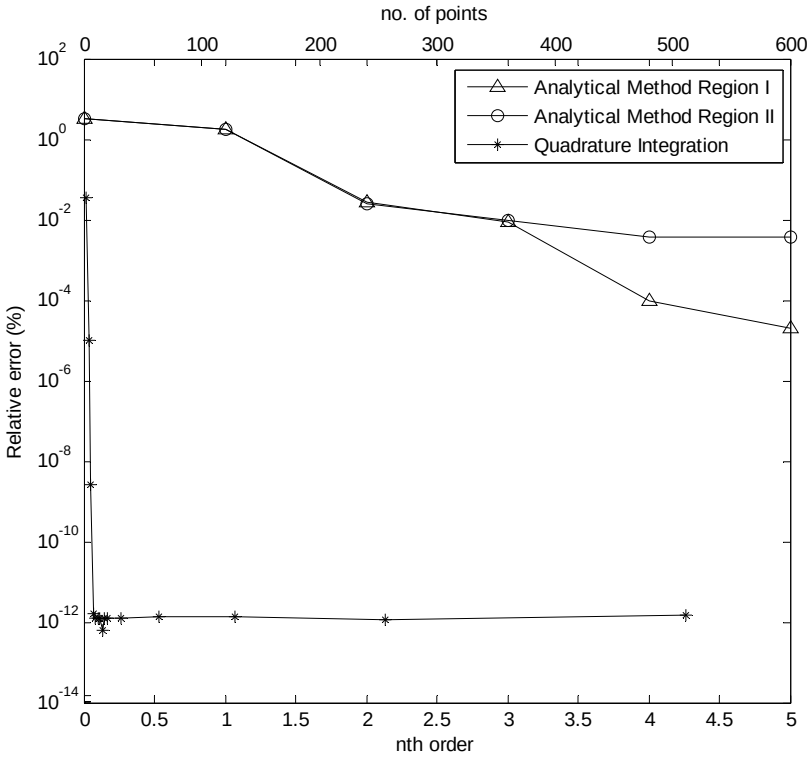

Fig. 3.27 Relative error of impedance of $I_{2D\Pi}$ versus n-th order of AMI and no. of QI points with $(u_o,v_o,w_o)=(0,0.2\lambda,0)$, $\Delta u=0.001\lambda$ and $\Delta v=0.1\lambda$

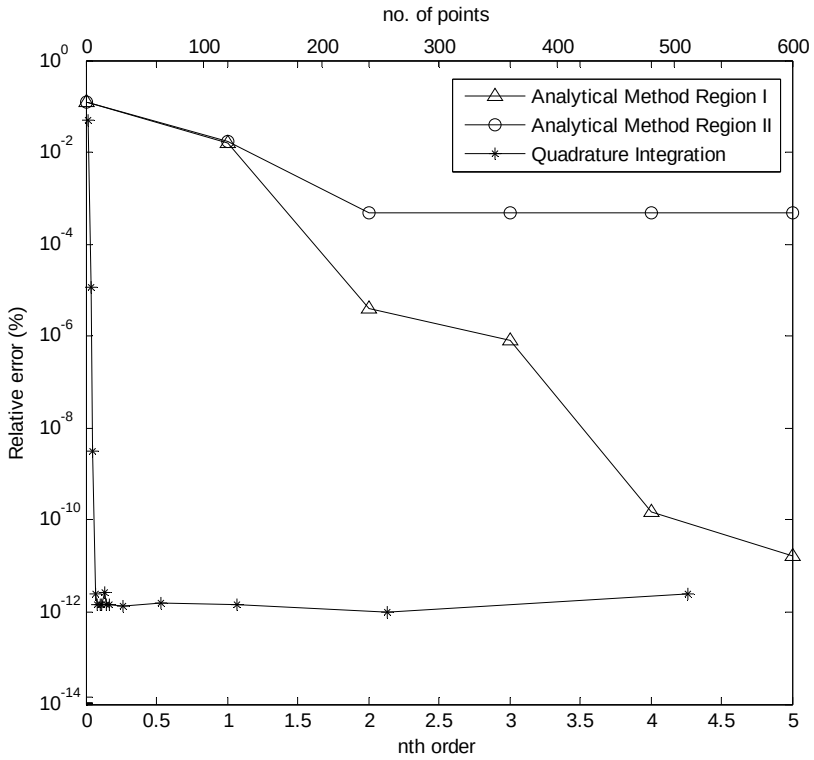

Fig. 3.28 Relative error of impedance of $I_{2D\Pi}$ versus n-th order of AMI and no. of QI points with $(u_o,v_o,w_o)=(0,0.02\lambda,0)$, $\Delta u=0.01\lambda$ and $\Delta v=0.01\lambda$

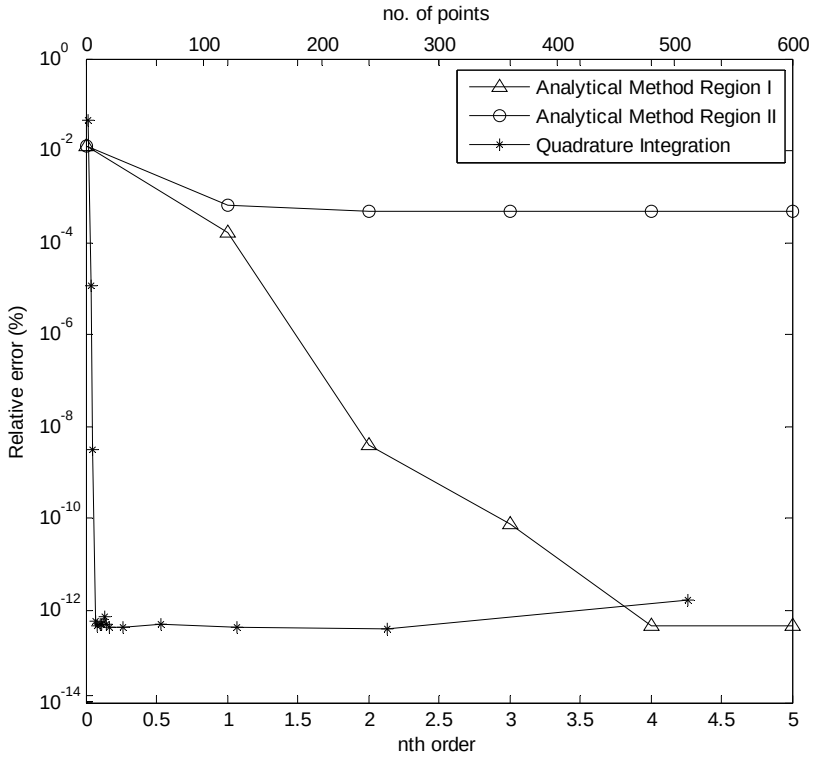

Fig. 3.29 Relative error of impedance of $I_{2D\Pi}$ versus n-th order of AMI and no. of QI points with $(u_o,v_o,w_o)=(0,0.002\lambda,0)$, $\Delta u=0.001\lambda$ and $\Delta v=0.001\lambda$

The detailed analysis of $I_{2D\Pi}$ has been carried out for various combinations of (u_o,v_o,w_o), Δu and Δv. In general, the behaviours of $I_{2D\Lambda}$, $I_{3D\Pi}$ and $I_{3D\Lambda}$ are quite similar to $I_{2D\Pi}$. Instead of plotting all the graphs, the relative errors of $I_{2D\Lambda}$, $I_{3D\Pi}$ and $I_{3D\Lambda}$ are evaluated and summarized into the following tables (see Table 3.5 to Table 3.19), except when $(u_o,v_o,w_o)=(0,0,0)$.

To study the accuracy of $I_{2D\Lambda}$, $I_{3D\Pi}$ and $I_{3D\Lambda}$ when the singular point resides in the region of integration $(u_o,v_o,w_o)=(0,0,0)$, Fig. 3.30 to Fig. 3.35 are plotted with different combinations of Δu_i, Δu and Δv. Fig. 3.30 shows the behaviours of the integrals when $\Delta v=0.1\lambda$ with $\Delta u_i=\Delta u$ as variable. Similar observations as in Fig. 3.11 is also found in Fig. 3.30; when the ratio of $\Delta u/\Delta v$ decreases, the absolute relative error also increases for both AMI_5 and QI_{512}. In this case, the absolute relative error of AMI_5 and QI_{512} are also almost similar and their relative errors are of different polarities. Although the real part of the impedance is not plotted, larger N of QI_N, also tends to converge towards AMI_5. This shows that the QI scheme is much less accurate than AMI when $\Delta u/\Delta v$ becomes very small. Similar observations as in Fig. 3.12 is also found in Fig. 3.31; when the ratio $\Delta u/\Delta v$ becomes unity, the absolute relative errors of QI are quite similar and for AMI, larger Δu tends to converge faster than smaller Δu.

Both Fig. 3.32 and Fig. 3.34 exhibit similar trends, when the ratio $\Delta u/\Delta v$ increases, the absolute relative error decreases for QI_N. However, the absolute relative error of AMI_n increases as $\Delta u/\Delta v$ increases till $n=3$. For $n=4$ and 5, the relative error increases as $\Delta u/\Delta v$ decreases. These increases in relative error may be cause by the increasing inaccuracy of the reference QI_{1024} when $\Delta u/\Delta v$ is very small. Similar observations as

Fig. 3.31 can also be found in both Fig. 3.33 and Fig. 3.35. Finally, it can be deduced from the analyses that AMI has much better accuracy than QI when singular point resides in the region of integration.

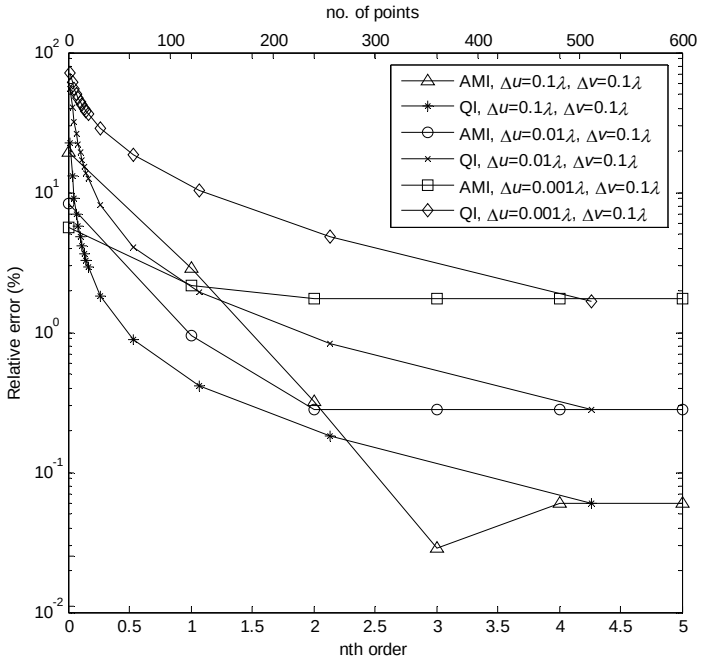

Fig. 3.30 Relative error of impedance of $I_{2D\Lambda}$ versus n-th order of AMI and no. of QI points with $(u_o,v_o,w_o)=(0,0,0)$, $\Delta u_i=\Delta u=0.1\lambda$, 0.01λ and 0.001λ, and $\Delta v=0.1\lambda$

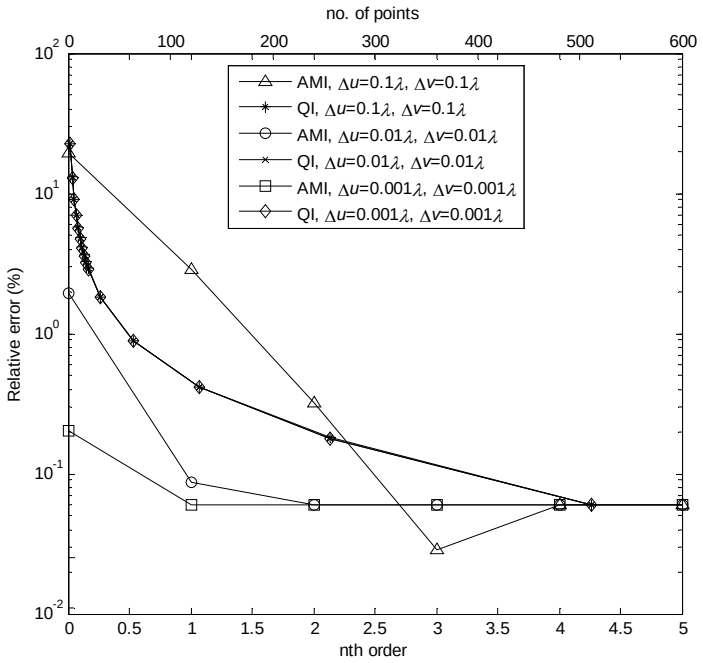

Fig. 3.31 Relative error of impedance of $I_{2D\Lambda}$ versus n-th order of AMI and no. of QI points with $(u_o,v_o,w_o)=(0,0,0)$, $\Delta u_i=\Delta u=\Delta v$, $\Delta u=0.1\lambda$, $\Delta u=0.01\lambda$ and $\Delta u=0.001\lambda$

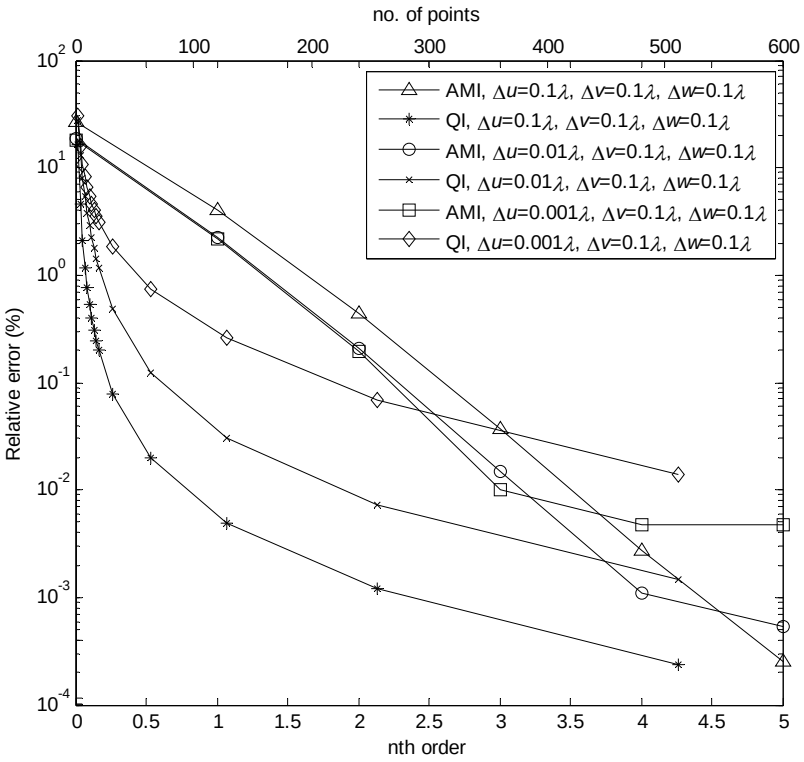

Fig. 3.32 Relative error of impedance of $I_{3D\Pi}$ versus n-th order of AMI and no. of QI points with $(u_o,v_o,w_o)=(0,0,0)$, $\Delta u=0.1\lambda$, 0.01λ and 0.001λ, and $\Delta v=\Delta w=0.1\lambda$

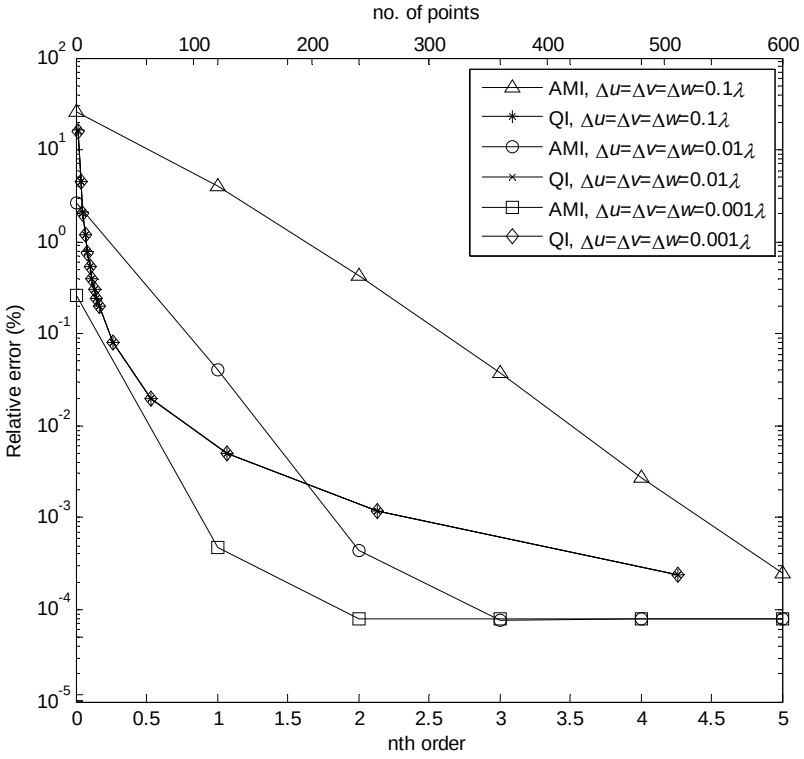

Fig. 3.33 Relative error of impedance of $I_{3D\Pi}$ versus n-th order of AMI and no. of QI points with $(u_o,v_o,w_o)=(0,0,0)$, $\Delta u=\Delta v=\Delta w$, $\Delta u=0.1\lambda$, $\Delta u=0.01\lambda$ and $\Delta u=0.001\lambda$

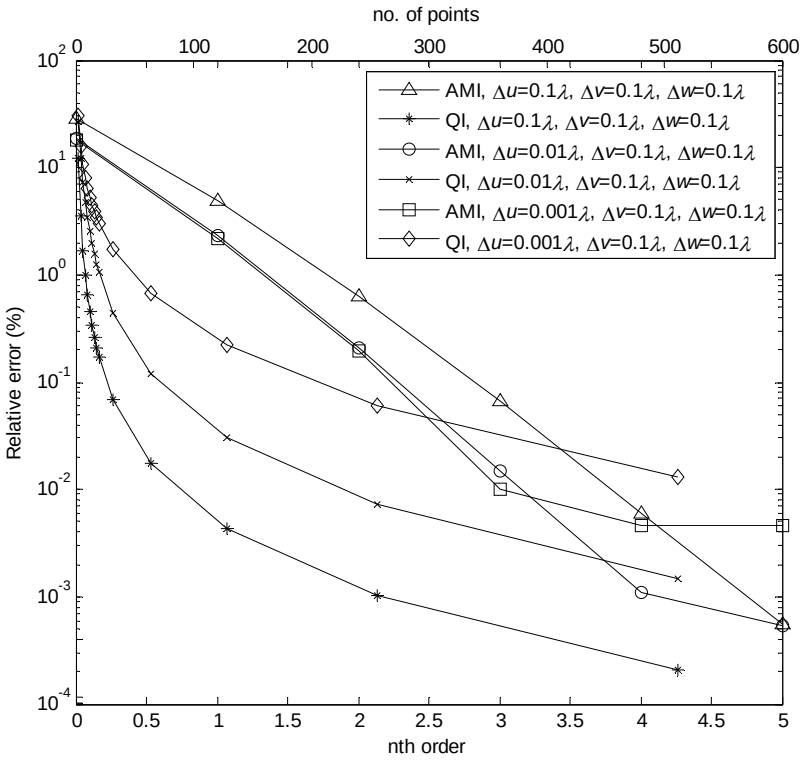

Fig. 3.34 Relative error of impedance of $I_{3D\Lambda}$ versus n-th order of AMI and no. of QI points with $(u_o,v_o,w_o)=(0,0,0)$, $\Delta u_i=\Delta u=0.1\lambda$, 0.01λ and 0.001λ, and $\Delta v=\Delta w=0.1\lambda$

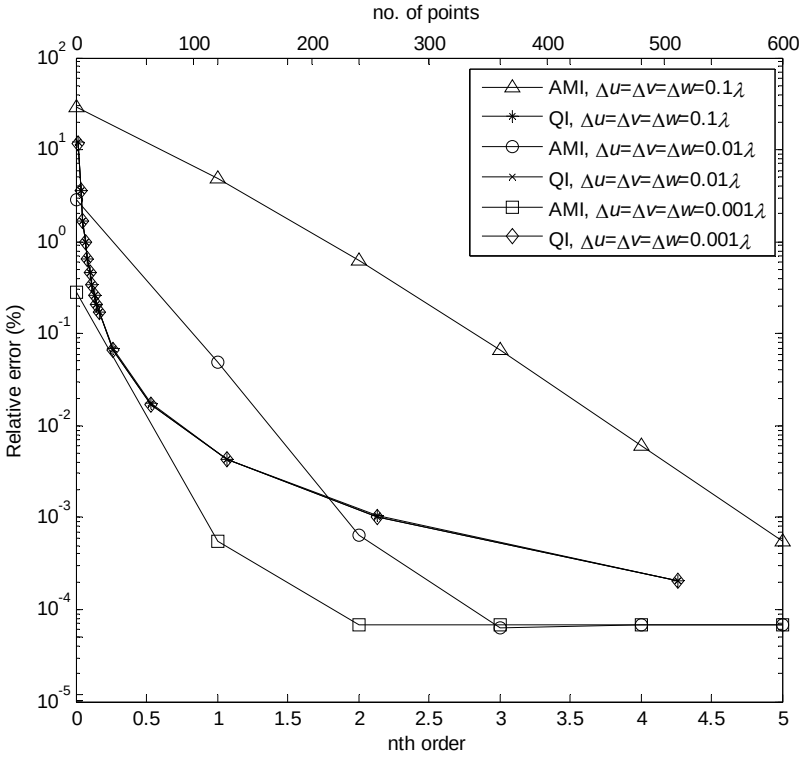

Fig. 3.35 Relative error of impedance of $I_{3D\Lambda}$ versus n-th order of AMI and no. of QI points with $(u_o,v_o,w_o)=(0,0,0)$, $\Delta u_i=\Delta u=\Delta v=\Delta w$, $\Delta u=0.1\lambda$, $\Delta u=0.01\lambda$ and $\Delta u=0.001\lambda$

The behaviours of the second to sixth sets of combinations of the different variables for $I_{2D\Lambda}$, $I_{3D\Pi}$ and $I_{3D\Lambda}$ are pretty much similar to those of $I_{2D\Pi}$. Hence, they will not be discussed further. However, to provide an overall picture on the accuracy of $I_{2D\Lambda}$, $I_{3D\Pi}$ and $I_{3D\Lambda}$, Table 3.5 to Table 3.19 are provided to show the comparison of the absolute relative errors of the second to sixth sets of combinations of the different variables.

Table 3.5 Comparison of the absolute relative errors of $I_{2D\Lambda}$ using AMI, AMII and QI scheme with $(u_o,v_o,w_o)=(\Delta u,0,0)$, $\Delta u_i=\Delta u$ and various combinations of Δu and Δv

Δu	0.1λ	0.01λ	0.001λ	0.01λ	0.001λ
Δv	0.1λ	0.1λ	0.1λ	0.01λ	0.001λ
Δu_i	0.1λ	0.01λ	0.001λ	0.01λ	0.001λ
AMI_0	5.296	7.837	6.335	0.437	0.044
AMI_1	3.025	0.588	0.508	0.030	2.97E-04
AMI_2	0.145	0.035	0.035	1.37E-04	1.38E-07
AMI_3	0.038	1.73E-03	1.11E-03	3.68E-06	8.46E-09
AMI_4	1.70E-03	7.32E-05	9.25E-04	1.92E-08	8.83E-09
AMI_5	2.60E-04	4.51E-06	9.19E-04	9.07E-09	8.83E-09
$AMII_0$	5.016	1095	8.64E+07	0.647	0.509
$AMII_1$	2.543	1097	8.64E+07	0.479	0.507
$AMII_2$	0.640	1097	8.64E+07	0.508	0.508
$AMII_3$	0.525	1097	8.64E+07	0.508	0.508
$AMII_4$	0.500	1097	8.64E+07	0.508	0.508
$AMII_5$	0.502	1097	8.64E+07	0.508	0.508
QI_2	0.290	28.380	61.941	0.252	0.251
QI_4	0.121	11.681	48.847	0.117	0.117
QI_6	0.039	5.498	40.778	0.038	0.038
QI_8	0.017	2.871	34.976	0.016	0.016
QI_{10}	8.61E-03	1.635	30.484	8.36E-03	8.36E-03
QI_{12}	5.06E-03	1.001	26.855	4.91E-03	4.91E-03
QI_{14}	3.23E-03	0.650	23.839	3.14E-03	3.14E-03
QI_{16}	2.19E-03	0.444	21.284	2.12E-03	2.12E-03
QI_{18}	1.55E-03	0.316	19.089	1.51E-03	1.50E-03
QI_{20}	1.14E-03	0.232	17.185	1.11E-03	1.10E-03
QI_{32}	2.84E-04	0.058	9.650	2.76E-04	2.76E-04
QI_{64}	3.63E-05	7.43E-03	2.710	3.53E-05	3.53E-05
QI_{128}	4.58E-06	9.38E-04	0.450	4.45E-06	4.45E-06
QI_{256}	5.68E-07	1.16E-04	0.057	5.52E-07	5.52E-07
QI_{512}	6.34E-08	1.30E-05	6.39E-03	6.15E-08	6.15E-08

Table 3.6 Comparison of the absolute relative errors of $I_{2D\Lambda}$ using AMI, AMII and QI scheme with $(u_o,v_o,w_o)=(0,\Delta v,0)$, $\Delta u_i=\Delta u$ and various combinations of Δu and Δv

Δu	0.1λ	0.01λ	0.001λ	0.01λ	0.001λ
Δv	0.1λ	0.1λ	0.1λ	0.01λ	0.001λ
Δu_i	0.1λ	0.01λ	0.001λ	0.01λ	0.001λ
AMI_0	1.629	5.874	5.949	0.016	2.06E-04
AMI_1	1.629	1.785	1.792	0.016	1.61E-04
AMI_2	0.024	0.058	0.059	2.25E-05	2.25E-08
AMI_3	8.93E-03	9.08E-03	9.16E-03	8.81E-07	9.40E-11
AMI_4	1.89E-04	2.03E-04	2.10E-04	1.85E-09	5.90E-12
AMI_5	2.59E-05	2.17E-05	2.19E-05	5.49E-11	5.90E-12
$AMII_0$	1.185	5.807	5.877	0.421	0.437
$AMII_1$	1.222	1.550	1.538	0.422	0.437
$AMII_2$	0.482	0.219	0.239	0.437	0.437
$AMII_3$	0.460	0.243	0.263	0.437	0.437
$AMII_4$	0.454	0.236	0.257	0.437	0.437
$AMII_5$	0.454	0.236	0.257	0.437	0.437
QI_2	0.504	0.702	0.712	0.483	0.482
QI_4	4.16E-04	3.70E-03	3.88E-03	3.94E-04	3.94E-04
QI_6	2.87E-06	1.85E-05	2.04E-05	2.78E-06	2.78E-06
QI_8	1.07E-07	9.04E-08	1.06E-07	1.05E-07	1.05E-07
QI_{10}	1.43E-09	4.56E-10	5.46E-10	1.51E-09	1.47E-09
QI_{12}	6.19E-11	3.84E-11	1.71E-11	5.19E-11	1.64E-11
QI_{14}	8.17E-11	3.72E-11	1.76E-11	2.98E-11	5.68E-12
QI_{16}	8.30E-11	3.88E-11	1.82E-11	2.77E-11	7.84E-12
QI_{18}	8.20E-11	3.72E-11	1.76E-11	2.95E-11	5.97E-12
QI_{20}	8.21E-11	3.71E-11	1.77E-11	2.95E-11	5.93E-12
QI_{32}	8.19E-11	3.72E-11	1.76E-11	2.99E-11	6.11E-12
QI_{64}	8.21E-11	3.72E-11	1.77E-11	2.94E-11	5.84E-12
QI_{128}	8.40E-11	3.85E-11	1.87E-11	2.82E-11	7.62E-12
QI_{256}	8.67E-11	3.65E-11	2.20E-11	2.52E-11	9.76E-12
QI_{512}	6.38E-11	4.23E-11	4.34E-11	6.52E-11	3.02E-11

Table 3.7 Comparison of the absolute relative errors of $I_{2D\Lambda}$ using AMI, AMII and QI scheme with $(u_o,v_o,w_o)=(0,0,0.1\lambda)$, $\Delta u_i=\Delta u$ and various combinations of Δu and Δv

Δu	0.1λ	0.01λ	0.001λ	0.01λ	0.001λ
Δv	0.1λ	0.1λ	0.1λ	0.01λ	0.001λ
Δu_i	0.1λ	0.01λ	0.001λ	0.01λ	0.001λ
AMI_0	6.760	2.504	2.454	0.078	7.85E-04
AMI_1	0.378	0.056	0.054	5.25E-05	4.72E-09
AMI_2	0.018	9.86E-04	9.59E-04	3.12E-08	6.85E-09
AMI_3	7.91E-04	1.43E-05	1.38E-05	2.44E-11	6.54E-09
AMI_4	3.02E-05	1.74E-07	1.66E-07	3.81E-11	6.63E-09

AMI_5	1.03E-06	1.84E-09	1.30E-09	3.81E-11	6.64E-09
$AMII_0$	6.968	2.506	2.456	0.078	7.85E-04
$AMII_1$	1.921	0.126	0.123	5.44E-05	5.32E-09
$AMII_2$	1.417	0.067	0.065	1.97E-06	3.97E-11
$AMII_3$	1.417	0.067	0.065	1.97E-06	3.97E-11
$AMII_4$	1.417	0.067	0.065	1.97E-06	3.97E-11
$AMII_5$	1.417	0.067	0.065	1.97E-06	3.97E-11
QI_2	0.298	0.185	0.186	6.63E-05	6.68E-09
QI_4	2.85E-04	4.17E-04	4.20E-04	3.42E-11	3.85E-11
QI_6	5.48E-07	1.07E-06	1.08E-06	3.64E-11	3.85E-11
QI_8	1.65E-09	2.89E-09	2.85E-09	3.65E-11	3.85E-11
QI_{10}	2.25E-11	9.54E-12	8.03E-11	3.64E-11	3.85E-11
QI_{12}	2.66E-11	1.43E-11	8.83E-11	3.64E-11	3.85E-11
QI_{14}	2.66E-11	1.42E-11	8.83E-11	3.64E-11	3.85E-11
QI_{16}	2.53E-11	1.40E-11	8.68E-11	3.51E-11	3.69E-11
QI_{18}	2.66E-11	1.44E-11	8.82E-11	3.65E-11	3.86E-11
QI_{20}	2.66E-11	1.43E-11	8.83E-11	3.65E-11	3.85E-11
QI_{32}	2.69E-11	1.42E-11	8.82E-11	3.64E-11	3.83E-11
QI_{64}	2.63E-11	1.43E-11	8.80E-11	3.67E-11	3.87E-11
QI_{128}	2.55E-11	1.04E-11	8.66E-11	3.75E-11	3.91E-11
QI_{256}	3.43E-11	1.71E-11	9.16E-11	3.72E-11	3.45E-11
QI_{512}	1.92E-11	9.75E-12	8.38E-11	5.57E-11	6.01E-11

Table 3.8 Comparison of the absolute relative errors of $I_{2D\Lambda}$ using AMI, AMII and QI scheme with $(u_o,v_o,w_o)=(0,2\Delta v,0)$, $\Delta u_i=\Delta u$ and various combinations of Δu and Δv

Δu	0.1λ	0.01λ	0.001λ	0.01λ	0.001λ
Δv	0.1λ	0.1λ	0.1λ	0.01λ	0.001λ
Δu_i	0.1λ	0.01λ	0.001λ	0.01λ	0.001λ
AMI_0	1.643	3.145	3.170	0.016	2.65E-04
AMI_1	1.643	1.691	1.693	0.016	1.62E-04
AMI_2	0.018	0.028	0.028	1.53E-05	1.53E-08
AMI_3	8.43E-03	8.42E-03	8.44E-03	8.31E-07	4.54E-11
AMI_4	1.15E-04	9.47E-05	9.71E-05	1.12E-09	3.78E-11
AMI_5	2.15E-05	1.99E-05	1.99E-05	1.05E-11	3.78E-11
$AMII_0$	1.633	3.143	3.168	7.18E-03	9.21E-03
$AMII_1$	1.633	1.688	1.689	6.98E-03	9.21E-03
$AMII_2$	0.030	0.024	0.024	9.38E-03	9.37E-03
$AMII_3$	0.015	0.010	0.010	9.38E-03	9.37E-03
$AMII_4$	0.010	0.003	0.004	9.38E-03	9.37E-03
$AMII_5$	0.010	0.003	0.004	9.38E-03	9.37E-03
QI_2	0.060	0.036	0.037	0.052	0.052
QI_4	8.57E-06	1.01E-05	1.02E-05	8.10E-06	8.10E-06
QI_6	7.73E-10	2.62E-09	2.69E-09	8.14E-10	7.49E-10
QI_8	6.59E-11	5.17E-11	1.93E-12	2.93E-11	3.78E-11
QI_{10}	6.59E-11	5.19E-11	2.64E-12	2.95E-11	3.79E-11
QI_{12}	6.59E-11	5.19E-11	2.65E-12	2.94E-11	3.77E-11

QI_{14}	6.60E-11	5.19E-11	2.68E-12	2.93E-11	3.78E-11
QI_{16}	6.42E-11	5.34E-11	2.91E-12	3.10E-11	3.62E-11
QI_{18}	6.58E-11	5.19E-11	2.64E-12	2.93E-11	3.79E-11
QI_{20}	6.60E-11	5.17E-11	2.68E-12	2.93E-11	3.79E-11
QI_{32}	6.58E-11	5.20E-11	2.59E-12	2.95E-11	3.80E-11
QI_{64}	6.61E-11	5.24E-11	2.43E-12	2.90E-11	3.76E-11
QI_{128}	6.67E-11	5.12E-11	1.96E-12	2.88E-11	3.72E-11
QI_{256}	6.09E-11	4.65E-11	7.70E-12	2.86E-11	3.72E-11
QI_{512}	7.83E-11	3.73E-11	4.60E-12	3.96E-11	5.73E-11

Table 3.9 Comparison of the absolute relative errors of $I_{2D\Lambda}$ using AMI, AMII and QI scheme with $(u_o,v_o,w_o)=(\Delta u,\Delta v,1\lambda)$, $\Delta u_i=\Delta u$ and various combinations of Δu and Δv

Δu	0.1λ	0.01λ	0.001λ	0.01λ	0.001λ
Δv	0.1λ	0.1λ	0.1λ	0.01λ	0.001λ
Δu_i	0.1λ	0.01λ	0.001λ	0.01λ	0.001λ
AMI_0	1.788	0.269	0.253	0.018	1.83E-04
AMI_1	0.068	0.017	0.017	7.07E-06	1.53E-05
AMI_2	1.22E-03	7.86E-05	1.73E-04	5.30E-07	5.84E-05
AMI_3	2.43E-05	1.01E-06	3.97E-04	1.52E-06	1.66E-04
AMI_4	3.74E-07	6.59E-08	9.17E-04	3.48E-06	3.78E-04
AMI_5	8.92E-09	1.80E-07	1.77E-03	6.65E-06	7.19E-04
$AMII_0$	1.788	0.269	0.253	0.018	1.83E-04
$AMII_1$	0.068	0.017	0.017	7.05E-06	7.41E-10
$AMII_2$	1.21E-03	7.83E-05	7.57E-05	1.28E-09	3.53E-11
$AMII_3$	4.60E-05	1.89E-06	1.85E-06	3.35E-11	3.53E-11
$AMII_4$	2.89E-05	1.13E-06	1.10E-06	3.82E-11	3.87E-11
$AMII_5$	2.89E-05	1.13E-06	1.10E-06	3.86E-11	4.21E-11
QI_2	2.98E-03	2.67E-04	2.67E-04	3.14E-07	6.50E-11
QI_4	1.77E-09	8.25E-11	1.45E-10	5.51E-11	3.55E-11
QI_6	1.70E-11	9.11E-12	9.55E-11	5.51E-11	3.55E-11
QI_8	1.69E-11	9.13E-12	9.55E-11	5.51E-11	3.55E-11
QI_{10}	1.70E-11	9.17E-12	9.55E-11	5.51E-11	3.55E-11
QI_{12}	1.70E-11	9.15E-12	9.55E-11	5.51E-11	3.54E-11
QI_{14}	1.69E-11	9.10E-12	9.55E-11	5.51E-11	3.56E-11
QI_{16}	1.52E-11	1.08E-11	9.37E-11	5.33E-11	3.38E-11
QI_{18}	1.70E-11	9.08E-12	9.55E-11	5.52E-11	3.53E-11
QI_{20}	1.70E-11	9.24E-12	9.55E-11	5.51E-11	3.55E-11
QI_{32}	1.71E-11	9.24E-12	9.52E-11	5.52E-11	3.55E-11
QI_{64}	1.71E-11	9.53E-12	9.58E-11	5.47E-11	3.54E-11
QI_{128}	1.78E-11	7.17E-12	9.74E-11	5.61E-11	3.46E-11
QI_{256}	1.73E-11	6.63E-12	1.03E-10	5.29E-11	3.01E-11
QI_{512}	1.89E-11	2.40E-11	1.02E-10	6.20E-11	3.66E-11

Table 3.10 Comparison of the absolute relative errors of $I_{3D\Pi}$ using AMI, AMII and QI scheme with $(u_o,v_o,w_o)=(\Delta u,0,0)$ and various combinations of Δu, Δv and Δw

Δu	0.1λ	0.01λ	0.001λ	0.01λ	0.001λ
Δv	0.1λ	0.1λ	0.1λ	0.01λ	0.001λ
Δw	0.1λ	0.1λ	0.1λ	0.01λ	0.001λ
AMI_0	1.648	14.980	17.545	0.080	7.90E-03
AMI_1	1.459	1.531	2.076	0.014	1.45E-04
AMI_2	0.036	0.119	0.186	3.45E-05	3.45E-08
AMI_3	7.29E-03	7.50E-03	0.014	7.21E-07	1.91E-11
AMI_4	2.08E-04	4.01E-04	8.32E-04	2.04E-09	5.29E-11
AMI_5	1.91E-05	1.87E-05	4.43E-05	4.49E-11	5.29E-11
$AMII_0$	1.454	4.55E+04	4.23E+09	0.220	0.220
$AMII_1$	1.248	4.56E+04	4.23E+09	0.206	0.220
$AMII_2$	0.267	4.56E+04	4.23E+09	0.220	0.220
$AMII_3$	0.245	4.56E+04	4.23E+09	0.220	0.220
$AMII_4$	0.238	4.56E+04	4.23E+09	0.220	0.220
$AMII_5$	0.238	4.56E+04	4.23E+09	0.220	0.220
QI_2	0.857	19.950	29.602	0.818	0.817
QI_4	6.59E-03	6.043	15.036	6.41E-03	6.40E-03
QI_6	9.23E-05	2.328	9.756	9.03E-05	9.03E-05
QI_8	1.56E-06	1.012	7.045	1.52E-06	1.52E-06
QI_{10}	2.94E-08	0.475	5.397	2.89E-08	2.88E-08
QI_{12}	5.79E-10	0.235	4.294	6.58E-10	5.41E-10
QI_{14}	2.84E-11	0.121	3.506	7.91E-11	3.74E-11
QI_{16}	3.36E-11	0.065	2.918	6.86E-11	4.85E-11
QI_{18}	3.54E-11	0.035	2.464	6.66E-11	5.03E-11
QI_{20}	3.56E-11	0.020	2.105	6.66E-11	5.04E-11
QI_{32}	3.54E-11	7.52E-04	0.950	6.68E-11	5.04E-11
QI_{64}	3.53E-11	3.30E-07	0.193	6.54E-11	4.85E-11
QI_{128}	3.43E-11	8.50E-12	0.017	6.82E-11	4.98E-11
QI_{256}	3.62E-11	7.15E-12	3.85E-04	6.98E-11	5.13E-11
QI_{512}	3.20E-11	5.42E-12	6.10E-07	8.90E-11	2.93E-11

Table 3.11 Comparison of the absolute relative errors of $I_{3D\Pi}$ using AMI, AMII and QI scheme with $(u_o,v_o,w_o)=(0,\Delta v,0)$ and various combinations of Δu, Δv and Δw

Δu	0.1λ	0.01λ	0.001λ	0.01λ	0.001λ
Δv	0.1λ	0.1λ	0.1λ	0.01λ	0.001λ
Δw	0.1λ	0.1λ	0.1λ	0.01λ	0.001λ
AMI_0	1.648	2.778	2.808	0.080	7.90E-03
AMI_1	1.459	1.563	1.566	0.014	1.45E-04
AMI_2	0.036	9.68E-03	0.010	3.45E-05	3.45E-08
AMI_3	7.29E-03	7.49E-03	7.50E-03	7.20E-07	2.30E-11
AMI_4	2.08E-04	3.16E-05	2.96E-05	2.05E-09	4.90E-11

AMI_5	1.91E-05	1.77E-05	1.77E-05	7.42E-11	4.90E-11
$AMII_0$	1.454	2.778	2.807	0.220	0.220
$AMII_1$	1.248	1.563	1.563	0.206	0.220
$AMII_2$	0.267	0.012	0.014	0.220	0.220
$AMII_3$	0.245	0.011	0.013	0.220	0.220
$AMII_4$	0.238	3.43E-03	5.96E-03	0.220	0.220
$AMII_5$	0.238	3.43E-03	5.96E-03	0.220	0.220
QI_2	0.857	0.804	0.809	0.818	0.817
QI_4	6.59E-03	6.39E-03	6.47E-03	6.41E-03	6.40E-03
QI_6	9.23E-05	9.62E-05	9.76E-05	9.03E-05	9.03E-05
QI_8	1.56E-06	1.84E-06	1.87E-06	1.52E-06	1.52E-06
QI_{10}	2.94E-08	3.88E-08	3.97E-08	2.88E-08	2.88E-08
QI_{12}	5.89E-10	8.22E-10	8.90E-10	5.39E-10	5.45E-10
QI_{14}	1.15E-11	6.45E-11	1.75E-11	4.00E-11	3.35E-11
QI_{16}	1.56E-11	7.50E-11	1.34E-11	5.06E-11	4.45E-11
QI_{18}	1.75E-11	7.68E-11	1.35E-11	5.25E-11	4.63E-11
QI_{20}	1.76E-11	7.70E-11	1.34E-11	5.26E-11	4.64E-11
QI_{32}	1.74E-11	7.68E-11	1.34E-11	5.26E-11	4.62E-11
QI_{64}	1.69E-11	7.73E-11	1.25E-11	5.33E-11	4.52E-11
QI_{128}	1.78E-11	7.50E-11	1.32E-11	5.26E-11	4.65E-11
QI_{256}	2.33E-11	7.82E-11	2.24E-11	5.25E-11	4.34E-11
QI_{512}	2.40E-11	6.85E-11	1.14E-11	4.86E-11	4.90E-11

Table 3.12 Comparison of the absolute relative errors of $I_{3D\Pi}$ using AMI, AMII and QI scheme with $(u_o,v_o,w_o)=(0,0,0.1\lambda)$ and various combinations of Δu, Δv and Δw

Δu	0.1λ	0.01λ	0.001λ	0.01λ	0.001λ
Δv	0.1λ	0.1λ	0.1λ	0.01λ	0.001λ
Δw	0.1λ	0.1λ	0.1λ	0.01λ	0.001λ
AMI_0	1.648	2.778	2.808	0.016	1.64E-04
AMI_1	1.459	1.563	1.566	0.016	1.64E-04
AMI_2	0.036	9.68E-03	0.010	3.54E-06	3.96E-10
AMI_3	7.29E-03	7.49E-03	7.50E-03	8.10E-07	7.10E-11
AMI_4	2.08E-04	3.16E-05	2.96E-05	2.46E-10	5.43E-11
AMI_5	1.91E-05	1.77E-05	1.77E-05	1.80E-11	5.43E-11
$AMII_0$	1.454	2.778	2.807	0.016	1.64E-04
$AMII_1$	1.248	1.563	1.563	0.016	1.64E-04
$AMII_2$	0.267	0.012	0.014	3.67E-06	3.85E-10
$AMII_3$	0.245	0.011	0.013	9.50E-07	5.69E-11
$AMII_4$	0.238	3.43E-03	5.96E-03	1.64E-07	5.48E-11
$AMII_5$	0.238	3.43E-03	5.96E-03	1.64E-07	5.48E-11
QI_2	0.857	0.804	0.809	1.00E-04	1.00E-08
QI_4	6.59E-03	6.39E-03	6.47E-03	3.40E-11	5.48E-11
QI_6	9.23E-05	9.62E-05	9.76E-05	3.75E-12	5.48E-11
QI_8	1.56E-06	1.84E-06	1.87E-06	3.72E-12	5.48E-11
QI_{10}	2.94E-08	3.88E-08	3.97E-08	3.72E-12	5.48E-11
QI_{12}	5.87E-10	8.23E-10	8.89E-10	3.70E-12	5.49E-11

QI_{14}	1.11E-11	6.35E-11	1.75E-11	3.83E-12	5.48E-11
QI_{16}	1.66E-11	7.40E-11	1.35E-11	4.58E-12	5.35E-11
QI_{18}	1.85E-11	7.59E-11	1.36E-11	3.79E-12	5.49E-11
QI_{20}	1.87E-11	7.61E-11	1.35E-11	3.67E-12	5.50E-11
QI_{32}	1.84E-11	7.59E-11	1.35E-11	3.58E-12	5.48E-11
QI_{64}	1.81E-11	7.63E-11	1.26E-11	3.46E-12	5.56E-11
QI_{128}	1.83E-11	7.40E-11	1.37E-11	2.89E-12	5.59E-11
QI_{256}	2.44E-11	7.76E-11	2.24E-11	1.01E-12	5.42E-11
QI_{512}	2.59E-11	6.76E-11	1.21E-11	1.26E-12	5.88E-11

Table 3.13 Comparison of the absolute relative errors of $I_{3D\Pi}$ using AMI, AMII and QI scheme with $(u_o,v_o,w_o)=(0,2\Delta v,0)$ and various combinations of Δu, Δv and Δw

Δu	0.1λ	0.01λ	0.001λ	0.01λ	0.001λ
Δv	0.1λ	0.1λ	0.1λ	0.01λ	0.001λ
Δw	0.1λ	0.1λ	0.1λ	0.01λ	0.001λ
AMI_0	1.606	2.072	2.081	0.019	1.12E-03
AMI_1	1.604	1.637	1.638	0.016	1.59E-04
AMI_2	0.019	8.84E-03	8.94E-03	1.75E-05	1.75E-08
AMI_3	7.90E-03	8.01E-03	8.01E-03	7.79E-07	1.82E-11
AMI_4	1.19E-04	2.48E-05	2.41E-05	1.17E-09	5.98E-11
AMI_5	1.91E-05	1.88E-05	1.88E-05	3.08E-11	5.98E-11
$AMII_0$	1.604	2.072	2.081	0.017	2.78E-03
$AMII_1$	1.601	1.638	1.638	0.013	2.55E-03
$AMII_2$	0.023	9.19E-03	9.28E-03	2.72E-03	2.71E-03
$AMII_3$	0.010	8.07E-03	8.07E-03	2.72E-03	2.71E-03
$AMII_4$	3.74E-03	3.12E-04	2.79E-04	2.72E-03	2.71E-03
$AMII_5$	3.74E-03	3.12E-04	2.79E-04	2.72E-03	2.71E-03
QI_2	0.067	0.052	0.052	0.058	0.058
QI_4	1.36E-05	1.19E-05	1.19E-05	1.27E-05	1.27E-05
QI_6	3.80E-09	3.17E-09	3.23E-09	3.55E-09	3.50E-09
QI_8	2.28E-11	1.88E-11	3.88E-11	1.25E-11	5.84E-11
QI_{10}	2.22E-11	1.94E-11	3.81E-11	1.37E-11	5.98E-11
QI_{12}	2.24E-11	1.93E-11	3.81E-11	1.37E-11	5.99E-11
QI_{14}	2.23E-11	1.93E-11	3.82E-11	1.38E-11	5.98E-11
QI_{16}	2.40E-11	1.78E-11	3.97E-11	1.25E-11	5.83E-11
QI_{18}	2.23E-11	1.94E-11	3.81E-11	1.37E-11	5.99E-11
QI_{20}	2.24E-11	1.94E-11	3.80E-11	1.39E-11	5.97E-11
QI_{32}	2.23E-11	1.95E-11	3.80E-11	1.36E-11	6.00E-11
QI_{64}	2.15E-11	1.91E-11	3.82E-11	1.35E-11	6.01E-11
QI_{128}	2.34E-11	1.98E-11	3.71E-11	1.41E-11	5.92E-11
QI_{256}	2.05E-11	2.38E-11	4.08E-11	1.62E-11	5.68E-11
QI_{512}	2.07E-11	2.35E-11	3.82E-11	3.48E-11	5.94E-11

Table 3.14 Comparison of the absolute relative errors of $I_{3D\Pi}$ using AMI, AMII and QI scheme with $(u_o,v_o,w_o)=(\Delta u,\Delta v,1\lambda)$ and various combinations of Δu, Δv and Δw

Δu	0.1λ	0.01λ	0.001λ	0.01λ	0.001λ
Δv	0.1λ	0.1λ	0.1λ	0.01λ	0.001λ
Δw	0.1λ	0.1λ	0.1λ	0.01λ	0.001λ
AMI_0	1.662	1.683	1.684	0.016	1.64E-04
AMI_1	1.662	1.663	1.663	0.016	1.64E-04
AMI_2	8.99E-03	8.39E-03	8.40E-03	8.91E-07	2.18E-06
AMI_3	8.43E-03	8.33E-03	8.33E-03	8.23E-07	5.69E-06
AMI_4	3.05E-05	2.02E-05	2.02E-05	6.18E-08	1.19E-05
AMI_5	2.08E-05	2.01E-05	2.02E-05	1.09E-07	2.12E-05
$AMII_0$	1.662	1.683	1.684	0.016	1.64E-04
$AMII_1$	1.662	1.663	1.663	0.016	1.64E-04
$AMII_2$	8.99E-03	8.39E-03	8.40E-03	8.82E-07	1.01E-10
$AMII_3$	8.43E-03	8.33E-03	8.33E-03	8.12E-07	9.49E-11
$AMII_4$	4.02E-05	2.42E-05	2.40E-05	9.25E-11	4.06E-12
$AMII_5$	4.02E-05	2.42E-05	2.40E-05	9.21E-11	1.22E-11
QI_2	2.62E-03	2.94E-03	2.94E-03	2.66E-07	3.82E-11
QI_4	9.28E-10	8.87E-10	9.18E-10	5.77E-11	1.38E-11
QI_6	1.50E-11	7.19E-12	5.49E-11	5.77E-11	1.37E-11
QI_8	1.49E-11	7.15E-12	5.49E-11	5.78E-11	1.38E-11
QI_{10}	1.49E-11	7.10E-12	5.49E-11	5.78E-11	1.38E-11
QI_{12}	1.49E-11	7.14E-12	5.50E-11	5.78E-11	1.37E-11
QI_{14}	1.49E-11	7.18E-12	5.49E-11	5.78E-11	1.38E-11
QI_{16}	1.32E-11	5.49E-12	5.67E-11	5.59E-11	1.56E-11
QI_{18}	1.49E-11	7.21E-12	5.49E-11	5.77E-11	1.39E-11
QI_{20}	1.49E-11	7.27E-12	5.50E-11	5.77E-11	1.37E-11
QI_{32}	1.49E-11	7.21E-12	5.50E-11	5.79E-11	1.35E-11
QI_{64}	1.47E-11	6.68E-12	5.49E-11	5.65E-11	1.33E-11
QI_{128}	1.76E-11	6.60E-12	5.49E-11	5.56E-11	1.21E-11
QI_{256}	1.73E-11	8.08E-12	5.66E-11	5.85E-11	2.39E-11
QI_{512}	4.11E-11	7.49E-13	2.20E-11	8.43E-11	2.26E-11

Table 3.15 Comparison of the absolute relative errors of $I_{3D\Lambda}$ using AMI, AMII and QI scheme with $(u_o,v_o,w_o)=(\Delta u,0,0)$, $\Delta u_i=\Delta u$ and various combinations of Δu, Δv and Δw

Δu	0.1λ	0.01λ	0.001λ	0.01λ	0.001λ
Δv	0.1λ	0.1λ	0.1λ	0.01λ	0.001λ
Δw	0.1λ	0.1λ	0.1λ	0.01λ	0.001λ
Δu_i	0.1λ	0.01λ	0.001λ	0.01λ	0.001λ
AMI_0	8.381	15.583	17.598	0.787	0.079
AMI_1	2.972	1.609	2.082	0.029	2.92E-04
AMI_2	0.236	0.126	0.187	2.29E-04	2.29E-07
AMI_3	0.038	7.99E-03	0.014	3.74E-06	2.95E-09

AMI_4	2.71E-03	4.30E-04	8.35E-04	2.67E-08	3.33E-09
AMI_5	2.78E-04	2.01E-05	4.84E-05	4.28E-09	3.33E-09
$AMII_0$	8.777	6298	7.06E+08	1.26E+00	0.960
$AMII_1$	3.964	6311	7.06E+08	9.88E-01	0.957
$AMII_2$	0.860	6310	7.06E+08	9.57E-01	0.957
$AMII_3$	0.971	6310	7.06E+08	9.57E-01	0.957
$AMII_4$	1.003	6310	7.06E+08	9.57E-01	0.957
$AMII_5$	1.001	6310	7.06E+08	9.57E-01	0.957
QI_2	0.514	18.576	29.399	4.53E-01	0.452
QI_4	0.062	5.201	14.803	5.99E-02	0.060
QI_6	0.011	1.903	9.521	1.10E-02	0.011
QI_8	3.55E-03	0.814	6.814	3.46E-03	3.46E-03
QI_{10}	1.48E-03	0.390	5.174	1.44E-03	1.44E-03
QI_{12}	7.27E-04	0.205	4.079	7.08E-04	7.08E-04
QI_{14}	3.98E-04	0.116	3.301	3.87E-04	3.87E-04
QI_{16}	2.36E-04	0.070	2.722	2.30E-04	2.30E-04
QI_{18}	1.48E-04	0.044	2.278	1.45E-04	1.45E-04
QI_{20}	9.81E-05	0.030	1.929	9.56E-05	9.56E-05
QI_{32}	1.54E-05	4.65E-03	0.827	1.50E-05	1.50E-05
QI_{64}	9.83E-07	2.99E-04	0.153	9.59E-07	9.60E-07
QI_{128}	5.77E-08	1.89E-05	0.015	5.71E-08	5.77E-08
QI_{256}	4.01E-09	1.18E-06	9.91E-04	3.90E-10	5.96E-10
QI_{512}	6.62E-09	6.31E-08	5.85E-05	3.96E-09	3.14E-09

Table 3.16 Comparison of the absolute relative errors of $I_{3D\Lambda}$ using AMI, AMII and QI scheme with $(u_o,v_o,w_o)=(0,\Delta v,0)$, $\Delta u_i=\Delta u$ and various combinations of Δu, Δv and Δw

Δu	0.1λ	0.01λ	0.001λ	0.01λ	0.001λ
Δv	0.1λ	0.1λ	0.1λ	0.01λ	0.001λ
Δw	0.1λ	0.1λ	0.1λ	0.01λ	0.001λ
Δu_i	0.1λ	0.01λ	0.001λ	0.01λ	0.001λ
AMI_0	3.375	2.748	2.808	0.300	0.030
AMI_1	1.583	1.561	1.566	0.016	1.57E-04
AMI_2	0.066	9.33E-03	0.010	6.43E-05	6.44E-08
AMI_3	9.37E-03	7.47E-03	7.50E-03	9.22E-07	3.45E-09
AMI_4	4.02E-04	3.37E-05	2.97E-05	4.34E-09	3.54E-09
AMI_5	3.08E-05	1.76E-05	1.77E-05	2.56E-09	3.54E-09
$AMII_0$	3.128	2.750	2.806	0.681	0.628
$AMII_1$	1.053	1.563	1.563	0.613	0.627
$AMII_2$	0.709	0.011	0.014	0.627	0.627
$AMII_3$	0.657	8.88E-03	0.013	0.627	0.627
$AMII_4$	0.650	1.13E-03	5.94E-03	0.627	0.627
$AMII_5$	0.650	1.13E-03	5.94E-03	0.627	0.627
QI_2	0.638	0.800	0.809	0.601	0.600
QI_4	2.20E-03	6.31E-03	6.46E-03	2.14E-03	2.14E-03
QI_6	3.87E-05	9.48E-05	9.76E-05	3.78E-05	3.78E-05

QI_8	6.61E-07	1.80E-06	1.87E-06	6.46E-07	6.45E-07
QI_{10}	1.16E-08	3.79E-08	3.90E-08	1.03E-08	9.19E-09
QI_{12}	2.71E-09	2.33E-09	2.88E-09	2.27E-09	3.27E-09
QI_{14}	2.86E-09	2.24E-09	2.99E-09	2.52E-09	3.54E-09
QI_{16}	2.86E-09	2.24E-09	3.00E-09	2.53E-09	3.54E-09
QI_{18}	2.86E-09	2.24E-09	3.00E-09	2.53E-09	3.54E-09
QI_{20}	2.86E-09	2.24E-09	3.00E-09	2.53E-09	3.54E-09
QI_{32}	2.86E-09	2.24E-09	3.00E-09	2.53E-09	3.54E-09
QI_{64}	2.86E-09	2.24E-09	3.00E-09	2.53E-09	3.54E-09
QI_{128}	2.84E-09	2.23E-09	2.99E-09	2.51E-09	3.55E-09
QI_{256}	2.86E-09	2.21E-09	2.94E-09	2.50E-09	3.54E-09
QI_{512}	2.72E-09	2.32E-09	3.07E-09	2.80E-09	3.60E-09

Table 3.17 Comparison of the absolute relative errors of $I_{3D\Lambda}$ using AMI, AMII and QI scheme with $(u_o,v_o,w_o)=(0,0,0.1\lambda)$, $\Delta u_i=\Delta u$ and various combinations of Δu, Δv and Δw

Δu	0.1λ	0.01λ	0.001λ	0.01λ	0.001λ
Δv	0.1λ	0.1λ	0.1λ	0.01λ	0.001λ
Δw	0.1λ	0.1λ	0.1λ	0.01λ	0.001λ
Δu_i	0.1λ	0.01λ	0.001λ	0.01λ	0.001λ
AMI_0	3.375	2.748	2.808	0.031	3.09E-04
AMI_1	1.583	1.561	1.566	0.016	1.65E-04
AMI_2	0.066	9.33E-03	0.010	7.77E-06	2.40E-07
AMI_3	9.37E-03	7.47E-03	7.50E-03	8.10E-07	2.32E-07
AMI_4	4.02E-04	3.37E-05	2.97E-05	3.73E-09	2.34E-07
AMI_5	3.08E-05	1.76E-05	1.77E-05	3.87E-09	2.35E-07
$AMII_0$	3.128	2.750	2.806	0.031	3.09E-04
$AMII_1$	1.053	1.563	1.563	0.016	1.64E-04
$AMII_2$	0.709	0.011	0.014	8.51E-06	4.08E-09
$AMII_3$	0.657	8.88E-03	0.013	1.73E-06	3.94E-09
$AMII_4$	0.650	1.13E-03	5.94E-03	1.01E-06	4.02E-09
$AMII_5$	0.650	1.13E-03	5.94E-03	1.01E-06	4.02E-09
QI_2	0.638	0.800	0.809	1.22E-04	9.55E-09
QI_4	2.20E-03	6.31E-03	6.46E-03	3.85E-09	4.02E-09
QI_6	3.87E-05	9.48E-05	9.76E-05	3.87E-09	4.02E-09
QI_8	6.61E-07	1.80E-06	1.87E-06	3.87E-09	4.02E-09
QI_{10}	1.17E-08	3.79E-08	3.90E-08	3.87E-09	4.02E-09
QI_{12}	2.68E-09	2.27E-09	2.88E-09	3.87E-09	4.02E-09
QI_{14}	2.82E-09	2.17E-09	2.99E-09	3.87E-09	4.02E-09
QI_{16}	2.82E-09	2.18E-09	2.99E-09	3.87E-09	4.02E-09
QI_{18}	2.82E-09	2.18E-09	3.00E-09	3.87E-09	4.02E-09
QI_{20}	2.82E-09	2.18E-09	3.00E-09	3.87E-09	4.02E-09
QI_{32}	2.82E-09	2.18E-09	3.00E-09	3.87E-09	4.02E-09
QI_{64}	2.82E-09	2.17E-09	3.00E-09	3.87E-09	4.02E-09
QI_{128}	2.81E-09	2.17E-09	2.99E-09	3.88E-09	4.03E-09
QI_{256}	2.84E-09	2.14E-09	2.93E-09	3.87E-09	3.93E-09
QI_{512}	2.68E-09	2.26E-09	3.07E-09	3.67E-09	4.48E-09

Table 3.18 Comparison of the absolute relative errors of $I_{3D\Lambda}$ using AMI, AMII and QI scheme with $(u_o,v_o,w_o)=(0,2\Delta v,0)$, $\Delta u_i=\Delta u$ and various combinations of Δu, Δv and Δw

Δu	0.1λ	0.01λ	0.001λ	0.01λ	0.001λ
Δv	0.1λ	0.1λ	0.1λ	0.01λ	0.001λ
Δw	0.1λ	0.1λ	0.1λ	0.01λ	0.001λ
Δu_i	0.1λ	0.01λ	0.001λ	0.01λ	0.001λ
AMI_0	2.126	2.063	2.081	0.139	0.014
AMI_1	1.626	1.637	1.638	0.016	1.61E-04
AMI_2	0.038	8.74E-03	8.94E-03	3.64E-05	3.66E-08
AMI_3	8.56E-03	8.00E-03	8.01E-03	8.40E-07	7.37E-10
AMI_4	2.21E-04	2.55E-05	2.41E-05	4.61E-09	8.20E-10
AMI_5	2.30E-05	1.88E-05	1.88E-05	4.08E-09	8.20E-10
$AMII_0$	2.116	2.063	2.081	0.138	0.019
$AMII_1$	1.613	1.637	1.638	3.01E-03	0.013
$AMII_2$	0.056	9.09E-03	9.28E-03	0.014	0.014
$AMII_3$	0.019	8.06E-03	8.07E-03	0.014	0.014
$AMII_4$	0.015	3.42E-04	2.79E-04	0.014	0.014
$AMII_5$	0.015	3.42E-04	2.79E-04	0.014	0.014
QI_2	0.074	0.052	0.052	0.062	0.062
QI_4	1.07E-05	1.18E-05	1.19E-05	9.80E-06	9.80E-06
QI_6	1.64E-09	3.61E-09	2.16E-09	2.46E-09	8.22E-10
QI_8	1.89E-09	3.03E-09	1.45E-09	4.05E-09	8.20E-10
QI_{10}	1.89E-09	3.03E-09	1.46E-09	4.06E-09	8.20E-10
QI_{12}	1.89E-09	3.03E-09	1.46E-09	4.06E-09	8.20E-10
QI_{14}	1.89E-09	3.03E-09	1.46E-09	4.06E-09	8.20E-10
QI_{16}	1.89E-09	3.03E-09	1.45E-09	4.05E-09	8.18E-10
QI_{18}	1.89E-09	3.03E-09	1.46E-09	4.06E-09	8.20E-10
QI_{20}	1.89E-09	3.03E-09	1.46E-09	4.06E-09	8.20E-10
QI_{32}	1.89E-09	3.03E-09	1.45E-09	4.06E-09	8.20E-10
QI_{64}	1.89E-09	3.03E-09	1.46E-09	4.06E-09	8.15E-10
QI_{128}	1.88E-09	3.04E-09	1.45E-09	4.02E-09	8.41E-10
QI_{256}	1.91E-09	3.08E-09	1.38E-09	4.04E-09	8.72E-10
QI_{512}	1.85E-09	3.11E-09	1.36E-09	3.97E-09	1.40E-09

Table 3.19 Comparison of the absolute relative errors of $I_{3D\Lambda}$ using AMI, AMII and QI scheme with $(u_o,v_o,w_o)=(\Delta u,\Delta v,1\lambda)$, $\Delta u_i=\Delta u$ and various combinations of Δu, Δv and Δw

Δu	0.1λ	0.01λ	0.001λ	0.01λ	0.001λ
Δv	0.1λ	0.1λ	0.1λ	0.01λ	0.001λ
Δw	0.1λ	0.1λ	0.1λ	0.01λ	0.001λ
Δu_i	0.1λ	0.01λ	0.001λ	0.01λ	0.001λ
AMI_0	2.118	1.681	1.684	0.021	4.07E-03
AMI_1	1.683	1.663	1.663	0.016	0.027

AMI_2	0.026	8.37E-03	8.01E-03	2.05E-05	0.095
AMI_3	8.87E-03	8.33E-03	8.01E-03	5.16E-05	0.244
AMI_4	1.38E-04	2.04E-05	2.30E-03	1.05E-04	0.498
AMI_5	2.33E-05	2.02E-05	4.19E-03	1.77E-04	0.849
$AMII_0$	2.118	1.681	1.684	0.021	2.10E-04
$AMII_1$	1.683	1.663	1.663	0.016	1.64E-04
$AMII_2$	0.026	8.37E-03	8.40E-03	2.63E-06	7.59E-10
$AMII_3$	8.86E-03	8.33E-03	8.33E-03	8.13E-07	7.17E-10
$AMII_4$	1.52E-04	2.43E-05	2.40E-05	1.72E-10	8.07E-10
$AMII_5$	6.67E-05	2.43E-05	2.40E-05	1.19E-10	8.08E-10
QI_2	3.43E-04	2.94E-03	2.94E-03	5.51E-08	8.01E-10
QI_4	4.00E-09	7.15E-10	3.19E-09	1.20E-10	7.98E-10
QI_6	3.25E-09	2.81E-10	3.56E-09	1.20E-10	7.98E-10
QI_8	3.25E-09	2.80E-10	3.56E-09	1.20E-10	7.98E-10
QI_{10}	3.25E-09	2.81E-10	3.56E-09	1.20E-10	7.99E-10
QI_{12}	3.25E-09	2.80E-10	3.56E-09	1.20E-10	7.98E-10
QI_{14}	3.25E-09	2.81E-10	3.56E-09	1.20E-10	7.98E-10
QI_{16}	3.24E-09	2.78E-10	3.56E-09	1.22E-10	7.96E-10
QI_{18}	3.25E-09	2.80E-10	3.56E-09	1.19E-10	7.98E-10
QI_{20}	3.25E-09	2.81E-10	3.56E-09	1.20E-10	7.98E-10
QI_{32}	3.25E-09	2.79E-10	3.56E-09	1.19E-10	7.98E-10
QI_{64}	3.25E-09	2.79E-10	3.56E-09	1.21E-10	8.00E-10
QI_{128}	3.23E-09	2.79E-10	3.56E-09	1.20E-10	8.07E-10
QI_{256}	3.26E-09	2.55E-10	3.59E-09	1.87E-10	8.94E-10
QI_{512}	3.71E-09	8.14E-11	3.55E-09	7.65E-11	1.56E-09

3.5 Conclusions

The analytical method to evaluate the MoM impedance matrix elements efficiently with good accuracy has been described in details. Two regions, region I (AMI) and region II (AMII), are defined so as to further improve the efficiently of the analytical method without loss in accuracy. The evaluations of matrix elements in these two regions have been proven to be highly efficient when compared to the QI scheme. To conclude this chapter, the observations on the efficiency and accuracy of the proposed analytical method are summarised as follows:

- Improving the accuracy of AMI_n and $AMII_n$ by increasing n does not suffer much in computational efficiency, which is a desirable feature if highly accurate solution is needed.

- QI scheme becomes highly inefficient if large N is employed to achieve the required accuracy.
- With the least possible number of N, the QI_2 scheme is only slightly faster than AMI but slower than AMII. However, it is far less accurate than AMI and AMII.
- From QI_4 scheme onwards, it is much slower than AMI and AMII. Hence, AMI and AMII are very efficient when compared to QI_4 to QI_{1024} schemes.
- When the singular point resides in the region of integration, AMI is capable of achieving highly accurate integral. Also, to obtain highly accurate integral, R_o should be greater than $2\times\max(\Delta u,\Delta v,\Delta w)$.
- Both AMI and AMII can produce highly accurate integral even for long and thin cell, however, low order QI scheme unable to produce the necessary accuracy for this kind of cell, especially when the source cell is very near to the field cell.

CHAPTER FOUR

4 COMPARISON OF ACCURACY AND COMPUTATIONAL EFFICIENCY

Based on Electric Field Integral Equations (EFIEs) described in Chapter 2, two separate Method of Moments (MoM) computer codes using C programming language have been developed. One MoM code adopts the proposed analytical method (PM) for the evaluation of integrals described in Chapter 3 and another MoM code uses the conventional quadrature integration (QI) scheme for the evaluation of integrals. Using microstrip line structures as test cases, the accuracy and efficiency of MoM code with PM will be compared with the MoM code with QI.

4.1 Accuracy and Efficiency of the Proposed Analytical Method

To investigate the accuracy and efficiency of the proposed analytical method mentioned in Chapter 3, two MoM codes have been developed for both the PM and the QI scheme. For the PM, the 5^{th} order integral is chosen. The criterion for choosing AMI_5 or $AMII_5$ has been defined in Table 3.3 of Chapter 3 and will not be repeated here. For the QI scheme, QI_{16} and QI_{128} are selected to compare with the PM. QI_{16} is chosen because it is a compromise between reasonable accuracy and computational efficiency and QI_{128} is selected as a reference for the accuracy comparison with PM and QI_{16}. QI_{1024} is not selected as it is computational prohibitive. All three approaches (PM,

Q_{16} and Q_{1024}) employ the robust generalized minimal residual algorithm (GMRES) [101] for the matrix solution.

A short-circuited microstrip line structure as shown in Fig. 4.1 with different geometrical dimensions will be used as a test case for all the simulations. In Fig. 4.1, h, w, l, w_s and ε_r are the thickness of the substrate, the width of the conductor trace, the length of the conductor trace, the width of the substrate and the substrate relative permittivity, respectively. In the simulations that follows, ε_r = 4.5, l = 100 mm, h = 1 mm, Δl = 2.5 mm and $\Delta w = w$ are kept unchanged. w_s and w are varied with four combinations: w_s = 50 mm and w = 10 mm, w_s = 5 mm and w = 1 mm, w_s = 1 mm and w = 0.2 mm, and w_s = 0.5 mm and w = 0.1 mm. As the ratio w_s : w of the four combinations are the same, the total number of cells for all the simulations is kept at 995. For each simulation, a 1 V source voltage will be applied at the open-end of the microstrip line with the other end short-circuited. The simulated frequency ranges from 50 MHz to 1 GHz at equal frequency steps of 50 MHz.

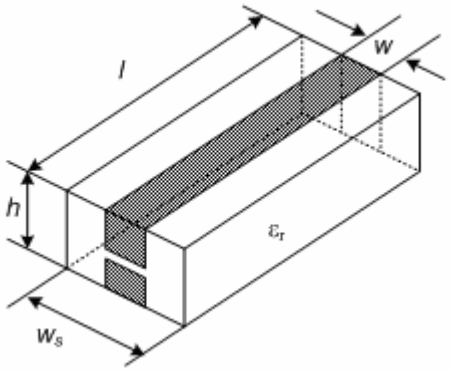

Fig. 4.1 A short-circuited microstrip line

To compare the computational efficiency of the three approaches, the matrix-fill time and matrix-solution time of each of the three approaches are tabulated in Table 4.1 for comparison purposes. The followings are observed:

- As the matrix size has been kept unchanged, the matrix-solution times are practically the same with very slight variations.
- As expected, the matrix-fill time of PM is the fastest amongst the three approaches. The computational efficiency ratio of t_{AM}:t_{QI16} and t_{AM}:t_{QI128} are about 1:20 and 1:75,000, respectively.
- For the PM, the total solution time is limited very much by the matrix-solution time.
- However, for both QI_{16} and QI_{128}, the total solution time is dominated by the matrix-fill time, which can be very significant for QI_{128}.

Table 4.1 Comparison of Matrix-fill and matrix-solution times for the microstrip line with varying w_s and w

w_s	50 mm	5 mm	1 mm	0.5 mm
w	10 mm	1 mm	0.2 mm	0.1 mm
PM (matrix-fill time)	0.703 s	0.703 s	0.703 s	0.703 s
QI_{16} (matrix-fill time)	14.484 s	14.484 s	14.484 s	14.484 s
QI_{128} (matrix-fill time)	53202 s	53695 s	53197 s	53434 s
PM (matrix-solution time)	3.203 s	2.766 s	2.516 s	2.453 s
QI_{16} (matrix-solution time)	3.219 s	2.718 s	2.547 s	2.657 s
QI_{128} (matrix-solution time)	3.219 s	2.782 s	2.563 s	2.719 s

To investigate the accuracy of the three approaches, the current distributions along the microstrip line at four selected frequencies: 50 MHz (the lowest simulated frequency), 500 MHz (the mid simulated frequency), 1 GHz (the highest simulated frequency) and frequency near to the resonant are plotted in Fig. 4.2 to Fig. 4.9. In general, the current distribution plots along the microstrip line at the four selected frequencies agree very

well between the PM and the QI_{128}, whereas the QI_{16} has shown significant deviation from the other two approaches.

In Fig. 4.2 to Fig. 4.9, there are four different aspect ratios for Δl:Δw. These aspect ratios are Δl:Δw = 0.25:1 for Fig. 4.2 and Fig. 4.3; Δl:Δw = 2.5:1 for Fig. 4.4 and Fig. 4.5; Δl:Δw = 12.5:1 for Fig. 4.6 and Fig. 4.7; and Δl:Δw = 25:1 for Fig. 4.8 and Fig. 4.9. The best agreement between the PM and the QI_{128} in Fig. 4.4 and Fig. 4.5 is observed because the difference in the aspect ratio Δl:Δw is the smallest. On the other hand, Fig. 4.9 shows that at 1 GHz, the PM and the QI_{128} do not agree as well due to the largest aspect ratio Δl:Δw. As explained in Chapter 3, when aspect ratio of Δl:Δw or Δw:Δl is very large, the QI_N integration method becomes inaccurate due to poor convergence. Of course, one could increase N to achieve the accuracy but at the expense of long computation time. However, the PM does not show any problem in accuracy even for very large aspect ratio of Δl:Δw or Δw:Δl. Hence, the PM has been demonstrated its robustness in terms of both accuracy and computational efficiency.

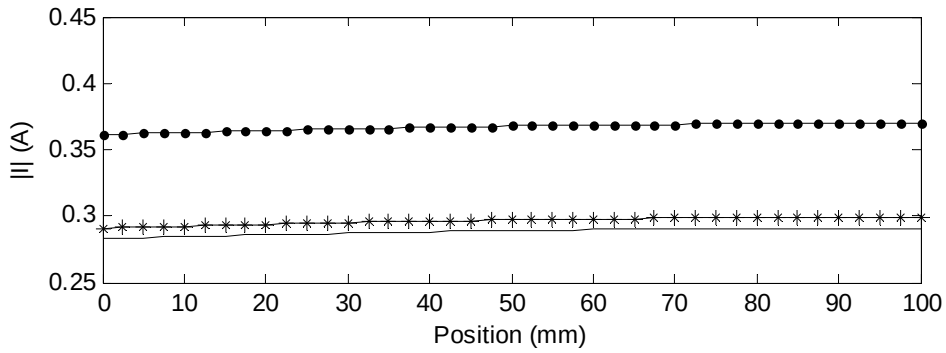

(a)

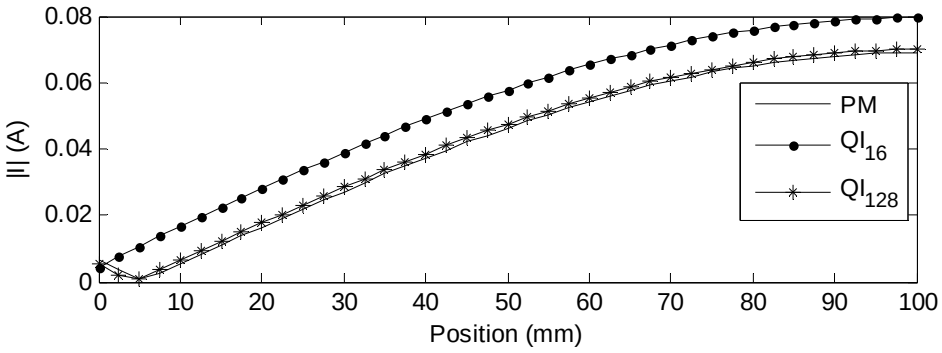

(b)

Fig. 4.2 Current along microstrip line with l=100 mm, w_s=50 mm, w=10 mm, Δl=2.5 mm and with the load end short-circuited at 50 MHz (a) and 350 MHz (b)

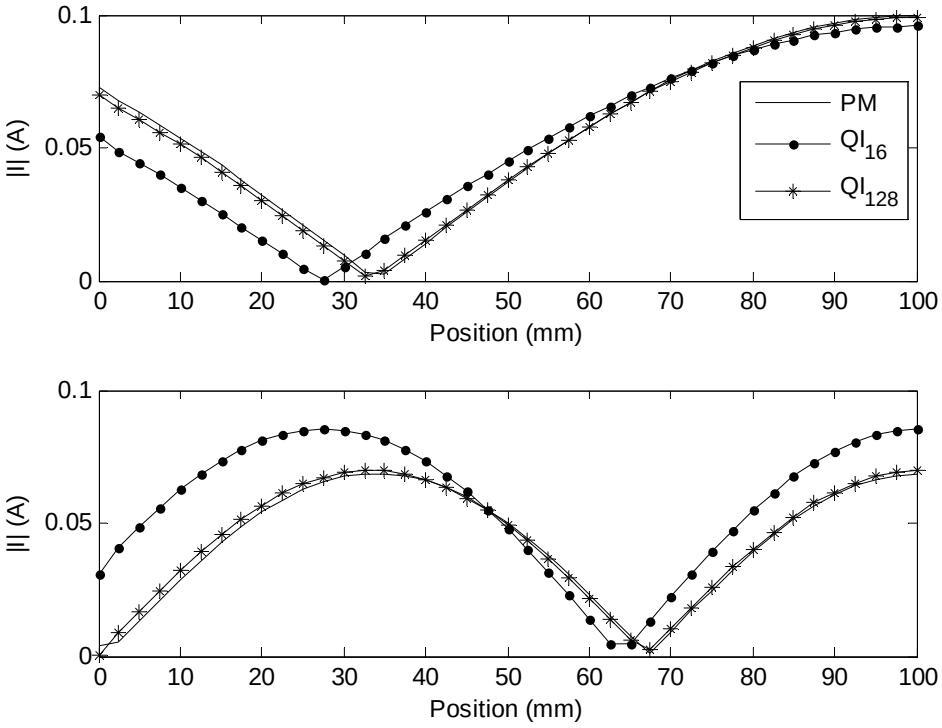

Fig. 4.3 Current along microstrip line with l=100 mm, w_s=50 mm, w=10 mm, Δl=2.5 mm and with the load end short-circuited at 500 MHz (top) and 1000 MHz (bottom)

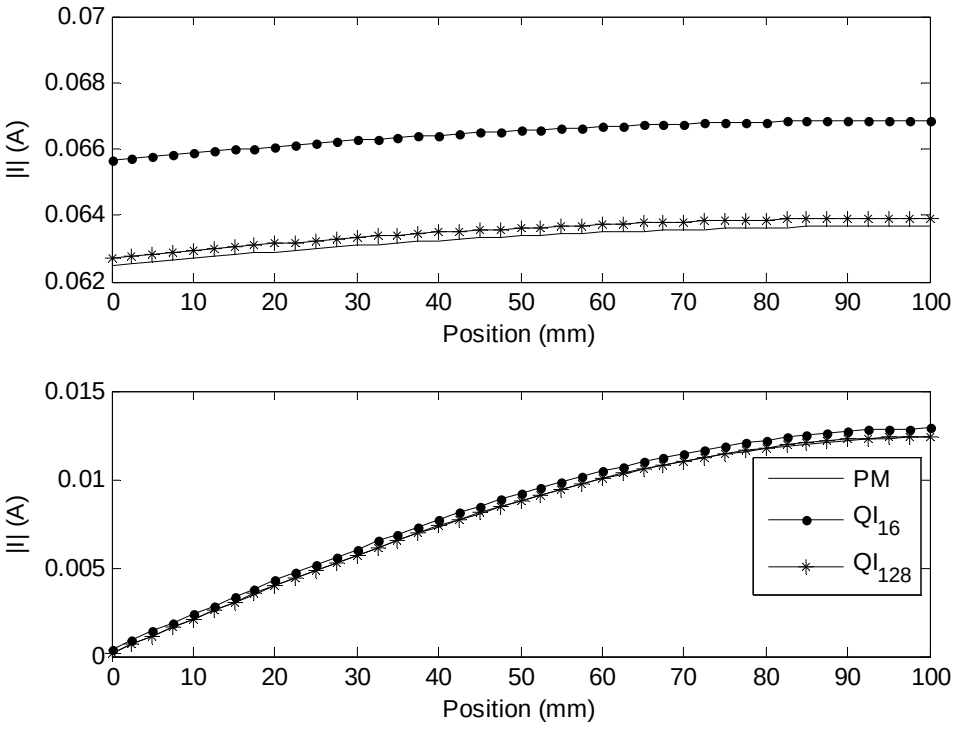

Fig. 4.4 Current along microstrip line with l=100 mm, w_s=5 mm, w=1 mm, Δl=2.5 mm and with the load end short-circuited at 50 MHz (top) and 400 MHz (bottom)

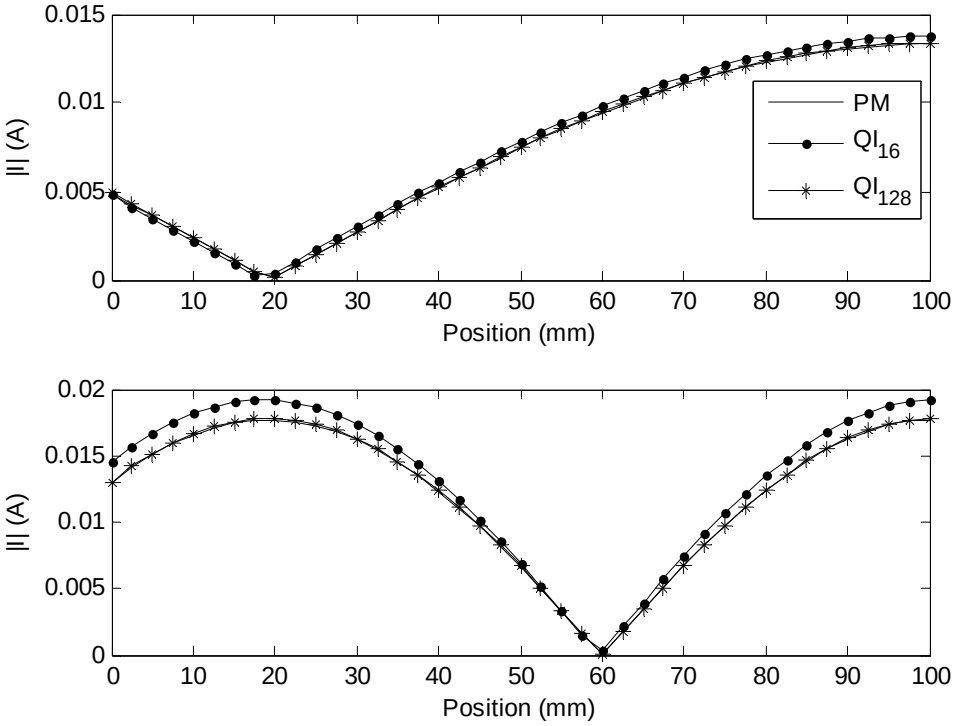

Fig. 4.5 Current along microstrip line with l=100 mm, w_s=5 mm, w=1 mm, Δl=2.5 mm and with the load end short-circuited at 500 MHz (top) and 1000 MHz (bottom)

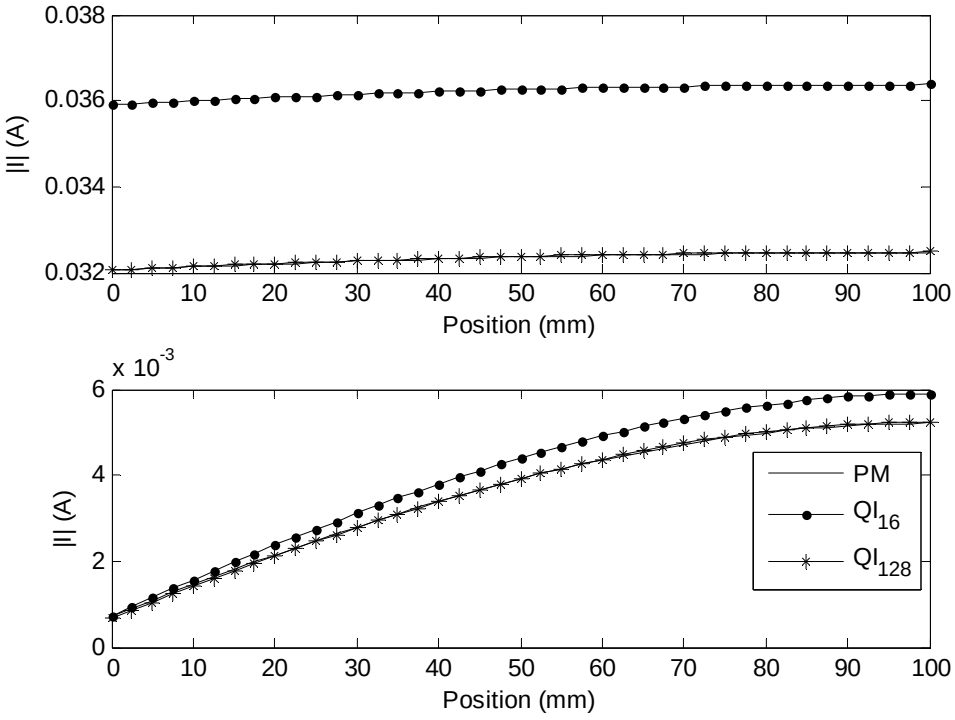

Fig. 4.6 Current along microstrip line with l=100 mm, w_s=1 mm, w=0.2 mm, Δl=2.5 mm and with the load end short-circuited at 50 MHz (top) and 450 MHz (bottom)

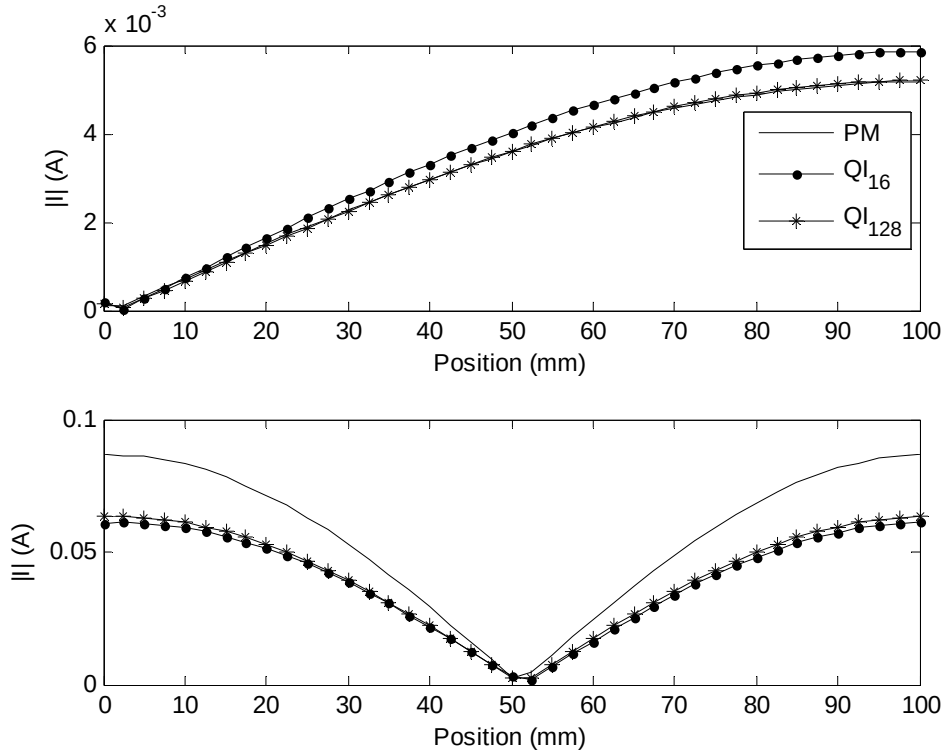

Fig. 4.7 Current along microstrip line with l=100 mm, w_s=1 mm, w=0.2 mm, Δl=2.5 mm and with the load end short-circuited at 500 MHz (top) and 1000 MHz (bottom)

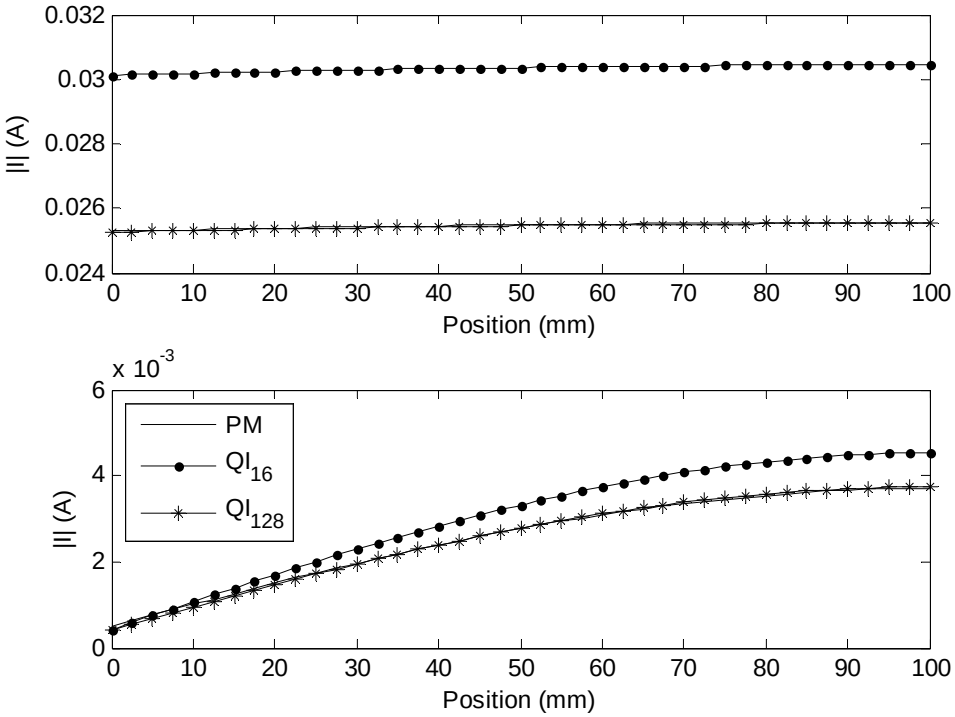

Fig. 4.8 Current along microstrip line with l=100 mm, w_s=0.5 mm, w=0.1 mm, Δl=2.5 mm and with the load end short-circuited at 50 MHz (top) and 500 MHz (bottom)

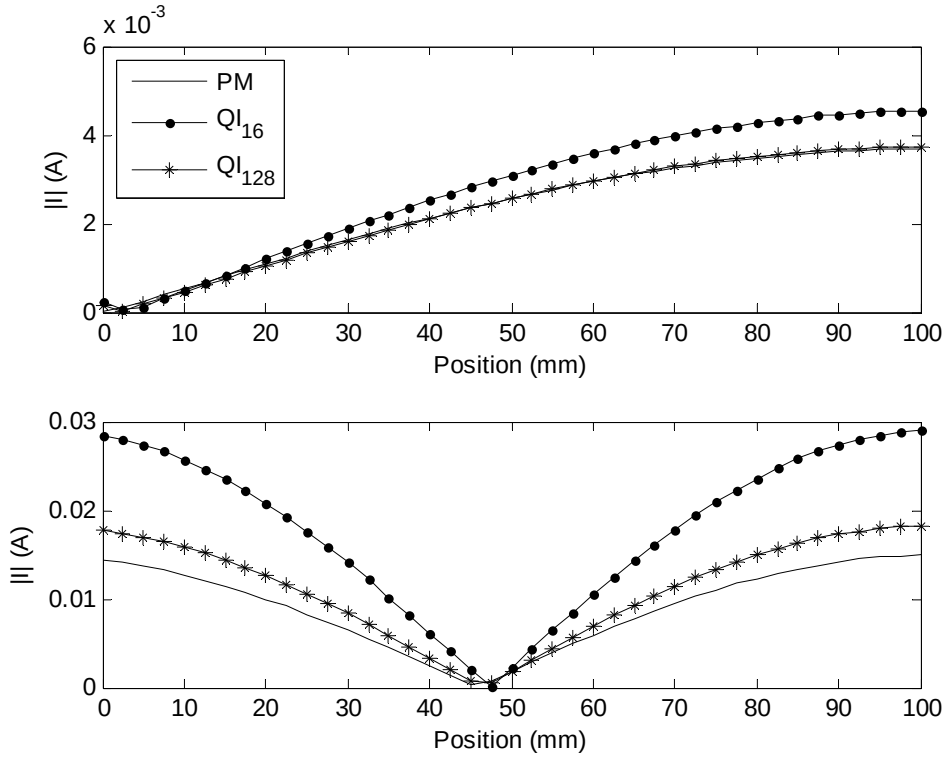

Fig. 4.9 Current along microstrip line with l=100 mm, w_s=0.5 mm, w=0.1 mm, Δl=2.5 mm and with the load end short-circuited at 550 MHz (top) and 1000 MHz (bottom)

4.2 S-parameter and Far-field Radiation

Besides the current distribution plots, further investigation is carried out to check the accuracy of the PM. Two commonly used parameters, the S-parameter and the radiated electric field for the same microstrip line are computed using the three approaches and plotted. Fig. 4.10 to Fig. 4.13 show the comparison of the S-parameter and Fig. 4.14 to Fig. 4.17 show the comparison of the maximum electric field at 3 m distance.

Again, from theses plots, it can be observed that the PM is in closed agreement with the QI_{128} and QI_{16} deviates significantly from the other two approaches. Hence, the PM has been proven to work well for the S-parameter extraction and far field radiation.

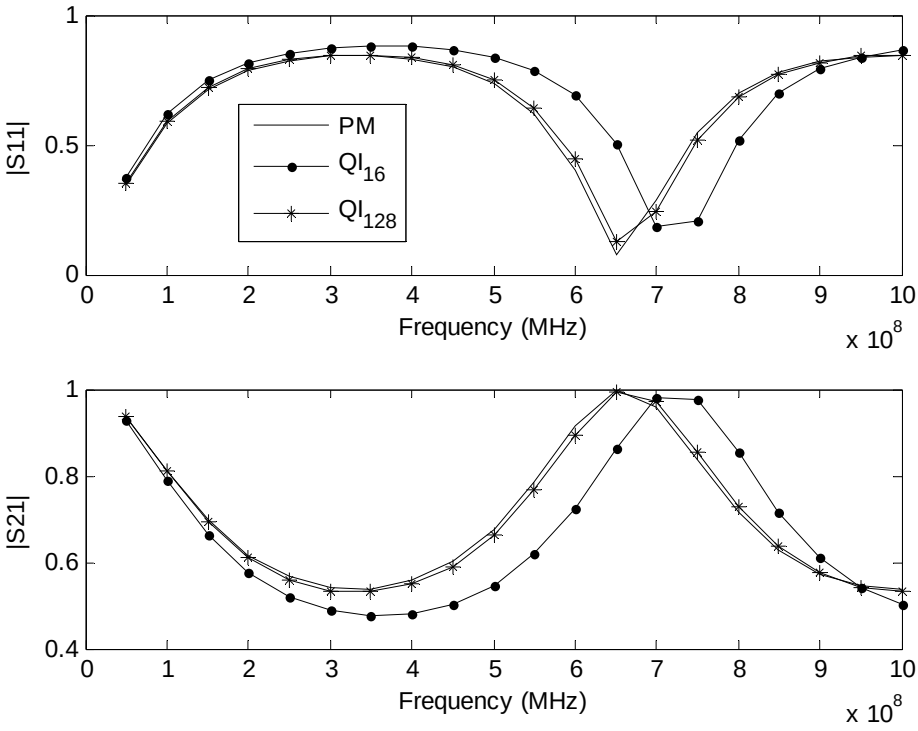

Fig. 4.10 S-parameters versus frequency with l=100 mm, w_s=50 mm, w=10 mm, Δl=2.5 mm

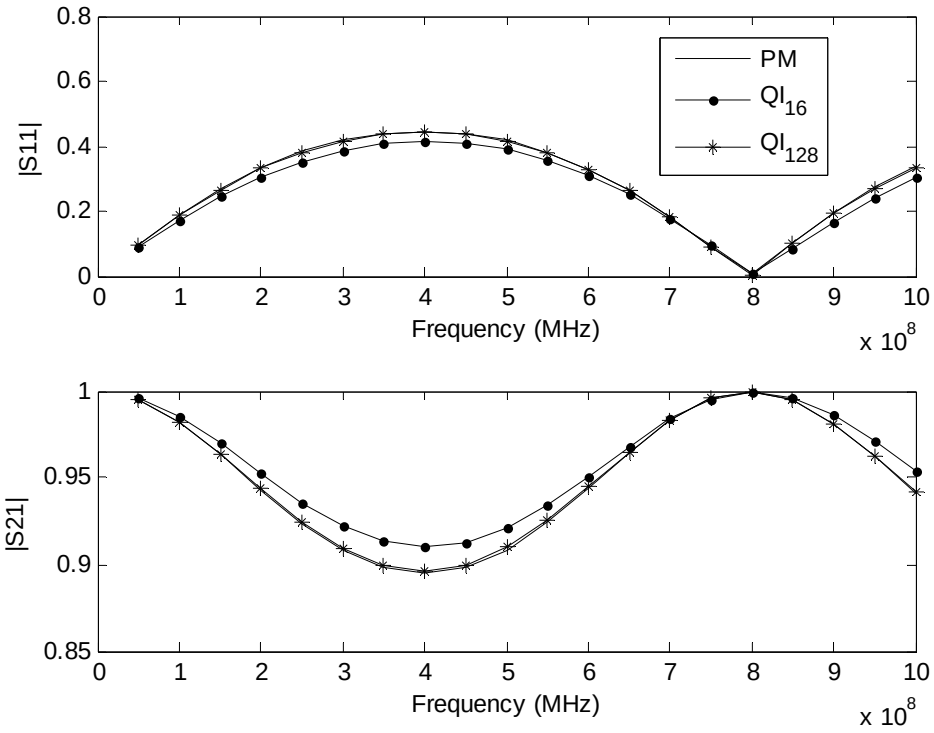

Fig. 4.11 S-parameters versus frequency with l=100 mm, w_s=5 mm, w=1 mm, Δl=2.5 mm

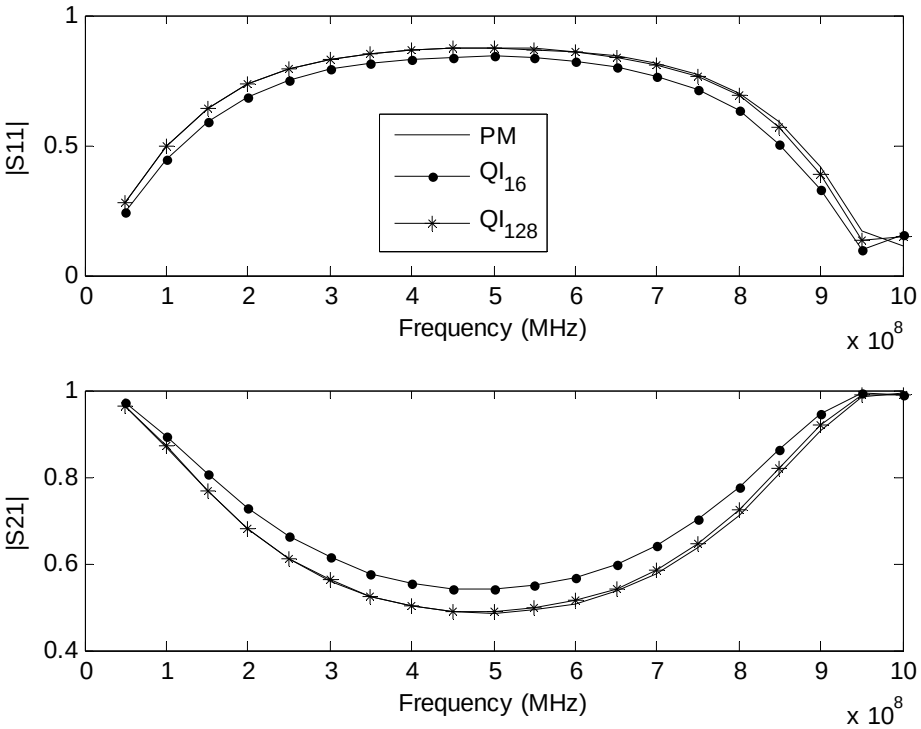

Fig. 4.12 S-parameters versus frequency with l=100 mm, w_s=1 mm, w=0.2 mm, Δl=2.5 mm

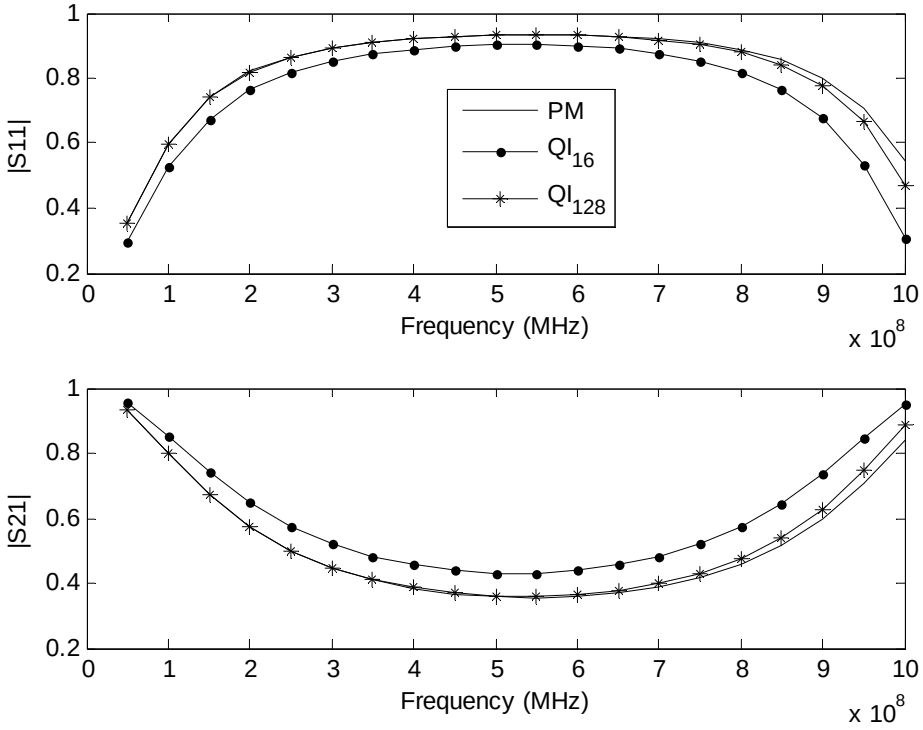

Fig. 4.13 S-parameters versus frequency with l=100 mm, w_s=0.5 mm, w=0.1 mm, Δl=2.5 mm

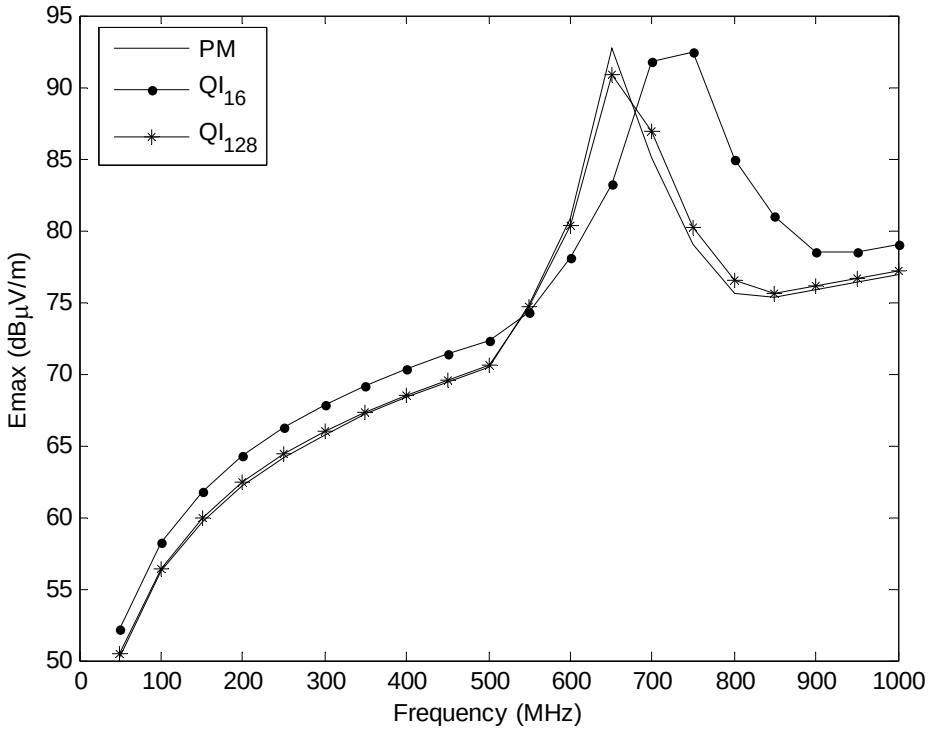

Fig. 4.14 Maximum E-field at 3 m versus frequency with l=100 mm, w_s=50 mm, w=10 mm, Δl=2.5 mm

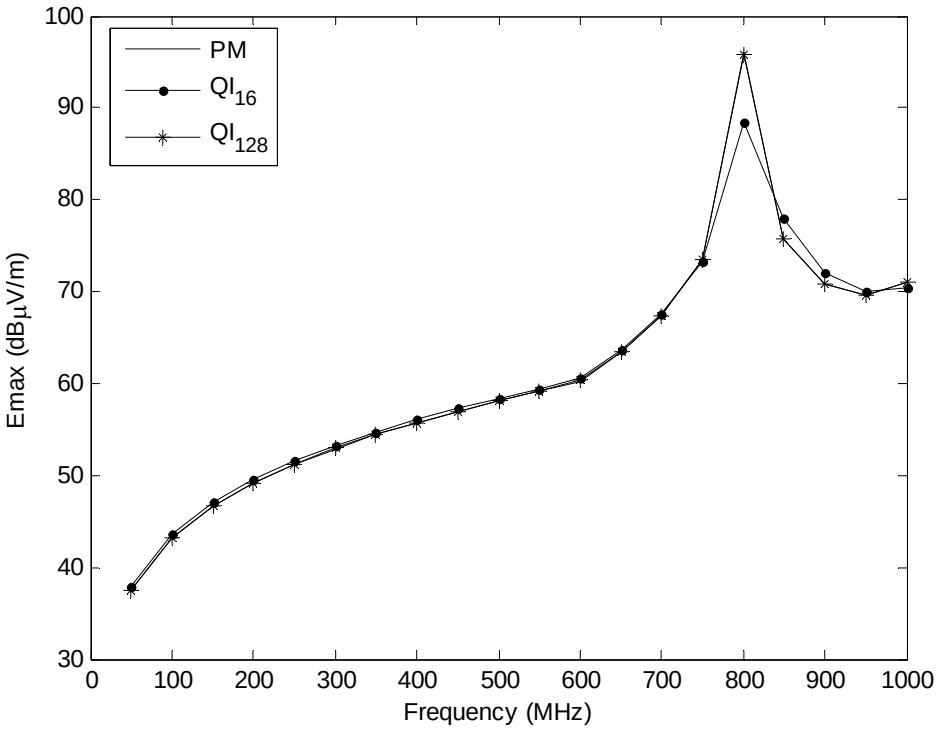

Fig. 4.15 Maximum E-field at 3 m versus frequency with l=100 mm, w_s=5 mm, w=1 mm, Δl=2.5 mm

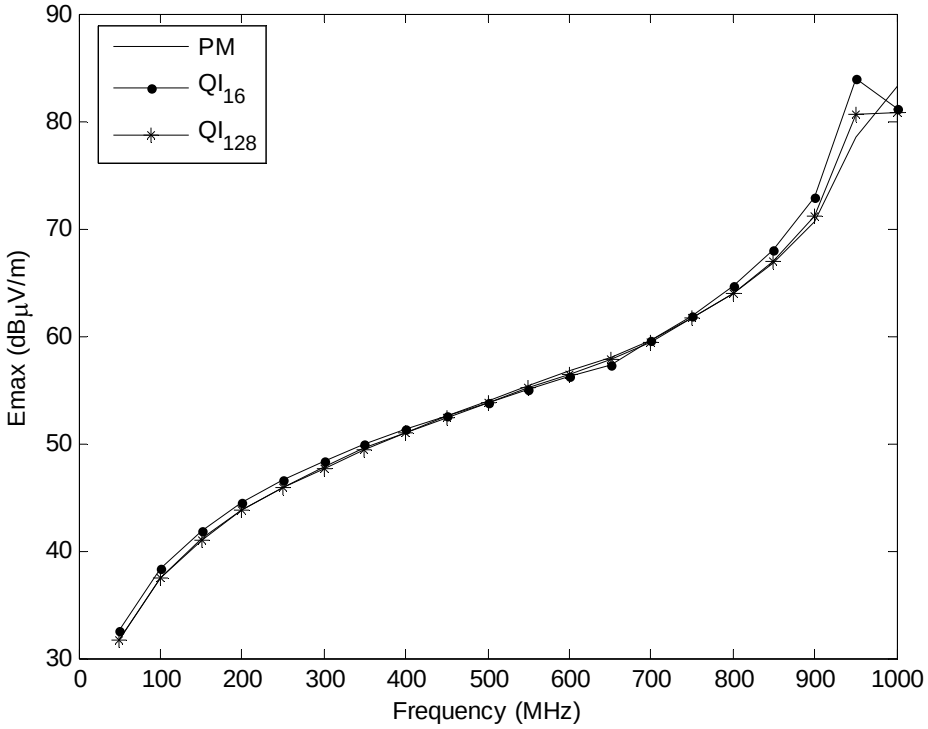

Fig. 4.16 Maximum E-field at 3 m versus frequency with l=100 mm, w_s=1 mm, w=0.2 mm, Δl=2.5 mm

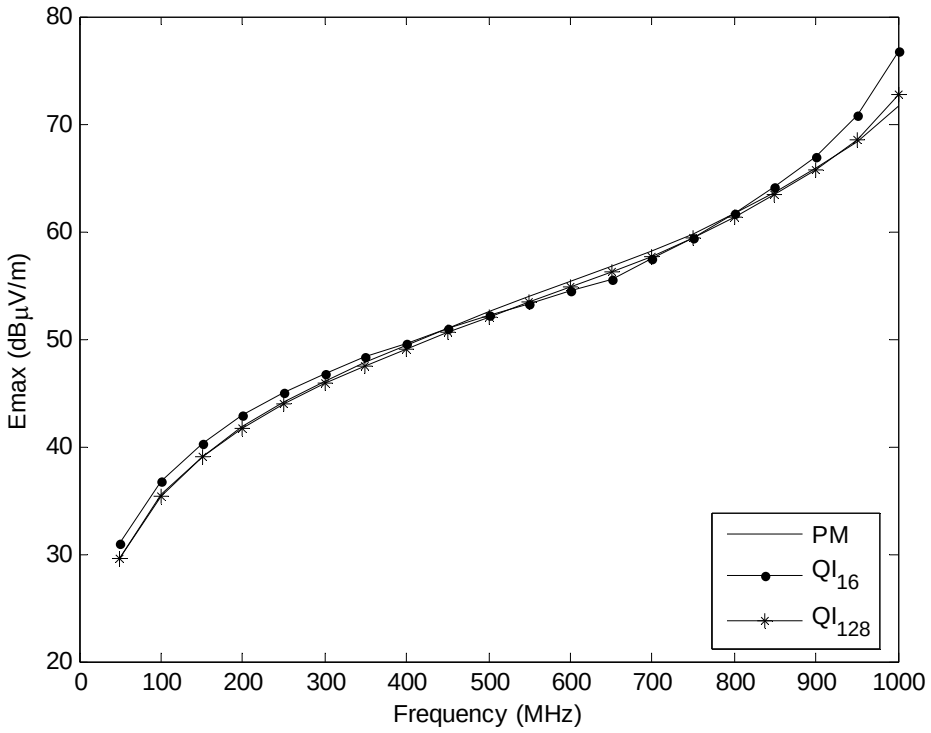

Fig. 4.17 Maximum E-field at 3 m versus frequency with l=100 mm, w_s=0.5 mm, w=0.1 mm, Δl=2.5 mm

In conclusion, the proposed analytical method for integral evaluation has been proven to be accurate, efficient and robust in MoM solver, even when the aspect ratio of the cell is large.

4.3 Application

To illustrate that the developed MoM code can deal with the near-field mutual coupling effect correctly, a circuit board with two parallel and uniform microstrip lines shown in Fig 4.18 is studied [102]. The substrate has a dielectric constant of (ε_r) of 2.2 and a thickness (h) of 1.55mm. The strip width w is 4.8 mm, and strip separation s is equal to the strip width of 4.8 mm. The line length l is 20 cm. Ports 1, 2, 3 and 4 are terminated in 50Ω, which is the characteristic impedance of the microstrip lines. Line 1 is excited at port 1. The other line is the victim line. The linear frequency sweep from the lowest

measurement frequency (100 MHz) to the highest measurement frequency (1.5 GHz) in steps of 50MHz is set to be the frequency range of interest. Simulated and measured results for the near-end and the far- end crosstalk are examined.

The discretization sizes for the trace simulation are: Δx = 5mm, Δy = 1.6 mm, substrate width= 2.4×6+1.6×9+2.4×6 = 43.2 mm, substrate height =Δz = 1.55mm and ε_r = 2.2. The proposed analytical approach is performed to extract crosstalk results. Scattering parameters (unit in dB) versus frequency results are compared with the measurement data. As we can see in Figs. 4.19 and 4.20, both simulated near-end and far-end crosstalk results using the proposed approach agree very well with the measured results up to GHz range.

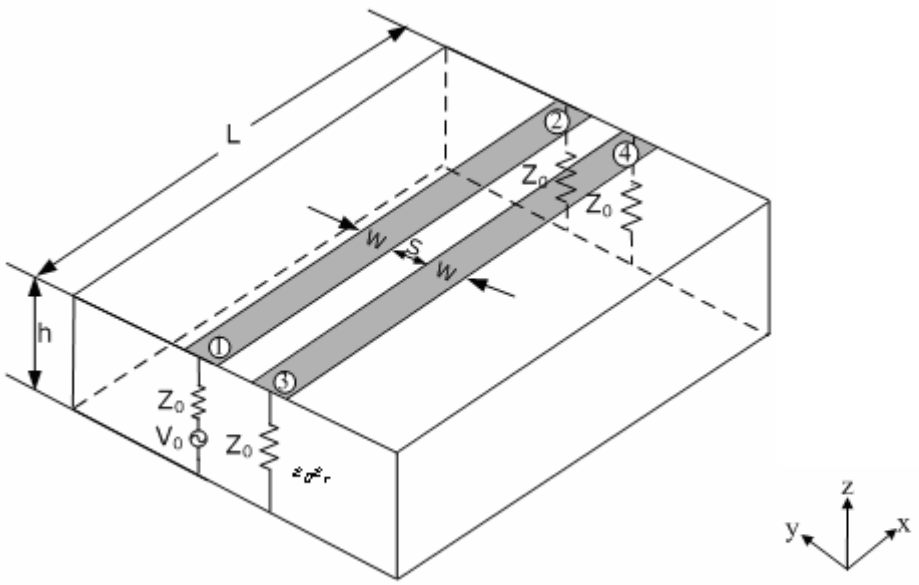

Fig. 4.18 Crosstalk structure. Port1 is excited

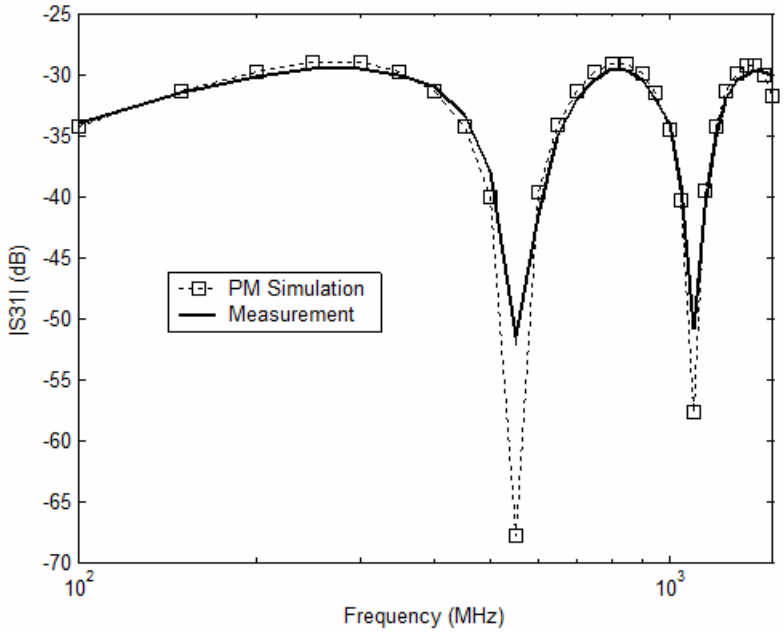

Fig. 4.19 Comparison of simulated and measured S_{31} (near-end crosstalk)

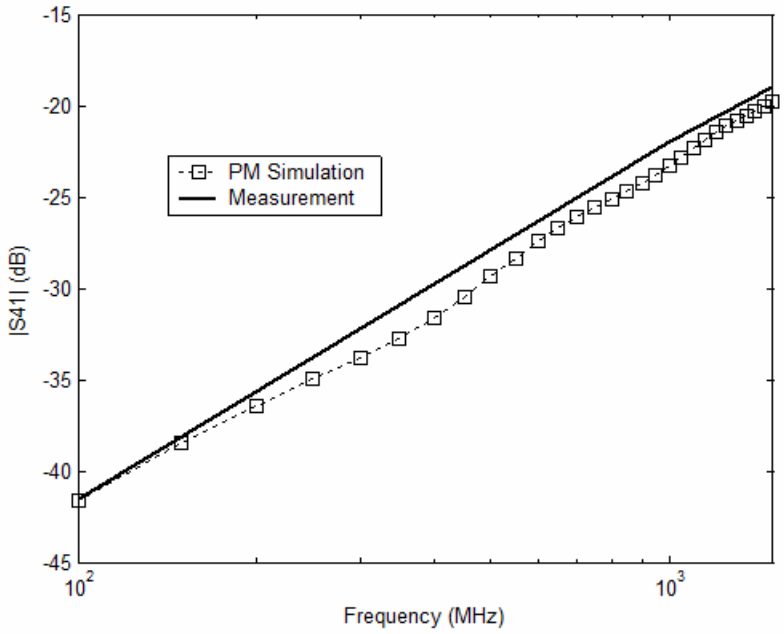

Fig. 4.20 Comparison of simulated and measured S_{41} (far-end crosstalk)

CHAPTER FIVE

5 CONCLUSIONS AND RECOMMENDED FUTURE WORK

5.1 Conclusions

Based on the Taylor's series expansion of the Green's function, an efficient and accurate generalised analytical approach has been developed for the evaluation of the matrix elements in MoM solver. The proposed generalised analytical approach has the flexibility of choosing any combination of basis and test functions, as long as they can be expressed in the polynomials form.

It is capable of handling any order of integrations and the definite integrals of the region of integration that is highly singular can be evaluated with very high degree of accuracy. The conventional numerical integration scheme requires very high order of numerical integration to achieve the same required accuracy but becomes computational prohibitive.

By incorporating the generalised analytical approach to evaluate the elements of the MoM matrix, the matrix-fill time can be greatly reduced without the loss of solution accuracy.

5.2 Recommended Future Work

As in any electromagnetic solver, there is always room for improvement. In the author's opinion, the MoM code developed in this thesis is still restricted to printed circuit traces that are rectangular in geometry, i.e., only the right-angled bend traces can be modeled for the simulation. Analytical expressions for definite integrals with trapezoidal and triangular shaped cells should be developed so that practical bends commonly seen in PCB layout could be modeled.

APPENDICES

A. FULL EXPRESSIONS OF VARIOUS INTEGRATIONS

The full expressions of all the integrations required in this thesis are listed here. The definition of C_m^n and R are given by

$$C_m^n = \frac{n!}{m!(n-m)!} \qquad R = \sqrt{u^2 + v^2 + w^2}$$

$$\int R^n du = \begin{cases} u \sum_{p=0}^{(n-1)/2} \left[\frac{\prod_{q=0}^{p-1} (n-2q)}{\prod_{q=0}^{p} (n+1-2q)} \left(v^2 + w^2\right)^p R^{n-2p} \right] \\ + \left[\prod_{q=0}^{(n-1)/2} \frac{(n-2q)}{(n+1-2q)} \right] \left(v^2 + w^2\right)^{(n+1)/2} \tanh^{-1} \frac{u}{R}, \quad n = \text{odd} \\ u \sum_{p=0}^{n/2} \left[\frac{\prod_{q=0}^{p-1} (n-2q)}{\prod_{q=0}^{p} (n+1-2q)} \left(v^2 + w^2\right)^p R^{n-2p} \right], \qquad n = \text{even} \end{cases} \tag{A.1}$$

$$\int u^m R^n du = \begin{cases} \sum_{p=0}^{(m-1)/2} (-1)^p C_{(m-1)/2}^n \left(v^2 + w^2\right)^p \frac{R^{n+m-2p+1}}{n+m-2p+1}, & m = \text{odd} \\ \sum_{p=0}^{m/2} (-1)^p C_{m/2}^n \left(v^2 + w^2\right)^p \int R^{n+m-2p} du, & m = \text{even} \end{cases} \tag{A.2}$$

$$\int \frac{u^n}{\left(u^2+w^2\right)R}du = \begin{cases} \sum_{p=0}^{(n-3)/2} (-1)^p w^{2p} \int \frac{u^{n-2-2p}}{R}du \\ +(-1)^{(n-3)/2} v^{-1} w^{n-1} \tanh^{-1}\frac{v}{R}, \quad n = \text{odd} \\ \sum_{p=0}^{n/2-1} (-1)^p w^{2p} \int \frac{u^{n-2-2p}}{R}du \\ +(-1)^{n/2} v^{-1} w^{n-1} \tan^{-1}\frac{uv}{wR}, \quad n = \text{even} \end{cases} \tag{A.3}$$

$$\int u^n \tanh^{-1}\frac{u}{R}du = \frac{u^{n+1}}{n+1}\tanh^{-1}\frac{u}{R} - \frac{1}{(n+1)}\int \frac{u^{n+1}}{R}du \tag{A.4}$$

$$\int u^n \tanh^{-1}\frac{v}{R}du = \frac{u^{n+1}}{n+1}\tanh^{-1}\frac{v}{R} + \frac{v}{(n+1)}\int \frac{u^{n+2}}{\left(u^2+w^2\right)R}du \tag{A.5}$$

$$\int u^n \tan^{-1}\frac{vw}{uR}du = \frac{u^{n+1}}{n+1}\tan^{-1}\frac{vw}{uR} + \frac{vw}{(n+1)}\int \frac{u^{n+1}}{\left(u^2+v^2\right)R}du + \frac{vw}{(n+1)}\int \frac{u^{n+1}}{\left(u^2+w^2\right)R}du \tag{A.6}$$

$$\int u^n \tan^{-1}\frac{uw}{vR}du = \frac{u^{n+1}}{n+1}\tan^{-1}\frac{uw}{vR} - \frac{vw}{(n+1)}\int \frac{u^{n+1}}{\left(u^2+v^2\right)R}du \tag{A.7}$$

$$\int\int R^n dudv = \begin{cases} u\sum_{p=0}^{(n-1)/2}\left[\frac{\prod_{q=0}^{p-1}(n-2q)}{\prod_{q=0}^{p}(n+1-2q)}\sum_{s=0}^{p} C_s^p w^s \int v^{p-s} R^{n-2p}dv\right] \\ +\left[\prod_{q=0}^{(n-1)/2}\frac{(n-2q)}{(n+1-2q)}\right]\sum_{s=0}^{(n+1)/2} C_s^{(n+1)/2} w^s \\ \times \int v^{(n+1)/2-s}\tanh^{-1}\frac{u}{R}dv, \quad n = \text{odd} \\ u\sum_{p=0}^{n/2}\left[\frac{\prod_{q=0}^{p-1}(n-2q)}{\prod_{q=0}^{p}(n+1-2q)}\sum_{s=0}^{p} C_s^p w^s \int v^{p-s} R^{n-2p}dv\right], \quad n = \text{even} \end{cases} \tag{A.8}$$

$$\int\int u^m R^n \, dudv = \begin{cases} \sum_{p=0}^{(m-1)/2} (-1)^p C_{(m-1)/2}^n \sum_{s=0}^{p} \dfrac{C_s^p w^s}{n+m-2p+1} \\ \times \int v^{p-s} R^{n+m-2p+1} dv, & m = \text{odd} \\ \sum_{p=0}^{m/2} (-1)^p C_{m/2}^n \sum_{s=0}^{p} C_s^p w^s \\ \times \int v^{p-s} \int R^{n+m-2p} \, dudv, & m = \text{even} \end{cases} \tag{A.9}$$

$$\int\int\int R^n \, dudvdw = \begin{cases} u \sum_{p=0}^{(n-1)/2} \left[\dfrac{\prod_{q=0}^{p-1} (n-2q)}{\prod_{q=0}^{p} (n+1-2q)} \sum_{s=0}^{p} C_s^p \int w^s \int v^{p-s} R^{n-2p} \, dvdw \right] \\ + \left[\prod_{q=0}^{(n-1)/2} \dfrac{(n-2q)}{(n+1-2q)} \right] \sum_{s=0}^{(n+1)/2} C_s^{(n+1)/2} \\ \times \int w^s \int v^{(n+1)/2-s} \tanh^{-1} \dfrac{u}{R} \, dvdw, \\ n = \text{odd} \\ u \sum_{p=0}^{n/2} \left[\dfrac{\prod_{q=0}^{p-1} (n-2q)}{\prod_{q=0}^{p} (n+1-2q)} \sum_{s=0}^{p} C_s^p \int w^s \int v^{p-s} R^{n-2p} \, dvdw \right], \\ n = \text{even} \end{cases} \tag{A.10}$$

$$\int\int\int u^m R^n \, dudvdw = \begin{cases} \sum_{p=0}^{(m-1)/2} (-1)^p C_{(m-1)/2}^n \sum_{s=0}^{p} \dfrac{C_s^p}{n+m-2p+1} \\ \times \int w^s \int v^{p-s} R^{n+m-2p+1} \, dvdw, & m = \text{odd} \\ \sum_{p=0}^{m/2} (-1)^p C_{m/2}^n \sum_{s=0}^{p} C_s^p \\ \times \int w^s \int v^{p-s} \int R^{n+m-2p} \, dudvdw, & m = \text{even} \end{cases} \tag{A.11}$$

B. N-POINT QUADRATURE INTEGRATION SCHEME

The *N*-point quadrature single integration is defined as

$$QI_N^{(1)} = \sum_{i=1}^{N} w_i f(x_i) \tag{B.1}$$

Since the weights are symmetrical, the *N*-point quadrature single integration can be written as follow

$$QI_N^{(1)} = \sum_{i=1}^{N/2} w_i \left[f(x_i) + f(x_{N-i+1}) \right] \tag{B.2}$$

The *N*-point quadrature double, triple and quadruple integrations can also be written as follows

$$\begin{aligned} QI_N = \sum_{i=1}^{N/2} \sum_{j=1}^{N/2} w_i w_j \Big[& f(x_i, x_j) + f(x_{N-i+1}, x_j) \\ & + f(x_i, x_{N-j+1}) + f(x_{N-i+1}, x_{N-j+1}) \Big] \end{aligned} \tag{B.3}$$

$$\begin{aligned} QI_N = \sum_{i=1}^{N/2} \sum_{j=1}^{N/2} \sum_{k=1}^{N/2} w_i w_j w_k \Big[& f(x_i, x_j, x_k) + f(x_{N-i+1}, x_j, x_k) \\ & + f(x_i, x_{N-j+1}, x_k) + f(x_{N-i+1}, x_{N-j+1}, x_k) \\ & + f(x_i, x_j, x_{N-k+1}) + f(x_{N-i+1}, x_j, x_{N-k+1}) \\ & + f(x_i, x_{N-j+1}, x_{N-k+1}) + f(x_{N-i+1}, x_{N-j+1}, x_{N-k+1}) \Big] \end{aligned} \tag{B.4}$$

$$
\begin{aligned}
QI_N = \sum_{i=1}^{N/2}\sum_{j=1}^{N/2}\sum_{k=1}^{N/2}\sum_{l=1}^{N/2} w_i w_j w_k w_l \Big[& f\left(x_i, x_j, x_k, x_l\right) + f\left(x_{N-i+1}, x_j, x_k, x_l\right) \\
& + f\left(x_i, x_{N-j+1}, x_k, x_l\right) + f\left(x_{N-i+1}, x_{N-j+1}, x_k, x_l\right) \\
& + f\left(x_i, x_j, x_{N-k+1}, x_l\right) + f\left(x_{N-i+1}, x_j, x_{N-k+1}, x_l\right) \\
& + f\left(x_i, x_{N-j+1}, x_{N-k+1}, x_l\right) + f\left(x_{N-i+1}, x_{N-j+1}, x_{N-k+1}, x_l\right) \\
& + f\left(x_i, x_j, x_k, x_{N-l+1}\right) + f\left(x_{N-i+1}, x_j, x_k, x_{N-l+1}\right) \\
& + f\left(x_i, x_{N-j+1}, x_k, x_{N-l+1}\right) + f\left(x_{N-i+1}, x_{N-j+1}, x_k, x_{N-l+1}\right) \\
& + f\left(x_i, x_j, x_{N-k+1}, x_{N-l+1}\right) + f\left(x_{N-i+1}, x_j, x_{N-k+1}, x_{N-l+1}\right) \\
& f\left(x_i, x_{N-j+1}, x_{N-k+1}, x_{N-l+1}\right) + f\left(x_{N-i+1}, x_{N-j+1}, x_{N-k+1}, x_{N-l+1}\right) \Big]
\end{aligned}
\tag{B.5}
$$

where w_i, w_j, w_k and w_l are the weights, x_i, x_j, x_k and x_l are the abscissas and $f()$ is the function to be integrated.

AUTHOR'S PUBLICATIONS

International Journal Papers

1. K. Y. See and **Z. H. Liu**, "Efficient evaluation of non-redundant Moment-Method matrix for electrically large object," *Microwave and Optical Technology Letters*, Vol. 43, No. 3, pp. 266–268, Nov. 2004.
2. E. K. Chua, K. Y. See and **Z. H. Liu**, "Accurate and efficient computation of MoM matrix involving 2D triangular basis function with line matching," *Int. Journal of Computational Methods*. Vol. 3, No. 3, pp. 355–370, Sep. 2006.
3. **Z. H. Liu,** E. K. Chua and K. Y. See, "Accurate and efficient evaluation of MOM matrix based on a generalized analytical approach," *Progress in Electromagnetics Research*, Vol. 94, pp. 367–382, 2009.

Conference Papers

1. **Z. H. Liu**, K. Y. See, and E. P. Li, "An Improved Integral Equation Approach for Finite-Size Printed Circuit EMI Analysis", *International Symposium on Integrated Circuits, Devices and Systems, ISIC-2004: Integrated Systems on Silicon-Proceedings,* pp. 353-356, Sep. 2004.
2. **Z. H. Liu**, K. Y. See, and E. P. Li, "Study on the power bus noise isolation using a SPICE compatible method," *International Symposium on Electromagnetic Compatibility*, Vol. 2, pp. 438-441, Aug. 2005.

3. **Z. H. Liu**, K. Y. See, E. P. Li and E. K. Chua, "Crosstalk analysis in frequency and time domain using FDTD-VF method," *IEEE Electronics Packaging Technology Conference*, pp. 167-170, Dec. 2005.
4. **Z. H. Liu**, K. Y. See, E. P. Li and E. K. Chua, "An efficient approach for the power/ground plane equivalent circuit extraction," *Proc. Int. Zurich Sym. Electromagnetic Compatibility*, pp. 379-382, Mar. 2006.
5. K. Y. See, **Z. H. Liu** and E. P. Li, "MoM modeling of high-speed power bus radiation," *Proc. Electronic Packaging Technology Conference*, pp. 649-651, Dec. 2004.
6. K. Y. See, O. Manish, **Z. H. Liu** and K. L. Kyaw, "Correlation between ground bounce and radiated emission," *Proceedings of 6th Electronics Packaging Technology Conference*, pp. 640-642, 2004.
7. E. K. Chua, K. Y. See and **Z. H. Liu**, "Modeling RF voltage drop of printed circuit interconnects using a full-wave approach," *17th International Zurich Symposium on Electromagnetic Compatibility*, pp. 332-335, Mar. 2006.
8. K. Y. See, E. K. Chua and **Z. H. Liu**, "Prediction of RF ground voltage drop using a full-wave approach," *International Symposium on Electromagnetic Compatibility*, Vol. 3, pp. 712-717, Aug. 2006.
9. K. Y. See, E. K. Chua and **Z. H. Liu**, "Full wave modeling of RF voltage drop on printed circuit interconnects," *Proc. Electronics System-integration Technology Conference (ESTC)*, pp. 491-497, Sep. 2006.

BIBLIOGRAPHY

[1] C. R. Paul, *Introduction to electromagnetic compatibility*, John Wiley & Sons, 1992.

[2] J. J. Goedbloed, *Electromagnetic compatibility*, Prentice Hall, 1992.

[3] M. I. Montrose and E. M. Nakauchi, *Testing for EMC compliance: approaches and techniques*, Wiley-IEEE Press, 2004.

[4] B. Archambeault, C. Brench, and O. M. Ramahi, *EMI/EMC Computational Modeling Handbook*, 2nd ed., Kluwer Academic Publishers, 2001.

[5] H. Singh and R. Garg, "EMC standardization", *Proceedings of the International Conference on Electromagnetic Interference and Compatibility*, pp. 296-299, Dec. 1999.

[6] *Electromagnetic compatibility (EMC). Part 6-3, Generic standards - Emission standard for residential, commercial and light-industrial environments*, 2nd ed., IEC, 2006.

[7] C. Marshman, *The guide to the EMC directive 89/336/EEC*, 2nd ed., EPA Press, 1995.

[8] S. C. Thierauf, *High-speed circuit board signal integrity*, Artech House, 2004.

[9] C. K. Cheng, J. Lillis, S. Lin, and N. H. Chang, *Interconnect analysis and synthesis*. John Wiley & Sons, 2000.

[10] Z. H. Liu, K. Y. See, E. P. Li, and E. K. Chua, "Crosstalk analysis in frequency and time domain using FDTD-VF method," *IEEE Electronics Packaging Technology Conference*, pp. 167-170, Dec. 2005.

[11] K. Armstrong, *EMC for printed circuit boards: basic and advanced design layout techniques*, Nutwood UK Ltd, 2007.

[12] H. W. Ott, *Noise reduction techniques in electronic systems*, John Wiley & Sons, 2nd ed., 1988.

[13] M. K. Amirhosseini and A. Cheldavi, "Efficient Interconnect Design Using Grounded-Lines", *J. Electromagn. Waves and Appl.*, Vol. 17, No. 9, pp. 1289-1300, Sep. 2003.

[14] D. L. Terrell and R. K. Keenan, *Digital design for interference specifications: a practical handbook for EMI suppression*, 2nd ed., Newnes, 2000.

[15] Y. H. Lin and T. L. Wu, "Analysis of radiation caused by SSN and transmission line by combining the equivalent circuits of active IC into FDTD," *IEEE Int. Symp. Electromagnetic Compatibility*, Vol. 1, pp. 277-282, Aug. 2004.

[16] S. W. Leung, L. Wan, and C. M. Ip, "Modeling of the ground bounce effect on PCBs for high speed digital circuits," *IEEE Int. Symp. Electromagnetic Compatibility*, Vol. 1, pp. 110-115, Aug. 1999.

[17] F. Y. Yuan, "Analysis of power/ground noises and decoupling capacitors in printed circuit board systems," *IEEE Int. Symp. Electromagnetic Compatibility*, pp. 425-430, Aug. 1997.

[18] T. Granberg, *Handbook of digital techniques for high-speed design; design examples, signaling and memory technologies, fiber optics, modeling and simulation to ensure signal integrity*, Prentice Hall, 2004.

[19] W. C. Bosshart, *Printed circuit boards design and technology*, Tata, McGraw-Hill, 1983.

[20] B. Archambeault, *PCB design for real-world EMI control*, Kluwer Academic Publishers, 2002.

[21] H. W. Johnson and M. Graham, *High speed digital design: a handbook of black magic*, Prentice Hall, 1993.

[22] M. I. Montrose, *EMC and the printed circuit board: design, theory, and layout made simple*, IEEE Press, 1998.

[23] S. Yoshida and H. Tohya, "Novel decoupling circuit enabling notable electromagnetic noise suppression and high-density packaging in a digital printed circuit board," *IEEE Int. Symp. Electromagnetic Compatibility,* Vol. 2, pp. 641-646, Aug. 1998.

[24] C. R. Paul, "A comparison of the contributions of common-mode and differential-mode currents in radiated emissions," *IEEE Trans. Electromagnetic Compatibility*, Vol. 31, No. 2, pp. 189-193, May 1989.

[25] C. R. Paul and K. B. Hardin, "Diagnosis and reduction of conducted noise emissions," *IEEE Trans. Electromagnetic Compatibility*, Vol. 30, No. 4, pp. 553-560, Nov. 1988.

[26] T. Watanabe, O. Wada, Y. Toyota, and R. Koga, "Estimation of common-mode EMI caused by a signal line in the vicinity of ground edge on a PCB," *IEEE Int. Symp. Electromagnetic Compatibility*, pp. 113-118, Aug. 2002.

[27] F. Han, "Radiated emission from shielded cables by pigtail effect," *IEEE Trans. Electromagnetic Compatibility*, Vol. 34, No. 3, pp. 345-348, Aug. 1992.

[28] D. M. Hockanson, J. L. Drewniak, T. H. Hubing, T. P. VanDoren, S. Fei, and M. J. Wilhelm, "Investigation of fundamental EMI source mechanisms driving common-mode radiation from printed circuit boards with attached cables," *IEEE Trans. Electromagnetic Compatibility,* Vol. 38, No. 4, pp. 557-566, Nov 1996.

[29] X. Ye, J. Nadolny, J. L. Drewniak, T. H. Hubing, T. P. VanDoren, and D. E. DuBroff, "EMI associated with inter-board connection for module-on-backplane and stacked-card configurations," *IEEE Int. Symp. Electromagnetic Compatibility*, Vol. 2, pp. 797-802, 1999.

[30] T. Sudo, "Predicting commo mode radiation of power bus structure excited by IC's switching current," *19th International Zurich Symposium on Electromagnetic Compatibility*, pp. 160-163, May 2008.

[31] A. C. Polycarpou, *Introduction to the finite element method in electromagnetics*, Morgan & Claypool, 2006.

[32] J. M. Jin, *The finite element method in electromagnetics*, John Wiley & Sons, 1993.

[33] D. W. Pepper and J. C. Heinrich, *The finite element method: basic concepts and applications*, Taylor & Francis, 2nd ed., 2006.

[34] D. M. Sullivan, *Electromagnetic simulation using the FDTD method*, IEEE Press, 2000.

[35] N. V. Kantartzis and T. D. Tsiboukis, *Modern EMC analysis techniques*, Morgan & Claypool Publishers, 2008.

[36] A. Taflove and S. C. Hagness, *Computational electrodynamics: the finite-difference time-domain method*, Artech House, 3rd ed., 2005.

[37] P. B. Johns and R. L. Beurle, "Numerical solution of 2-dimensional scattering problems using a transmission-line matrix" *IEE Proc.*, Vol. 118, No. 9, 1203–1208, 1971.

[38] C. Christopoulos and J. L. Herring, "The application of transmission-line modeling (TLM) to electromagnetic compatibility problems," *IEEE Trans. Electromagnetic Compatibility*, Vol. 35, No. 2, pp. 185-191, May 1993.

[39] R. Holland, R. St. John, *Statistical electromagnetics*, Taylor & Francis, 1999.

[40] R. Holland, V. P. Cable, and L. C. Wilson, "Finite-volume time-domain (FVTD) techniques for EM scattering," *IEEE Trans. Electromagnetic Compatibility*, Vol. 33, No. 4, pp. 281-294, Nov. 1991.

[41] F. M. Tesche, M. V. Ianoz, and T. Karlsson, *EMC analysis methods and computational models*, John Wiley & Sons, 1997.

[42] W. C. Gibson, *The method of moments in electromagnetics*, Chapman & Hall/CRC, 2008.

[43] J. Moore and R. Pizer, *Moment methods in electromagnetics: techniques and applications*. John Wiley & Sons, 1984.

[44] R. F. Harrington, *Field Computation by Moment Methods*, 2nd ed., IEEE Press, 1993.

[45] E. K. Miller, *Computational Electromagnetics: Frequency-Domain Method of Moments*, IEEE Press, 1992.

[46] A. R. Hall, *Generalized method of moments*. Oxford University Press, 2005.

[47] A. F. Peterson, S. L. Ray, and R. Mittra, *Computational Methods for Electromagnetics*, IEEE Press, 1998.

[48] M. G. Araujo, J. M. Bertolo, F. Obelleiro, J. L. Rodriguez, J. M., Taboada, and L. Landesa, "Geometry based preconditioner for radiation problems involving wire and surface basis functions," *Progress in Electromagnetics Research*, Vol. 93, 29–40, 2009.

[49] J. Yeo and R. Mittra, "An algorithm for interpolating the frequency variations of method-of-moments matrices arising in the analysis of planar microstrip structures," *IEEE Trans. Microw. Theory & Techn.*, Vol. 51, No. 3, 1018–1025, Mar. 2003.

[50] K. L. Virga, and R.-S. Yahya, "Efficient wide-band evaluation of mobile communications antennas using [Z] or [Y] matrix interpolation with the method of moments," *IEEE Trans. Antennas Propag.*, Vol. 47, No. 1, pp. 65-76, Jan. 1999.

[51] B. J. Fasenfest, F. Capolino, D. R. Wilton, D. R. Jackson, and N. J. Champagne, "A fast MoM solution for large arrays: Green's function interpolation with FFT," *IEEE Antennas and Wireless Propag. Letter*, Vol. 3, 161–164, 2004.

[52] E. A. Soliman, "Rapid frequency sweep technique for MoM planar solvers," *IEE Proc. Microw. Antennas Propag.*, Vol. 151, No. 4, 277–282, Aug. 2004.

[53] E. A. Soliman, A. K. Abdelmageed, and M. A. El-Gamal, "Neural computation of the MoM matrix elements for planar configurations," *Int. J. of Electronics and Communications*, Vol. 56, No. 3, 155–162, 2002.

[54] Y. Xiong, D. G. Fang, and Q. J. Zhang, "Application of two-dimensional AWE algorithm in training neural networks," *3rd Int. Conf. On Microw. and Millimeter wave Tech. Proc.*, 879–882, 2002.

[55] E. A. Soliman, H. B. Mohamed, and K. N. Natalia, "Neural networks-method of moments (NN-MoM) for the efficient filling of the coupling matrix," *IEEE Trans. Antennas Propag.*, Vol. 52, No. 6, 1521–1529, Jun. 2004.

[56] L. Tarricone, M. Mongiardo, and F. Cervelli, "A quasi one-dimensional integration technique for the analysis of planar microstrip circuits via MPIE/MoM," *IEEE Trans. Microw. Theory & Techn.*, Vol. 49, No. 3, 517–523, Mar. 2001.

[57] J. R. Smith and M. S. Mirotznik, "Analytical simplification of the 2-D method of moments impedance integral," *IEEE Trans. Antennas Propag.*, Vol. 52, No. 12, 3288–3294, Dec. 2004.

[58] J. R. Smith and M. S. Mirotznik, "Moments via integral transform method for 2-D dielectric materials," *IEEE Trans. Antennas Propag.*, Vol. 53, No. 1, 560–563, Jan. 2005.

[59] K. Mahadevan and H. A. Auda, "Electromagnetic field of a rectangular patch of uniform and linear distributions of current," *IEEE Trans. Antennas Propag.*, Vol. 37, No. 12, 1503–1509, Dec. 1989.

[60] L. Alatan, M. I. Aksun, K. Mahadevan, and M. T. Birand, "Analytical evaluation of the MoM matrix elements," *IEEE Trans. Microw. Theory & Techn.*, Vol. 44, No. 4, 519–525, Apr. 1996.

[61] E. K. Chua, K. Y. See, and Z. H. Liu, "Accurate and efficient computation of MoM matrix involving 2D triangular basis function with line matching," *Int. J. of Computational Methods*, Vol. 3, No. 3, 355–370, Sep. 2006.

[62] X. C. Wei, E. P. Li, and Y. J. Zhang, "Application of the improved finite element-fast multipole method on large scattering problems," *Progress in Electromagnetics Research*, Vol. 47, 49–60, 2004.

[63] P. Zhao and H. G. Wang, "Resistances and inductances extraction using surface integral equation with the acceleration of multilevel Green function interpolation method," *Progress in Electromagnetics Research*, Vol. 83, 43–54, 2008.

[64] X. C. Wei, E. P. Li, and C. H. Liang, "Fast solution for large scale electromagnetic scattering problems using wavelet transform and its precondition," *J. Electromagn. Waves and Appl.*, Vol. 17, No.4, 611–613, 2003.

[65] K. F. A. Hussein, "Fast computational algorithm for EFIE applied to arbitrarily-shaped conducting surfaces," *Progress in Electromagnetics Research*, Vol. 68, 339–357, 2007.

[66] M. Martinez-Burdalo, L. Nonidez, A. Martin, and R. Villar, "Using a combination of FDTD with a surface integration method for electromagnetic scattering analysis in large regions," *Microwave and Optical Technology Letters*, Vol. 22, No. 1, pp. 74–78, Jul. 1999.

[67] R. J. Luebbers, K.S. Kunz, M. Schneider, and F. Hunsberger, " A finite-difference time-domain near zone to far zone transformation," *IEEE Trans. Antennas Propag.*, Vol. 39, No. 4, pp. 429–433, Apr. 1991.

[68] D. A. Weston, *Electromagnetic compatibility: principles and applications*, Marcel Dekker, 2nd ed., 2001.

[69] J. K. Mao, J. L. Drewniak, G. Antonini, and A. Orlandi, "Extraction of SPICE-type equivalent circuits of signal via transitions using the PEEC method," *IEEE Int. Symp. Electromagnetic Compatibility*, Vol. 3, pp. 980-983, Aug. 2004.

[70] S. V. Kochetov and G. Wollenberg, "Stable time domain PEEC solution for pulse interconnection structures," *IEEE Int. Symp. Electromagnetic Compatibility*, Vol. 3, pp. 911-916, Aug. 2005.

[71] J. E. Garrett, A. E. Ruehli, and C. R. Paul, "Accuracy and stability improvements of integral equation models using the partial element equivalent circuit," *IEEE Trans. Antennas Propag.*, Vol. 46, No. 12, pp.1824–1832, Dec. 1998.

[72] G. Dural and M. I. Aksun, "Closed-form Green's functions for general sources and stratified media," *IEEE Trans. Microw. Theory & Techn.*, Vol. 43, No. 7, pp. 1545-1552, Jul. 1995.

[73] M. J. Tsai, F. De Flaviis, O. Fordham, and N. G. Alexopoulos, "Modeling planar arbitrarily shaped microstrip elements in multilayered media," *IEEE Trans. Microw. Theory & Techn.*, Vol. 45, No. 3, pp. 330-337, Mar. 1997.

[74] M. Kahrizi, T. K. Sarkar, and Z. A. Maricevic, "Analysis of a wide radiating slot in the ground plane of a microstrip line," *IEEE Trans. Microw. Theory & Techn.*, Vol. 41, No. 1, pp. 29–37, Jan. 1993.

[75] M. I. Aksun and G. Dural, "Clarification of issues on the closed-form Green's functions in stratified media," *IEEE Trans. Antennas Propag.*, Vol. 53, No. 11, pp. 3644-3653, Nov. 2005.

[76] N. Kinayman and M. I. Aksun, "Efficient evaluation of spatial-domain MoM matrix entries in the analysis of planar stratified geometries," *IEEE Trans. Microw. Theory & Techn.*, Vol. 48, No. 2, pp. 309–312, Feb. 2000.

[77] K. Y. See and E. M. Freeman, "Rigorous approach to modeling electromagnetic radiation from finite-size printed circuit structures," *IEE Proc. Microw., Antenna & Propag.*, Vol. 146, No. 1, pp. 29–34, Feb. 1999.

[78] A. W. Glisson and D. R. Wilton, "Simple and efficient numerical methods for problems of electromagnetic radiation and scattering from surfaces," *IEEE Trans. Antennas Propag.*, Vol. 28, No. 5, pp. 593-603, Sep. 1980.

[79] R. F. Harrington, *Time-harmonic electromagnetic field*. McGraw-Hill, 1961.

[80] Z. Haznadar and Z. Stih, *Electromagnetic fields, waves and numerical methods*, ISO Press, 2000.

[81] R. E. Collin, *Field theory of guided waves*, New York, IEEE Press, 2nd ed., 1991.

[82] A. F. Peterson, S. L. Ray, and R. Mittra, *Computational Methods for Electromagnetics*, Oxford University Press and IEEE Press, 1998.

[83] C. T. Tai, *Dyadic green functions in electromagnetic theory*, IEEE Press, 2nd ed., 1993.

[84] T. K. Sarkar, S. M. Rao, and A. R. Djordjevic, "Electromagnetic scattering and Radiation from finite microstrip structures", *IEEE Trans. Microw. Theory & Techn.*, Vol. 38, pp.1568-1575, Nov. 1990.

[85] T. K. Sarkar, and E. Arvas, "Scattering cross section of composite conducting and lossy dielectric bodies", *Proc. of the IEEE*, Vol. 77, No. 5, pp.788-795, May 1989.

[86] T. K. Sarkar, and E. Arvas, "An integral equation approach to the analysis of finite microstrip antennas: volume/surface formulation", *IEEE Trans. Antennas Propag.*, Vol. 38, No. 3, pp.305-312, March 1990.

[87] J. R. Mosig, "Arbitrarily shaped microstrip structures and their analysis with a mixed potential integral equation," *IEEE Trans. Microw. Theory & Techn.*, Vol. 36, No. 2, pp. 314–323, Feb. 1988.

[88] L. V. Kantorovich and V. I. Krylov, *Approximate methods of higher analysis*, 4th ed., New York, 1959.

[89] R. Bancroft, *Understanding electromagnetic scattering using the moment method a practical approach*, Artech House.1996.

[90] J. H. Richmond, "Digital computer solutions of the rigorous equations for scattering problems," *Proc. of the IEEE*, Vol. 53, No. 8, pp. 796-804, Aug. 1965.

[91] J. J. H. Wang, *Generalized moment methods in electromagnetics: formulation and computer solution of integral equations*, New York. J. Wiley, 1991.

[92] R. F. Harrington, "Matrix methods for field problems," *Proc. of the IEEE*, Vol. 55, No. 2, pp.136-149, Feb. 1967.

[93] D. M. Pozar, *Microwave engineering*, Addison Wesley, 1993.

[94] D. K. Cheng, *Field and wave electromagnetic*, 2nd ed., Addison Wesley, 1989.

[95] A. B. Polyanin and A. V. Manzhirov, *Handbook of Integral Equations*, CRC Press, 1998.

[96] K. Mahadevan and H. A. Auda, "Electromagnetic field of a rectangular patch of uniform and linear distributions of current," *IEEE Trans. Antennas Propag.*, Vol. 37, No. 12, pp. 1503-1509, Dec. 1989.

[97] L. Alatan, M. I. Aksun, K. Mahadevan and M. T. Birand, "Analytical evaluation of the MoM matrix elements," *IEEE Trans. Microw. Theory & Techn.*, Vol. 44, No. 4, pp. 519-525, Apr. 1996.

[98] J. Waldvogel, "The Newtonian Potential of a Homogenous Cube", *Journal of Appl. Math. Phys. (ZAMP)*, Vol. 27, pp. 867-871, 1976.

[99] http://www.maplesoft.com/

[100] http://mathworld.wolfram.com/

[101] Y. Saad and M. H. Schultz, "GMRES: A generalized minimal residual algorithm for solving nonsymmetric linear systems," *SIAM J. Sci. Stat. Comput.*, Vol. 7, No. 3, pp. 856-869, Jul. 1986.

[102] D. A. Hill, K. H. Cavcey and R. T. Johnk, "Crosstalk between microstrip transmission lines," *IEEE Trans. Electromagnetic Compatibility*, Vol. 36, No. 4, pp. 314-321, Nov. 1994.